Ho, S., Hunt, D., Steiner, A., Mannucci, A. J., Kirchengast, G., Gleisner, H., Heise, S., v. Engeln, A., Marquardt, C., Sokolovskiy, S., Schreiner, W., Ao, C., Wickert, J., Syndergaad, S., Lauritsen, K., Leroy, S., Kursinski, R., Kuo, Y.-H., Scherllin-Pirscher, B., Foelsche, U., Schmidt, T., Gorbunov, M. (2012): Reproducibility of GPS radio occultation data for climate monitoring: Profile-to-profile inter-comparison of CHAMP climate records 2002 to 2008 from six data centers. - Journal of Geophysical Research, 117, D18

DOI: 10.1029/2012JD017665

Reproducibility of GPS radio occultation data for climate monitoring: Profile-to-profile inter-comparison of CHAMP climate records 2002 to 2008 from six data centers

Shu-peng Ho,[1] Doug Hunt,[1] Andrea K. Steiner,[2] Anthony J. Mannucci,[3] Gottfried Kirchengast,[2] Hans Gleisner,[4] Stefan Heise,[5] Axel von Engeln,[6] Christian Marquardt,[6] Sergey Sokolovskiy,[1] William Schreiner,[1] Barbara Scherllin-Pirscher,[2] Chi Ao,[3] Jens Wickert,[5] Stig Syndergaard,[4] Kent B. Lauritsen,[4] Stephen Leroy,[7] Emil R. Kursinski,[8] Ying-Hwa Kuo,[1] Ulrich Foelsche,[2] Torsten Schmidt,[5] and Michael Gorbunov[4,9]

Received 20 February 2012; revised 6 August 2012; accepted 10 August 2012; published 25 September 2012.

[1] To examine the claim that Global Positioning System (GPS) radio occultation (RO) data are useful as a benchmark data set for climate monitoring, the structural uncertainties of retrieved profiles that result from different processing methods are quantified. Profile-to-profile comparisons of CHAMP (CHAllenging Minisatellite Payload) data from January 2002 to August 2008 retrieved by six RO processing centers are presented. Differences and standard deviations of the individual centers relative to the inter-center mean are used to quantify the structural uncertainty. Uncertainties accumulate in derived variables due to propagation through the RO retrieval chain. This is reflected in the inter-center differences, which are small for bending angle and refractivity increasing to dry temperature, dry pressure, and dry geopotential height. The mean differences of the time series in the 8 km to 30 km layer range from −0.08% to 0.12% for bending angle, −0.03% to 0.02% for refractivity, −0.27 K to 0.15 K for dry temperature, −0.04% to 0.04% for dry pressure, and −7.6 m to 6.8 m for dry geopotential height. The corresponding standard deviations are within 0.02%, 0.01%, 0.06 K, 0.02%, and 2.0 m, respectively. The mean trend differences from 8 km to 30 km for bending angle, refractivity, dry temperature, dry pressure, and dry geopotential height are within ±0.02%/5 yrs, ±0.02%/5 yrs, ±0.06 K/5 yrs, ±0.02%/5 yrs, and ±2.3 m/5 yrs, respectively. Although the RO-derived variables are not readily traceable to the international system of units, the high precision nature of the raw RO observables is preserved in the inversion chain.

Citation: Ho, S., et al. (2012), Reproducibility of GPS radio occultation data for climate monitoring: Profile-to-profile inter-comparison of CHAMP climate records 2002 to 2008 from six data centers, *J. Geophys. Res.*, *117*, D18111, doi:10.1029/2012JD017665.

1. Introduction

[2] Long-term Climate Data Records (CDRs) constructed from stable and accurate measurements with adequate temporal and spatial coverage are essential for monitoring global and regional climate variability and understanding their forcing mechanisms. Current long-term measurements used to generate CDRs are mainly derived from satellite observations and in situ measurements [see *Intergovernmental Panel on Climate Change* (*IPCC*), 2007]. These satellite sensors were originally designed to provide measurements for short-

[1]COSMIC Program Office, University Corporation for Atmospheric Research, Boulder, Colorado, USA.
[2]Wegener Center for Climate and Global Change and Institute for Geophysics, Astrophysics, and Meteorology, Institute of Physics, University of Graz, Graz, Austria.
Corresponding author: S. Ho, COSMIC Project Office, University Corporation for Atmospheric Research, PO Box 3000, Boulder, CO 80307-3000, USA. (spho@ucar.edu)

0148-0227/12/2012JD017665

[3]Jet Propulsion Laboratory, California Institute of Technology, Pasadena, California, USA.
[4]Danish Meteorological Institute, Copenhagen, Denmark.
[5]Department of Geodesy and Remote Sensing, German Research Centre for Geosciences, Potsdam, Germany.
[6]EUMETSAT, Darmstadt, Germany.
[7]School of Engineering and Applied Sciences, Harvard University, Cambridge, Massachusetts, USA.
[8]Institute of Atmospheric Physics, University of Arizona, Tucson, Arizona, USA.
[9]Institute of Atmospheric Physics, Russian Academy of Sciences, Moscow, Russia.

term weather and environmental predictions, not long-term climate monitoring. As a result, extra effort must be spent on data re-processing, inter-satellite calibration, and multiple satellite data merging procedures in order to account for possible on-board calibration drift and degradation of satellite sensors. Because instrument calibrations lack traceability to the International System of Units (SI), the possible degradation of the sensors and the on-board calibration creates a source of uncertainty that can alias into the climate signal being sought. Even using the same satellite data, climate trends provided by different groups may be very different. For example, to construct consistent temperature CDRs using multiple Microwave Sounding Units (MSU) and Advanced Microwave Sounding Units (AMSU) on the NOAA TIROS Operational Vertical Sounders (TOVS), various calibration and tuning methods from different groups were used to correct the inter-satellite residual biases among the sensors [e.g., *Christy et al.*, 2000; *Mears et al.*, 2003; *Grody et al.*, 2004; *Zou et al.*, 2006; *Zou and Wang*, 2011; *Prabhakara et al.*, 2000]. However, because on-board calibration is unable to fully constrain inter-satellite biases, substantial uncertainties still exist in temperature trends reported from different groups [*IPCC*, 2007; *Thorne et al.*, 2005, 2011]. Many studies have been conducted to investigate the causes of the structural uncertainty among MSU/AMSU data derived from different groups [*Christy et al.*, 2000; *Mears et al.*, 2003, 2011; *Karl et al.*, 2006; *Prabhakara et al.*, 2000; *Zou et al.*, 2006; *Zou and Wang*, 2011].

[3] Radiosonde observations have been used as benchmarks to validate satellite-derived soundings. However, changing instruments and observation practices and limited spatial coverage complicate climate signals from this data set [*Free et al.*, 2005; *Haimberger et al.*, 2008; *Thorne et al.*, 2011].

[4] Global Positioning System (GPS) Radio Occultation (RO) data are currently the only satellite data that maintain SI traceability [*Ohring*, 2007]. By flying a GPS receiver in the low earth orbit (LEO), GPS RO is the first technique to provide measurements that are traceable to the international standard of time, i.e., the SI second [*Hardy et al.*, 1994; *Kursinski et al.*, 1997]. This traceability makes GPS RO a strong candidate for use as a climate benchmark [*Goody et al.*, 1998, 2002].

[5] Accurate RO retrievals of atmospheric variable profiles depend on the adequate calculation of the atmospheric excess phase of two GPS L-band frequencies (1575.42 MHz (L1) and 1227.6 MHz (L2)) due to signal delay and bending in the Earth's atmosphere and ionosphere [*Kursinski et al.*, 1997; *Ho et al.*, 2009a]. Possible error sources of RO-derived products include i) observation errors and ii) inversion errors. Observation errors in RO phase measurements are related to GPS RO signal strength combined with receiver noise for a particular RO mission and local multipath effect [*Kursinski et al.*, 1997]. Theoretical error analyses of RO sounding techniques based on simulations have been conducted [see *Kursinksi et al.*, 1997; *Rieder and Kirchengast*, 2001; *Steiner and Kirchengast*, 2005] and were used to explain causes of errors in retrieved variables. The observation errors consist of random and systematic errors that may be mission-dependent. Error analyses with real RO data were performed to characterize observational errors of individual profiles [*Kuo et al.*, 2004; *Scherllin-Pirscher et al.*, 2011b] and errors of climatological fields [*Scherllin-Pirscher et al.*, 2011a].

[6] Structural uncertainties of RO-retrieved variables for a particular RO mission are mainly due to the inversion errors, which include errors in precise orbit determination (POD), removal of clock fluctuations, and other inversion procedures. While the fundamental phase measurement is synchronized to the ultra-stable atomic clocks on the ground, the RO-derived variables (e.g., refractivity, pressure, temperature) are not. The retrieval results may differ for different processing algorithms and implementations as used in the excess phase processing and inversion procedures, such as noise filtering and profile initializations [*Ho et al.*, 2009a]. RO inversion algorithms are used to convert the RO atmospheric excess phase into atmospheric variables, including bending angle, refractivity, pressure, geopotential height, and temperature in the upper troposphere and lower stratosphere, by assuming a dry atmosphere (defined in section A5).

[7] Currently, multiyear GPS RO data can be obtained from the following centers: the Radio Occultation Meteorology (ROM) Satellite Application Facility (SAF) (formerly GRAS (Global Navigation Satellite System Receiver for Atmospheric Sounding) SAF) at the Danish Meteorological Institute (DMI) in Copenhagen, Denmark; the European Organisation for the Exploitation of Meteorological Satellites (EUMETSAT, hereafter EUM), in Darmstadt, Germany; the German Research Centre for Geosciences (GFZ) in Potsdam, Germany; the Jet Propulsion Laboratory (JPL) in Pasadena, CA, USA; the University Corporation for Atmospheric Research (UCAR) in Boulder, CO, USA; and the Wegener Center/University of Graz (WEGC) in Graz, Austria. These centers use different assumptions, initializations, and implementations in the excess phase processing and inversion procedures (see Appendix A).

[8] To use RO data as a benchmark data set for climate monitoring, it is critically necessary to quantify the reproducibility of RO retrieved profiles. The reproducibility of RO data is defined by the consistency (small structural uncertainty) of i) global averages, ii) monthly zonal averages, and iii) anomaly time series of the RO retrieval profiles among centers due to different assumptions and inversion methods. A first study to this end was performed by *Ho et al.* [2009a] who used five years (2002 to 2006) of refractivity climatologies from CHAMP (CHAllenging Minisatellite Payload) generated by GFZ, JPL, UCAR, and WEGC. Each center used the profiles that passed their own quality control criteria to generate monthly mean climatologies. Results showed that the uncertainty of the trend for the fractional refractivity anomalies among the centers is between (−0.03 to 0.01)%/5 yrs. Thus 0.03%/5 yrs was considered an upper bound in the processing scheme-induced uncertainty for global refractivity trend monitoring. In that study, sampling errors were regarded as the dominant error source at high-latitudes because different quality control mechanisms cause a different number of profiles in climatologies. Numerical weather model re-analysis data were used to determine sampling errors, which were subtracted. Remaining differences among centers contained residual sampling errors and inversion-related structural uncertainty.

[9] The objective of this study is to quantify the reproducibility of RO data from six RO processing centers for all (dry) atmospheric variables. To estimate the reproducibility of RO data, in this study we quantify i) the structural uncertainties, and ii) long-term consistency of retrieved profiles that result

Table 1. Overview on Implementations of Processing Chains at DMI, EUM, GFZ, JPL, UCAR, and WEGC

URL/Processing Step	Implementations for Each Center
URL	DMI: http://www.romsaf.org EUM: http://www.eumetsat.int GFZ: http://isdc.gfz-potsdam.de JPL: http://genesis.jpl.nasa.gov UCAR: http://www.cosmic.ucar.edu WEGC: http://www.wegcenter.at/globclim
POD phase and orbit data	DMI: UCAR CDAAC orbit and phase data used (version 2009.2650). EUM: UCAR CDAAC orbit and phase data used (version 2009.2650). GFZ: POD: EPOS-OC for Rapid Science Orbit provision [*König et al.*, 2006]; Excess Phase: Single differencing, reference link smoothing. JPL: POD: reduced-dynamic strategy using GIPSY software [*Bertiger et al.*, 1994]; Excess Phase: Double differencing. UCAR: POD computed with Bernese 5.0 software [*Dach et al.*, 2007]; Excess Phase: Single differencing, reference link smoothing. WEGC: UCAR CDAAC orbit and phase data used (version 2009.2650).
Bending angle calculation	DMI: Canonical Transform of Type 2 (CT2) inversion [*Gorbunov and Lauritsen*, 2004] below 25 km, combined with GO used above 25 km. EUM: Geometric optics used for BAs at all heights GFZ: Full Spectrum Inversion (FSI) below 15 km [*Jensen et al.*, 2003]; Geometric optics used above 15 km. JPL: Canonical transform (CT) after *Gorbunov* [2002] applied to L1. UCAR: FSI [*Jensen et al.*, 2003] applied to L1 in troposphere < dynamic L2 QC height; Geometric optics used > dynamic L2 QC height. WEGC: Geometric optics used for L1 and L2 BAs at all heights.
Ionospheric correction	DMI: Optimal linear combination of L1 and L2 BAs [*Vorob'ev and Krasil'nikova*, 1994; *Gorbunov*, 2002]; Iono. correction term extrapolation < dynamic L2 QC height. Linear combination of L1 and L2 BAs [*Vorob'ev and Krasil'nikova*, 1994]. EUM: Linear combination of L1 and L2 BAs [*Vorob'ev and Krasil'nikova*, 1994]. GFZ: Linear combination of L1 and L2 BAs [*Vorob'ev and Krasil'nikova*, 1994], JPL: Linear comb. of L1 and L2 BAs [*Vorob'ev and Krasil'nikova*, 1994]; Iono. correction term extrapolation below 10 km. UCAR: Linear comb. of L1 and L2 BAs [*Vorob'ev and Krasil'nikova*, 1994]; Iono. correction term extrapolation < dynamic L2 QC height. WEGC: Linear comb. of L1 and L2 BAs [*Vorob'ev and Krasil'nikova*, 1994]; Iono. correction term extrapolation <15 km.
Initialization of bending angles	DMI: Optimization after *Gorbunov* [2002], but using a two-parameter fit of background (MSISE-90) to data above 40 km in combination with a global background search [*Lauritsen et al.*, 2011]. Dynamic estimation of obs. errors [*Gorbunov*, 2002]; background error fixed at 50%. GFZ: Optimization after *Sokolovskiy and Hunt* [1996] with MSISE-90 (>40 km). JPL: Exponential function fit at 40–50 km and extrapolation above. UCAR: Optimization after *Sokolovskiy and Hunt* [1996] with fitting backgr. prof. (NCAR clim. extrap. to 150 km), dynamic estimation of the top fit height, background and obs. errors [*Lohmann*, 2005]. WEGC: Statistical optimization >30 km with ECMWF analyses and MSISE-90 to 120 km [*Healy*, 2001], dynamic estimation of obs. errors and inverse covariance weighting [*Gobiet and Kirchengast*, 2004; *Gobiet et al.*, 2007].
Derivation of refractivity	DMI: Numerical calculation of the Abel integral [*Fjeldbo et al.*, 1971] from each height to 150 km. GFZ: Abel inversion of the optimized bending angle profiles starts at 150 km. JPL: Able inversion of the ionosphere-corrected bending angle from each height up to 120 km. UCAR: The optimized bending angle is subjected to Abel inversion below 150 km by applying the finite- difference representation [*Sokolovskiy et al.*, 2005]. WEGC: Numerical integration over bending angle (Simpson's trapezoidal rule) from each height (impact par.) to 120 km. Impact par. to height conversion with radius of curvature at mean TP location [*Syndergaard*, 1999]; Sinc-windowed Blackman filter on refractivity (<1 km moving average, for resolution-conserving filtering of residual numerical processing noise).
Dry air retrieval	DMI: Refractivity is directly proportional to air density (applying ideal gas equation). Pressure downward integration of the hydrostatic equation from 150 km (boundary conditions determined from the refractivity and its gradient at the top); Dry geopotential height relative to EGM-96; Temperature: Smith-Weintraub formula for dry air [*Smith and Weintraub*, 1953]. GFZ: Pressure retrieval is initialized at 100 km with MSISE-90. Pressure downward integration using hydrostatic equation. ; Dry geopotential height relative to EGM-96; Dry temperature after Smith-Weintraub eq. and eq. of state. JPL: Pressure integration using hydrostatic equation starting at 40 km. Dry geopotential height relative to JGM-3. Dry temperature after Smith-Weintraub eq. and eq. of state, temperature initialization using ECMWF temperature at 40 km. UCAR: Pressure integration using hydrostatic equation, initialized at 150 km by setting pressure and temperature to zero. Dry temperature after Smith-Weintraub eq. and eq. of state. WEGC: Hydrostatic integral initialization at 120 km, pressure = pressure(MSISE-90); no initialization below 120 km (downward integration); Dry geopotential height relative to EGM-96; Smith-Weintraub eq. and eq. of state (ideal gas) to obtain dry temperature; Same filtering on dry temperature as for refractivity filtering.

Table 1. (continued)

URL/Processing Step	Implementations for Each Center
Quality control	DMI: QC of L2 quality from impact parameters (noise); QC of BA using model from iono. corr.; QC of N using ECMWF analyses: reject if $\Delta N > 10\%$ in 10–45 km. GFZ: QC of forward differences of excess phases and QC of bending angles; QC of N using MSISE-90: reject if $\Delta N > 22.5\%$. JPL: QC of Doppler shift <6 km; QC of N, T < 30 km: ECMWF analyses, >10% ΔN and >10 K ΔT rejected. UCAR: QC of raw L1 Doppler (truncation); QC of L2 Doppler (reject if dynamic QC height > 20 km); QC of bending angle (reject if top fit height <40 km); QC of N using climatology (reject if difference > 50%). WEGC: QC of excess phases and bending angles; QC of N, T using ECMWF analyses: reject if $\Delta N > 10\%$ in 5–35 km and/or $\Delta T > 20$ K in 8–25 km.

from different processing methods. Here we conduct profile-to-profile comparisons (PPCs) (i.e., contain no sampling differences) to quantify the structural uncertainties of RO-retrieved variables and to understand how those uncertainties propagate from bending angle profiles to pressure and temperature profiles. This should help identify the causes of process-dependent errors from each center.

[10] We describe the data sources obtained from six centers in section 2. The method of generating CHAMP PPCs is described in section 3. Results on the differences of global and monthly zonal averages as well as anomaly time series and trends are presented in section 4. Possible causes for the structural differences among the six centers are discussed in section 5. Conclusions are drawn in section 6.

2. Data Sources

[11] CHAMP profiles from GFZ used in this study have been reprocessed with the latest version (006) of GFZ's operational occultation analysis system. It is planned to provide these data via the Information System and Data Center (ISDC, http://isdc.gfz-potsdam.de). Details and related references on the operational standard near-real time orbit and occultation processing can be found in *König et al.* [2006] and *Wickert et al.* [2009].

[12] CHAMP profiles from JPL were downloaded from the JPL Genesis website: http://genesis.jpl.nasa.gov. The inversion procedures used to process CHAMP data for this study are the same as those used in *Ho et al.* [2009a].

[13] UCAR operational CHAMP profiles (version 2009.2650) were downloaded from the UCAR COSMIC (Constellation Observing System for Meteorology, Ionosphere, and Climate) Data Analysis and Archive Center (CDAAC) website: http://cosmic-io.cosmic.ucar.edu/cdaac/index.html. An updated POD code is developed and implemented in this version [*Schreiner et al.*, 2009] (also see section A1.5). A general description of UCAR inversion procedures can be found in *Kuo et al.* [2004], *Ho et al.* [2009a], and *Schreiner et al.* [2011].

[14] RO atmospheric profiles provided by the Wegener Center were retrieved with the WEGC Occultation Processing System (OPS) retrieval software [*Borsche et al.*, 2006; *Kirchengast et al.*, 2007; *Borsche*, 2008; *Foelsche et al.*, 2008a, 2009; *Ho et al.*, 2009a]. A short overview on the current retrieval version OPSv5.4 is given by *Steiner et al.* [2009], a detailed description can be found in *Pirscher* [2010]. The WEGC OPSv5.4 retrieval is based on input data of RO phase and orbit information provided by UCAR CDAAC. WEGC profile and climatology data are available from its global climate monitoring website: http://www.globclim.org. Information on error characteristics is given by *Scherllin-Pirscher et al.* [2011a, 2011b].

[15] EUM and DMI constructed the CHAMP retrievals specifically for this study. Like WEGC, both EUM and DMI started with excess phase and amplitude data, as well as CHAMP orbit data, from UCAR CDAAC. EUM processing generally focuses on level 0 to bending angle processing; hence, they only provided bending angle profiles for this study.

[16] A sequence of processing steps is used by individual centers to inverse time delays to physical parameters. These processing steps include: i) POD and atmospheric excess phase processing, ii) bending angle calculation, iii) ionospheric correction, iv) optimal estimation of the bending angles in the stratosphere, v) calculation of refractivity by Abel inversion, vi) calculation of pressure, temperature, and geopotential height, and vii) quality control (QC). Table 1 summarizes the retrieval methods used in this study for each processing step for the individual centers. Though implementation of these procedures is different, the main processing steps are, to a large extent, common. Detailed implementations of the inversion methods for each processing step used by individual centers are described in Appendix A so as not to detract from the quantitative analysis.

3. Method of Profile-to-Profile Comparison (PPC)

[17] The inter-center statistical comparisons are based on differences of profile-to-profile pairs of bending angle, refractivity, dry temperature, dry pressure, and dry geopotential height profiles. The PPC pairs were first obtained by matching the profiles produced by all six centers. Each center supplied CHAMP processed profiles from January 2002 to August 2008 in a common netCDF file format. The occultation time and occulting GPS satellite identifiers from each profile were then compared with a database of all geometrically possible occultations to obtain standard occultation times. The provided profile files from each center were then given canonical names using the standard occultation times. Only high-quality profiles from individual centers that passed their Quality Controls (QCs) (see section A7) for all retrieved variables are included in the common PPC files. This matching was done within a 5-min time window for occultations using the same GPS satellite. In this way the profile files from all centers were matched and assigned common occultation identifiers. All the centers provided their RO data products on a fixed vertical altitude grid of 200 m from 8 km to 30 km. It should be noted that this does not imply that profiles from all

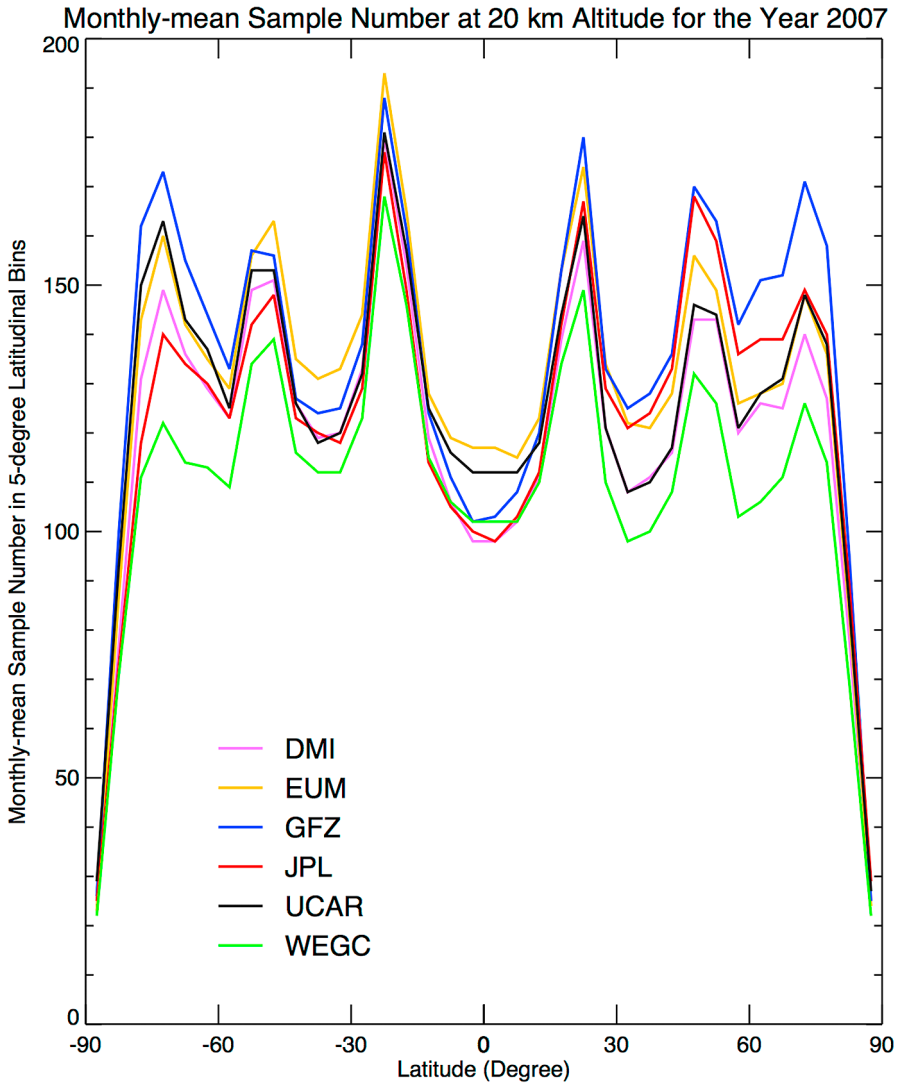

Figure 1. The monthly mean number of samples in latitudinal bins of 5° at 20 km altitude for DMI, EUM, GFZ, JPL, UCAR, and WEGC for the year 2007.

data centers have an intrinsic vertical resolution of 200 m. The data centers applied different smoothing/filtering algorithms on the data so that the intrinsic vertical resolutions would vary from one data set to another and could also be altitude dependent.

[18] Due to the different QC procedures, the total number of profiles varies from center to center. This is demonstrated in the monthly mean sample numbers for each individual center in zonal bins of 5° latitudinal width for 2007 in Figure 1. With the restriction of all QCs from different centers, only 50% of the total available CHAMP profiles are included in the common set.

[19] To quantify the latitudinal and temporal comparisons of inter-center differences, we further compare the monthly mean profile-to-profile climatologies (MPCs) of the common set of CHAMP profiles. For each center we group the matched profiles in zonal bins of 5° latitudinal width (i.e., 36 bins) at the 200 m vertical grid for each month from January 2002 to August 2008. Hereafter we use a common set of CHAMP data whereas *Ho et al.* [2009a] used monthly mean climatologies including a different number of profiles per center. Thus, different from *Ho et al.* [2009a], the sampling error due to temporal and spatial mismatches is not an issue in this study.

4. Quantification of the Structural Uncertainties Among Centers

[20] All comparisons are performed for bending angle (α), refractivity (N), dry temperature (T), dry pressure (p), and dry geopotential height (Z) from January 2002 to August 2008. A global PPC of all matched pairs is conducted in section 4.1 to estimate the mean difference among centers in the investigated period. MPCs are used to investigate the zonal average differences as summarized in section 4.2. Anomaly time series are compared in section 4.3. Trend differences of anomaly time series with respect to the inter-center mean trend are presented in section 4.4. This study seeks to

determine the sources for differences in zonal average fields, anomaly time series, and trends for all RO-derived variables.

4.1. Comparison of Mean Global Differences

4.1.1. Analysis Method

[21] Using the PPC files for all six centers, we generate the global comparison for all variables from January 2002 to August 2008. We first compute the difference for each center to the inter-center mean at each vertical level from 8 km to 30 km. The multiple years of global RO temperature and geopotential height anomalies are computed using the following equation

$$\Delta X^{\mathrm{PPC}}(j) = (1/n) \times \sum\nolimits_{s=1}^{s=n} \left\{ X^{\mathrm{PPC}}(s,j) - X^{\mathrm{PPC}}_{\mathrm{Mean}}(s,j) \right\}. \quad (1)$$

[22] Because bending angle, refractivity, and dry pressure decrease exponentially with height, we present $\Delta\alpha^{\mathrm{PPC}}$, ΔN^{PPC}, and Δp^{PPC} in a fractional sense (i.e., $\Delta X/X$) to better visualize the results. The fractional differences (in %) are computed using the following equation:

$$\Delta X^{\mathrm{PPC}}(j) = 100\% \times (1/n) \times \sum\nolimits_{s=1}^{s=n} \left\{ X^{\mathrm{PPC}}(s,j) - X^{\mathrm{PPC}}_{\mathrm{Mean}}(s,j) \right\} / X^{\mathrm{PPC}}_{\mathrm{Mean}}(s,j). \quad (2)$$

[23] Here j is the index of the vertical levels from 8 km to 30 km and s is the index of all matched pairs. $X^{\mathrm{PPC}}(s, j)$ are the individual profile pairs and $X^{\mathrm{PPC}}_{\mathrm{Mean}}(s, j)$ is the mean profile of all six centers for matched pair s at vertical level j. The refractivity, dry temperature, dry pressure, and dry geopotential height comparisons are for DMI, GFZ, JPL, UCAR, and WEGC and the bending angle comparison is for all six centers including EUM. The total number of matched pairs is n. Here we compute the mean global differences of bending angle ($\Delta\alpha^{\mathrm{PPC}}$ in %), refractivity (ΔN^{PPC} in %), temperature (ΔT^{PPC} in K), pressure (Δp^{PPC} in %), and geopotential height (ΔZ^{PPC} in m) for all matched pairs. The corresponding zonal average differences (section 4.2) and anomaly time series differences (section 4.3) are computed also but the corresponding equations for fractional differences are not specifically listed hereafter.

4.1.2. Bending Angle (α) Difference

[24] Figure 2 depicts the global bending angle differences for DMI, EUM, GFZ, JPL, UCAR, and WEGC (i.e., $\Delta\alpha^{\mathrm{PPC}}_{\mathrm{DMI}}$, $\Delta\alpha^{\mathrm{PPC}}_{\mathrm{EUM}}$, $\Delta\alpha^{\mathrm{PPC}}_{\mathrm{GFZ}}$, $\Delta\alpha^{\mathrm{PPC}}_{\mathrm{JPL}}$, $\Delta\alpha^{\mathrm{PPC}}_{\mathrm{UCAR}}$, $\Delta\alpha^{\mathrm{PPC}}_{\mathrm{WEGC}}$, respectively). The mean differences and the median absolute deviation (MAD) for the 8 km to 30 km layer are listed in Table 2 for each year and for 01/2002 to 08/2008. Structural uncertainty presented here contains the cumulative errors from POD, atmospheric excess phase processing, and intermediate steps for calculation of bending angle among centers (Table 1). In general, the mean $\Delta\alpha$ for all matched pairs among centers agree to within $\pm$0.04% (where the mean $\Delta\alpha^{\mathrm{PPC}}_{\mathrm{JPL}}$ from 2002 to 2008 is equal to 0.04% and that for WEGC is equal to $-$0.03%). The MAD for DMI, EUM, GFZ, JPL, UCAR, and WEGC from the inter-center mean is 0.47%, 0.63%, 0.51%, 0.74%, 0.34%, and 0.32%, respectively. There is an obvious change of the standard deviation for JPL (Std($\alpha^{\mathrm{PPC}}_{\mathrm{JPL}}$)) at 20 km altitude (Figure 2d) where Std($\alpha^{\mathrm{PPC}}_{\mathrm{JPL}}$) ranges from 1% to 0.5% below 20 km. As a result, all the other centers also have a spike near the same height to offset $\Delta\alpha^{\mathrm{PPC}}_{\mathrm{JPL}}$. The reason for the sudden change of Std($\alpha^{\mathrm{PPC}}_{\mathrm{JPL}}$) at 20 km altitude is due to the change in vertical smoothing interval for the L1 bending angles from 200 m below 20 km impact altitude to 1 km above 20 km impact altitude. $\Delta\alpha^{\mathrm{PPC}}_{\mathrm{GFZ}}$ has an obvious positive mean bias below 13 km which is mainly offset by $\Delta\alpha^{\mathrm{PPC}}_{\mathrm{WEGC}}$ in the same height and shows a seasonal dependence, especially in sub-tropical region (see Figure 9a). These biases below 13 km are probably due to differences in geometric optics and wave optics retrievals as well as different approaches for downward extrapolation of L1–L2 for ionospheric correction (see section A3) [cf. *Steiner et al.*, 1999]. The choice of the data interval used for extrapolation of ionospheric correction is especially different between the centers and may introduce differences in the observed magnitude.

[25] The relatively small MADs from DMI, UCAR, and WEGC is primarily due to all these three centers using the same UCAR CHAMP orbit data, excess phase, and amplitude data. Although EUM is also using the same UCAR CHAMP orbit and excess phase data, the MAD of EUM for the 8 km to 30 km layer is larger ($\sim$0.63%) than those from DMI, UCAR, and WEGC. These MAD differences are also likely caused by the different processing and smoothing approaches of the centers.

4.1.3. Refractivity (N) Difference

[26] Although different methods are used by each center for bending angle initialization of the upper boundary condition of the Abel integral [*Phinney and Anderson*, 1968], the mean refractivity anomalies among DMI, GFZ, JPL, UCAR, and WEGC (e.g., $\Delta N^{\mathrm{PPC}}_{\mathrm{DMI}}$, $\Delta N^{\mathrm{PPC}}_{\mathrm{GFZ}}$, $\Delta N^{\mathrm{PPC}}_{\mathrm{JPL}}$, $\Delta N^{\mathrm{PPC}}_{\mathrm{UCAR}}$, and $\Delta N^{\mathrm{PPC}}_{\mathrm{WEGC}}$) agree within $\pm$0.01% except for JPL (Table 2). We note that all centers incorporate MSIS (Mass Spectrometer Incoherent Scatter Radar model) climatology in some form for the initialization, except for JPL and UCAR. The mean fractional refractivity differences for $\Delta N^{\mathrm{PPC}}_{\mathrm{DMI}}$, $\Delta N^{\mathrm{PPC}}_{\mathrm{GFZ}}$, $\Delta N^{\mathrm{PPC}}_{\mathrm{JPL}}$, $\Delta N^{\mathrm{PPC}}_{\mathrm{UCAR}}$, and $\Delta N^{\mathrm{PPC}}_{\mathrm{WEGC}}$ are equal to (0.01, $-$0.01, 0.02, $-$0.01, and $-$0.01)%, respectively. Figures 3a and 3b depict the $\Delta N^{\mathrm{PPC}}_{\mathrm{UCAR}}$ and $\Delta N^{\mathrm{PPC}}_{\mathrm{JPL}}$ for all 80 months, respectively, where $\Delta N^{\mathrm{PPC}}_{\mathrm{UCAR}}$ is representative of centers with small mean differences and $\Delta N^{\mathrm{PPC}}_{\mathrm{JPL}}$ represents a center with relatively larger mean differences to the inter-center mean (see Table 2). Figure 3b shows that $\Delta N^{\mathrm{PPC}}_{\mathrm{JPL}}$ has a slightly positive mean difference relative to all the other centers. The yearly mean $\Delta N^{\mathrm{PPC}}_{\mathrm{DMI}}$, $\Delta N^{\mathrm{PPC}}_{\mathrm{GFZ}}$, $\Delta N^{\mathrm{PPC}}_{\mathrm{JPL}}$, $\Delta N^{\mathrm{PPC}}_{\mathrm{UCAR}}$, and $\Delta N^{\mathrm{PPC}}_{\mathrm{WEGC}}$, and their corresponding MADs are almost the same from 2002 to 2008 (Table 2). This indicates the long-term consistency (reproducibility) of RO data generated from individual centers.

4.1.4. Dry Temperature (T), Dry Pressure (p), and Dry Geopotential Height (Z) Differences

[27] The global mean temperature differences for DMI, GFZ, JPL, UCAR, and WEGC (i.e., $\Delta T^{\mathrm{PPC}}_{\mathrm{DMI}}$, $\Delta T^{\mathrm{PPC}}_{\mathrm{GFZ}}$, $\Delta T^{\mathrm{PPC}}_{\mathrm{JPL}}$, $\Delta T^{\mathrm{PPC}}_{\mathrm{UCAR}}$, and $\Delta T^{\mathrm{PPC}}_{\mathrm{WEGC}}$) are listed in Table 2. Figures 3c and 3d depict $\Delta T^{\mathrm{PPC}}_{\mathrm{UCAR}}$ and $\Delta T^{\mathrm{PPC}}_{\mathrm{JPL}}$ from 8 km to 30 km altitude, respectively. Table 2 shows that the mean $\Delta T^{\mathrm{PPC}}_{\mathrm{DMI}}$, $\Delta T^{\mathrm{PPC}}_{\mathrm{GFZ}}$, $\Delta T^{\mathrm{PPC}}_{\mathrm{UCAR}}$, and $\Delta T^{\mathrm{PPC}}_{\mathrm{WEGC}}$ are equal to 0.13 K, 0.01 K, 0.03 K and 0.10 K, respectively and offset the negative $\Delta T^{\mathrm{PPC}}_{\mathrm{JPL}}$ ($-$0.27 K) that increases exponentially from 15 km to 30 km (Figure 3d). The obvious negative

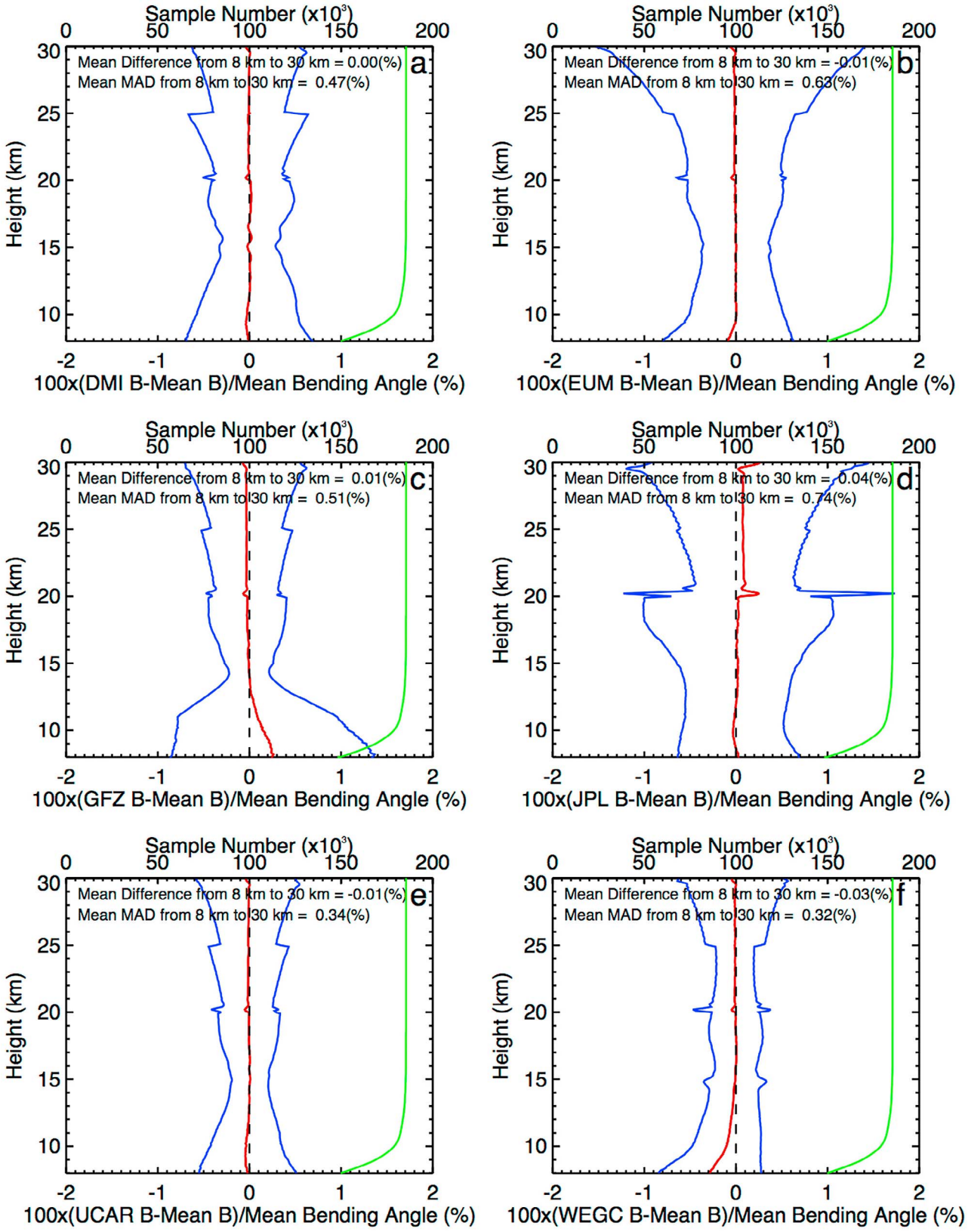

Figure 2. The mean global difference (red) and standard deviation (blue) of bending angle for (a) DMI, (b) EUM, (c) GFZ, (d) JPL, (e) UCAR, and (f) WEGC relative to the inter-center mean, for January 2002 to August 2008. The number of the matched profile pairs is denoted by the green line.

Table 2. The Mean Differences for DMI, EUM, GFZ, JPL, UCAR, WEGC Derived RO Variables From the 8 km to 30 km Layer and the Median Absolute Deviation (MAD) in the Same Height Range for Each Year and That for All the Years[a]

Center	Year	Fractional Bending Angle (%) Mean (MAD)	Fractional Refractivity (%) Mean (MAD)	Temperature (K) Mean (MAD)	Fractional Dry Pressure (%) Mean (MAD)	Geopotential Height (m) Mean (MAD)
DMI	2002	0.0 (0.45)	0.01 (0.1)	0.14 (0.51)	0.08 (0.24)	10 (20.0)
	2003	0.0 (0.46)	0.01 (0.1)	0.14 (0.51)	0.08 (0.24)	10 (20.0)
	2004	0.0 (0.47)	0.01 (0.1)	0.15 (0.51)	0.08 (0.24)	10 (10.0)
	2005	−0.01 (0.46)	0.01 (0.1)	0.15 (0.50)	0.08 (0.24)	10 (10.0)
	2006	0.0 (0.47)	0.01 (0.1)	0.09 (0.51)	0.08 (0.24)	10 (10.0)
	2007	0.0 (0.49)	0.01 (0.1)	0.12 (0.53)	0.07 (0.26)	10 (20.0)
	2008	0.0 (0.47)	0.01 (0.1)	0.10 (0.51)	0.06 (0.25)	10 (10.0)
	2002–2008	**0.0 (0.47)**	**0.01 (0.1)**	**0.13 (0.51)**	**0.07 (0.24)**	**10 (20.0)**
GFZ	2002	0.01 (0.51)	0.00 (0.18)	0.04 (0.87)	0.02 (0.49)	−10 (30.0)
	2003	0.02 (0.52)	−0.01 (0.18)	0.05 (0.91)	0.03 (0.51)	−10 (30.0)
	2004	0.01 (0.52)	−0.01 (0.18)	0.0 (0.89)	−0.01 (0.50)	−10 (30.0)
	2005	0.01 (0.51)	−0.01 (0.18)	0.01 (0.91)	0.0 (0.52)	−10 (30.0)
	2006	0.01 (0.51)	−0.01 (0.18)	−0.01 (0.96)	−0.01 (0.55)	−10 (30.0)
	2007	0.0 (0.51)	−0.02 (0.18)	−0.05 (0.98)	−0.04 (0.56)	−10 (30.0)
	2008	0.0 (0.50)	−0.01 (0.18)	0.02 (0.95)	0.0 (0.55)	−10 (30.0)
	2002–2008	**0.01 (0.51)**	**−0.01 (0.18)**	**0.01 (0.92)**	**0.0 (0.52)**	**−10 (30.0)**
JPL	2002	0.06 (0.75)	0.02 (0.17)	−0.29 (0.66)	−0.11 (0.30)	−5.8 (17.8)
	2003	0.04 (0.75)	0.02 (0.17)	−0.28 (0.65)	−0.11 (0.30)	−5.8 (17.8)
	2004	0.03 (0.75)	0.02 (0.16)	−0.29 (0.65)	−0.12 (0.30)	−5.8 (17.8)
	2005	0.06 (0.75)	0.02 (0.16)	−0.30 (0.66)	−0.12 (0.31)	−5.8 (17.8)
	2006	0.03 (0.75)	0.02 (0.16)	−0.26 (0.65)	−0.11 (0.31)	−5.8 (17.8)
	2007	0.05 (0.75)	0.02 (0.16)	−0.23 (0.65)	−0.09 (0.32)	−5.8 (17.8)
	2008	0.06 (0.73)	0.01 (0.15)	−0.22 (0.63)	−0.09 (0.30)	−5.8 (17.8)
	2002–2008	**0.04 (0.74)**	**0.02 (0.16)**	**−0.27 (0.65)**	**−0.11 (0.31)**	**−5.8 (17.8)**
UCAR	2002	−0.01 (0.34)	−0.02 (0.09)	0.02 (0.42)	0.0 (0.21)	2.3 (13.2)
	2003	−0.01 (0.34)	−0.02 (0.09)	0.02 (0.43)	−0.01 (0.22)	2.3 (13.2)
	2004	−0.01 (0.35)	−0.01 (0.09)	0.06 (0.43)	0.02 (0.22)	2.3 (13.2)
	2005	−0.01 (0.34)	−0.01 (0.09)	0.04 (0.43)	0.01 (0.22)	2.3 (13.2)
	2006	−0.01 (0.34)	−0.01 (0.09)	0.04 (0.44)	0.01 (0.23)	2.3 (13.2)
	2007	−0.01 (0.35)	−0.01 (0.09)	0.02 (0.44)	0.0 (0.23)	2.3 (13.2)
	2008	−0.01 (0.34)	−0.01 (0.09)	0.03 (0.42)	0.0 (0.22)	2.3 (13.2)
	2002–2008	**−0.01 (0.34)**	**−0.01 (0.09)**	**0.03 (0.43)**	**0.0 (0.22)**	**2.3 (13.2)**
WEGC	2002	−0.04 (0.32)	−0.02 (0.10)	0.08 (0.37)	0.02 (0.18)	3.5 (10.0)
	2003	−0.03 (0.33)	−0.02 (0.10)	0.07 (0.39)	0.01 (0.20)	3.5 (10.0)
	2004	−0.03 (0.32)	−0.01 (0.10)	0.09 (0.37)	0.03 (0.19)	3.5 (10.0)
	2005	−0.04 (0.32)	−0.01 (0.09)	0.10 (0.38)	0.03 (0.18)	3.5 (10.0)
	2006	−0.03 (0.32)	0.00 (0.09)	0.15 (0.40)	0.06 (0.20)	3.5 (10.0)
	2007	−0.03 (0.33)	0.00 (0.09)	0.14 (0.41)	0.06 (0.21)	3.5 (10.0)
	2008	−0.03 (0.32)	−0.01 (0.09)	0.08 (0.41)	0.03 (0.21)	3.5 (10.0)
	2002–2008	**−0.03(0.32)**	**−0.01 (0.09)**	**0.10 (0.39)**	**0.03 (0.20)**	**3.5 (10.0)**
EUM	2002	−0.01 (0.56)				
	2003	−0.01 (0.6)				
	2004	0.00 (0.64)				
	2005	−0.03 (0.64)				
	2006	0.00 (0.64)				
	2007	−0.02 (0.69)				
	2008	−0.03 (0.69)				
	2002–2008	**−0.01 (0.63)**				

[a]The RO-derived variables include fractional bending angle (%), fractional refractivity (%), temperature (K), fractional dry pressure (%), and geopotential height (m). To be more visible for readers, the mean differences and MADs for the period 2002 to 2008 are highlighted in bold.

$\Delta T_{\mathrm{JPL}}^{\mathrm{PPC}}$ relative to the inter-center mean above 15 km reflects the significant difference in the initialization of the hydrostatic equation between JPL and the other data centers (see section A5). JPL starts the hydrostatic equation at 40 km by assuming temperature from ECMWF, whereas the other data centers start the hydrostatic integration at 120 km. The reason that the mean MADs for DMI, UCAR, and WEGC during the period 2002 to 2008 are all close to 0.5 K is mainly that all these three centers use the same excess phase and orbit data from UCAR (see section A1). Here the inversion errors and possible impacts of hydrostatic boundary effects for temperature profile derivation are also included in the inter-center comparisons.

[28] Since the dry pressure is derived together with dry temperature from the refractivity profile (the ratio of dry pressure and dry temperature is proportional to refractivity, $N = a_1\, p/T$, a_1 = 77.6 K/hPa), the mean differences of dry pressure for each center more or less compensate both the refractivity differences and dry temperature differences (Table 2). The mean dry pressure differences for all centers are within 0.07% (mean bias from DMI) and −0.11% (mean bias from JPL). The mean dry pressure differences for UCAR are depicted in Figure 3e. Again, DMI, GFZ, UCAR, and WEGC show mean dry pressure differences that offset the −0.11% difference of JPL (Figure 3f).

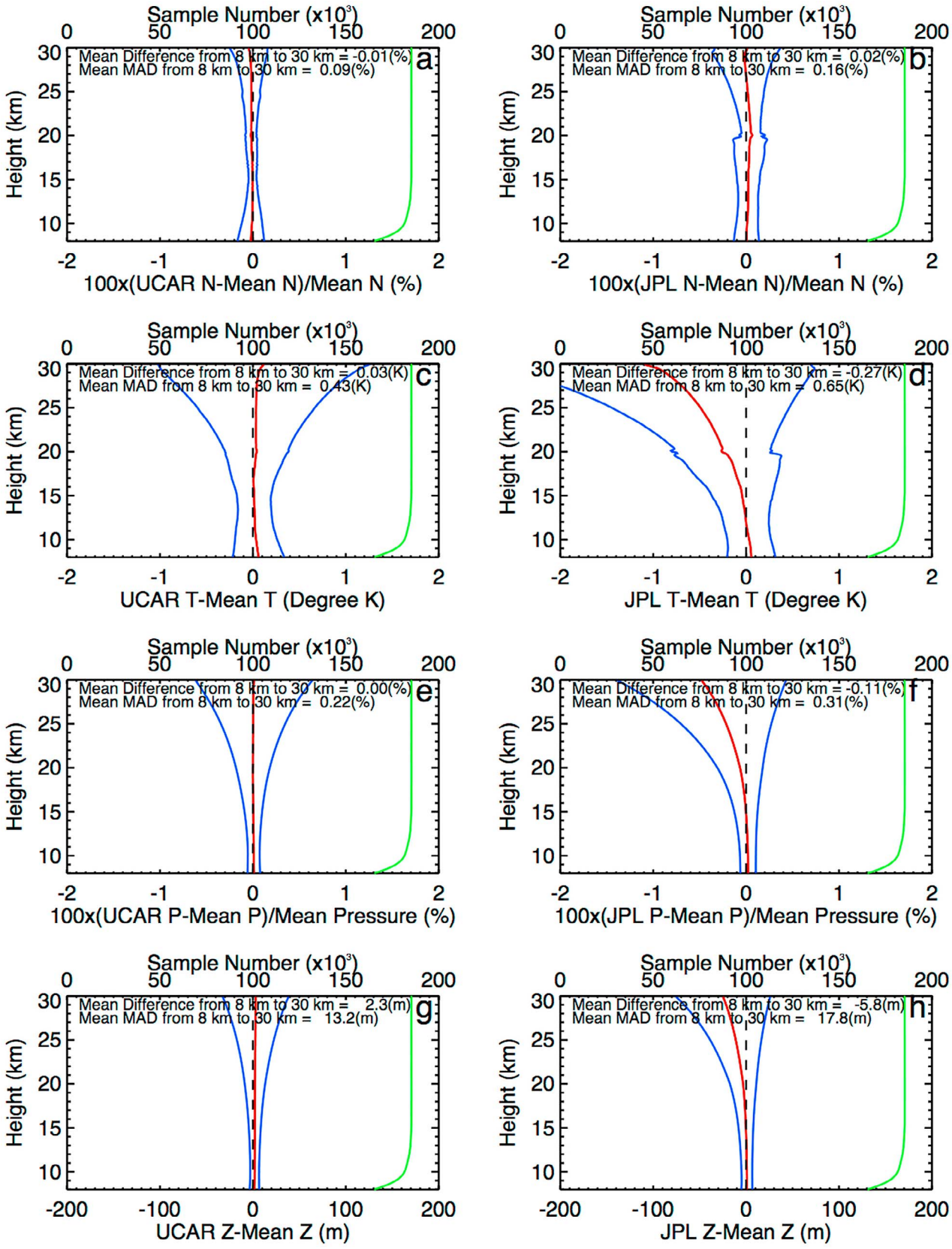

Figure 3. The mean global difference (red) and standard deviation (blue) of (a and b) refractivity, (c and d) dry temperature, (e and f) dry pressure, and (g and h) dry geopotential height shown for (left) UCAR and (right) JPL for January 2002 to August 2008. The number of the matched profile pairs is denoted by the green line.

[29] In Figure 3g we depict geopotential height differences for UCAR (ΔZ^{PPC}_{UCAR}). The standard deviation of ΔZ^{PPC}_{UCAR} at 8 km altitude is about 10 m and increases to about 50 m at 30 km altitude. The results of the global comparison for pressure and geopotential height are also listed in Table 2.

4.2. Comparison of Mean Zonal Differences

[30] The above comparisons from different centers are based on global means from 2002 to 2008. In this section we compare zonal mean differences in order to investigate small but nonzero differences among centers at different latitudes and times. Similar to *Ho et al.* [2009a], we use the following equation to generate zonal average differences for RO-derived variables for individual centers:

$$\Delta X(i,j) = (1/80) \times \sum\nolimits_{k=1}^{k=80} \left\{ X_{MPC}(i,j,k) - \overline{X_{MPC}}(i,j,k) \right\}, \quad (3)$$

where i is the index of latitude bins (5-degree), j is the index of the altitude levels (200 m from 8 km to 30 km), and k is the month index (from January 2002 to August 2008). $\overline{X_{MPC}}(i, j, k)$ is the mean of MPC of the compared variable for all centers (inter-center mean) in each latitude-, height-, and month-bin. Because there are few CHAMP data in July 2006, MPCs from that month are set to zero for all centers. In addition, we compute the MAD of differences using the following equation:

$$\Delta X^{MAD}(i,j) = (1/80) \times \sum\nolimits_{k=1}^{k=80} \left| X_{MPC}(i,j,k) - \overline{X_{MPC}}(i,j,k) \right|. \quad (4)$$

[31] Figure 4 depicts the mean fractional refractivity differences to the inter-center mean for 2007 for the five centers (i.e., ΔN_{DMI}, ΔN_{GFZ}, ΔN_{JPL}, ΔN_{UCAR}, and ΔN_{WEGC}, EUM does not produce refractivity products). The patterns of the mean fractional refractivity differences for other years are similar to this year and are not shown. In general, the fractional refractivity differences are within $\pm 0.2\%$ for all centers except for GFZ near the equator below 10 km. The slightly positive ΔN_{JPL} above 10 km along all latitudes is the result of the global positive bending angle anomalies ($\sim 0.04\%$) shown in Figure 2d. The slightly positive ΔN_{UCAR}, ΔN_{DMI}, and ΔN_{WEGC} above 15 km south of 50°S compensate the negative ΔN_{GFZ} in the same region. ΔN_{GFZ} has an obvious latitudinal bias relative to the inter-center mean (Figure 4b). It is about -0.2% above 20 km altitude in the southern mid- and high-latitudes while it is 0.2% in the northern high latitudes. These biases (not observed in the raw bending angles) are related to GFZ's approach of bending angle initialization, especially the stronger weighting of RO measurements with respect to background information (see section A4). The biases are obviously connected with a different trend behavior of GFZ's refractivity data in these regions (see Figure 10f).

[32] The corresponding two-dimensional distribution of the MAD of the fractional refractivity differences (e.g., ΔN^{MAD}_{DMI}, ΔN^{MAD}_{GFZ}, ΔN^{MAD}_{JPL}, ΔN^{MAD}_{UCAR}, and ΔN^{MAD}_{WEGC}) is shown in Figure 5. It illustrates that, even with different inversion procedures to convert raw phase data to bending angles and to refractivity, the MAD of the fractional refractivity anomalies among centers are in general smaller than 0.25% below 25 km at all latitudes. This is also partially reflecting the high precision of RO data. The ΔN^{MAD}_{DMI}, ΔN^{MAD}_{UCAR}, and ΔN^{MAD}_{WEGC} are all as small as 0.2% from 8 km to 30 km at all latitudes, which again may result from the fact that all these three centers were using the same phase and orbit data. The near 0.2% of ΔN^{MAD}_{JPL} from 15 km and 20 km altitude over the tropics could be partially due to the intrinsically higher vertical resolution of the JPL retrievals at those altitudes (200 m). The higher vertical resolution would capture the sharper structures of the tropical tropopauses. (A larger refractivity by 0.2% would correspond to colder tropopauses by about 0.4 K.) The differences among ΔN^{MAD}_{GFZ}, ΔN^{MAD}_{JPL}, and ΔN^{MAD}_{UCAR} may also reflect the upper bound uncertainty by using different orbit data and inversion procedures.

[33] In general, the precision of 0.05% in fractional refractivity is equivalent to about 0.1 K in dry temperature for temperatures at around 200 K [*Kuo et al.*, 2004; *Ho et al.*, 2009a]. This is roughly reflecting the zonal average temperature differences (i.e., ΔT_{DMI}, ΔT_{GFZ}, ΔT_{JPL}, ΔT_{UCAR}, and ΔT_{WEGC}, Figure 6) and their corresponding MAD relative to those of refractivity anomalies for each center (ΔT^{MAD}_{DMI}, ΔT^{MAD}_{GFZ}, ΔT^{MAD}_{JPL}, ΔT^{MAD}_{UCAR}, and ΔT^{MAD}_{WEGC}, Figure 7). Below 20 km, the temperature differences are in general less than 0.1 K globally. Note that we do not observe a temperature difference from JPL between 15 km and 20 km that is commensurate with the refractivity bias in the tropics. This indicates that the difference in hydrostatic integration has canceled out some of the bias. Below 25 km from 70°S to 70°N, the temperature differences are less than 0.2 K (Figure 6). The less than 0.1 K positive ΔT_{UCAR} from 70°S to 90°S compensates the 0.1 K negative ΔT_{GFZ} in the same region. The nearly 0.2 K positive ΔT_{DMI}, ΔT_{JPL}, ΔT_{UCAR}, ΔT_{WEGC} near the Tropics below 10 km offsets the negative ΔT_{GFZ} in the same region. Below 25 km, the global temperature MADs are in general less than 0.4 K except for ΔT^{MAD}_{GFZ} (Figure 7).

[34] The zonal average differences for bending angle, dry pressure and dry geopotential height more or less show similar patterns as those for fractional refractivity and dry temperature (not shown here).

4.3. Comparison of Time Series Differences

4.3.1. Analysis Method

[35] To further quantify the reproducibility and consistency of CHAMP RO data processed from different centers we compare the time series among centers. The following equation is used to calculate the differences of the time series for all investigated RO variables:

$$\Delta X^{Time}(l,m,k) = X^{Time}_{MPC}(l,m,k) - \overline{X^{Time}_{MPC}}(l,m,k), \quad (5)$$

where l is the index for different vertical layers including the 8 km to 30 km layer, the upper troposphere (UT, the 8 km to 12 km layer), the highest troposphere/lowest stratosphere (TS, the 12 km to 20 km layer), and the bulk lower stratosphere (LS, the 20 km to 30 km layer). We construct the time series comparisons for six latitudinal zones (m) including global, (90°N to 90°S), northern high-latitudes (90°N to 60°N), sub-tropical and northern midlatitudes (60°N to 20°N), Tropics (20°N to 20°S), sub-tropical and southern midlatitudes (20°S to 60°S), and southern high-latitudes (60°S to 90°S). k is the index of monthly bins (k = 1, 80) and $\overline{X^{Time}_{MPC}}(l, m, k)$ is the

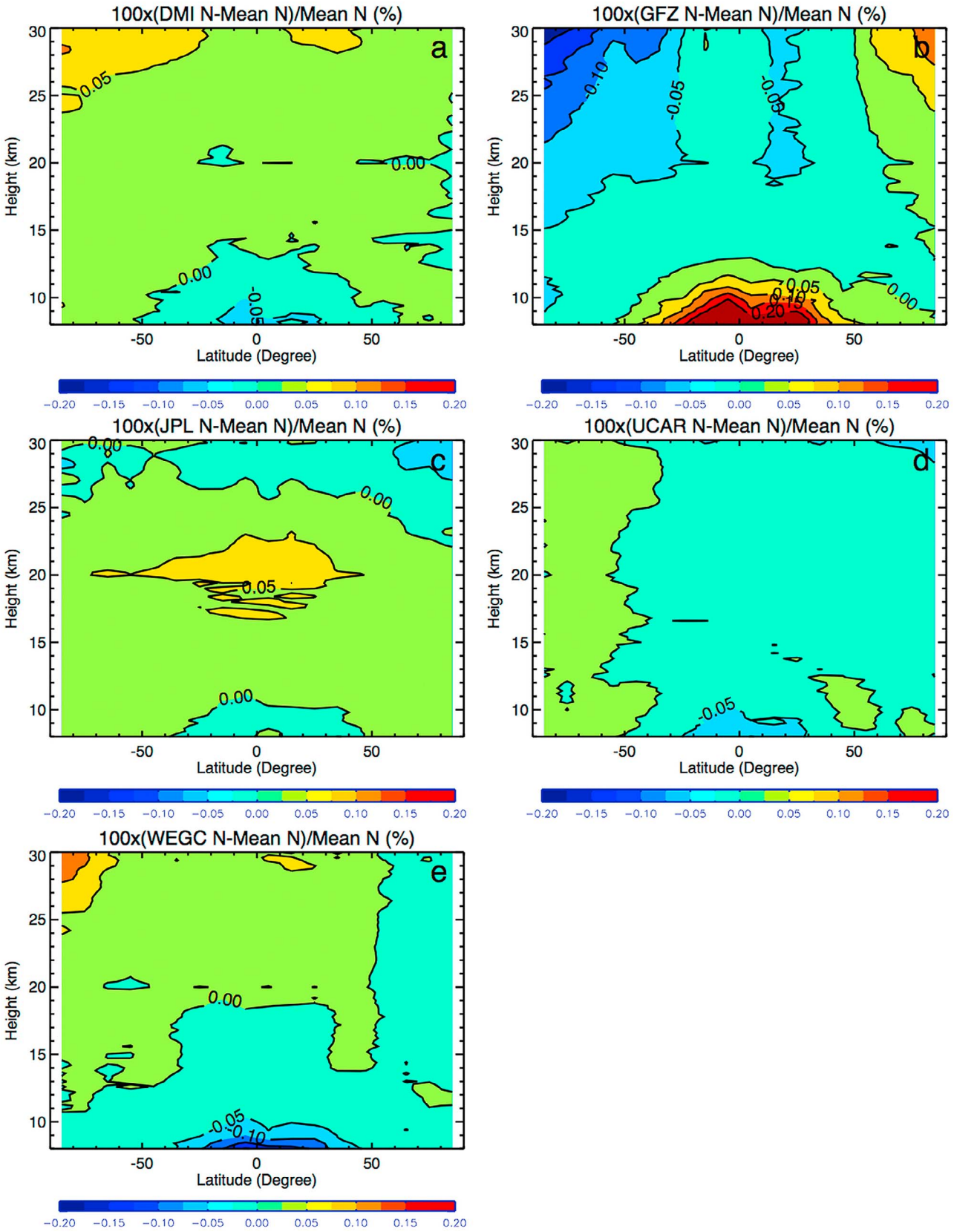

Figure 4. The mean difference of zonal-mean refractivity to the inter-model mean for (a) DMI, (b) GFZ, (c) JPL, (d) UCAR, and (e) WEGC is shown for the year 2007.

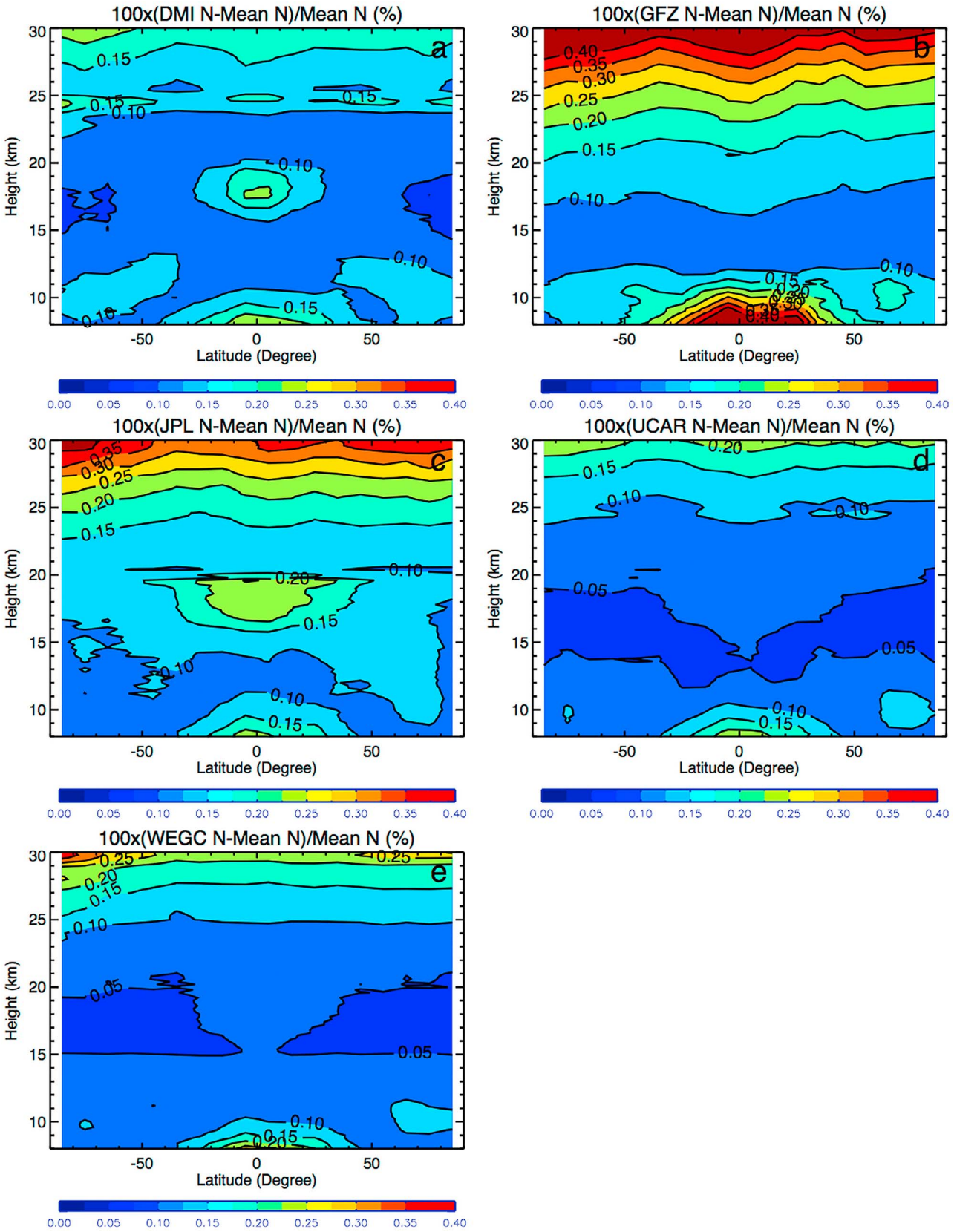

Figure 5. The Median Absolute Deviation (MAD) of zonal-mean fractional refractivity from the inter-model mean for (a) DMI, (b) GFZ, (c) JPL, (d) UCAR, and (e) WEGC is shown for 2007.

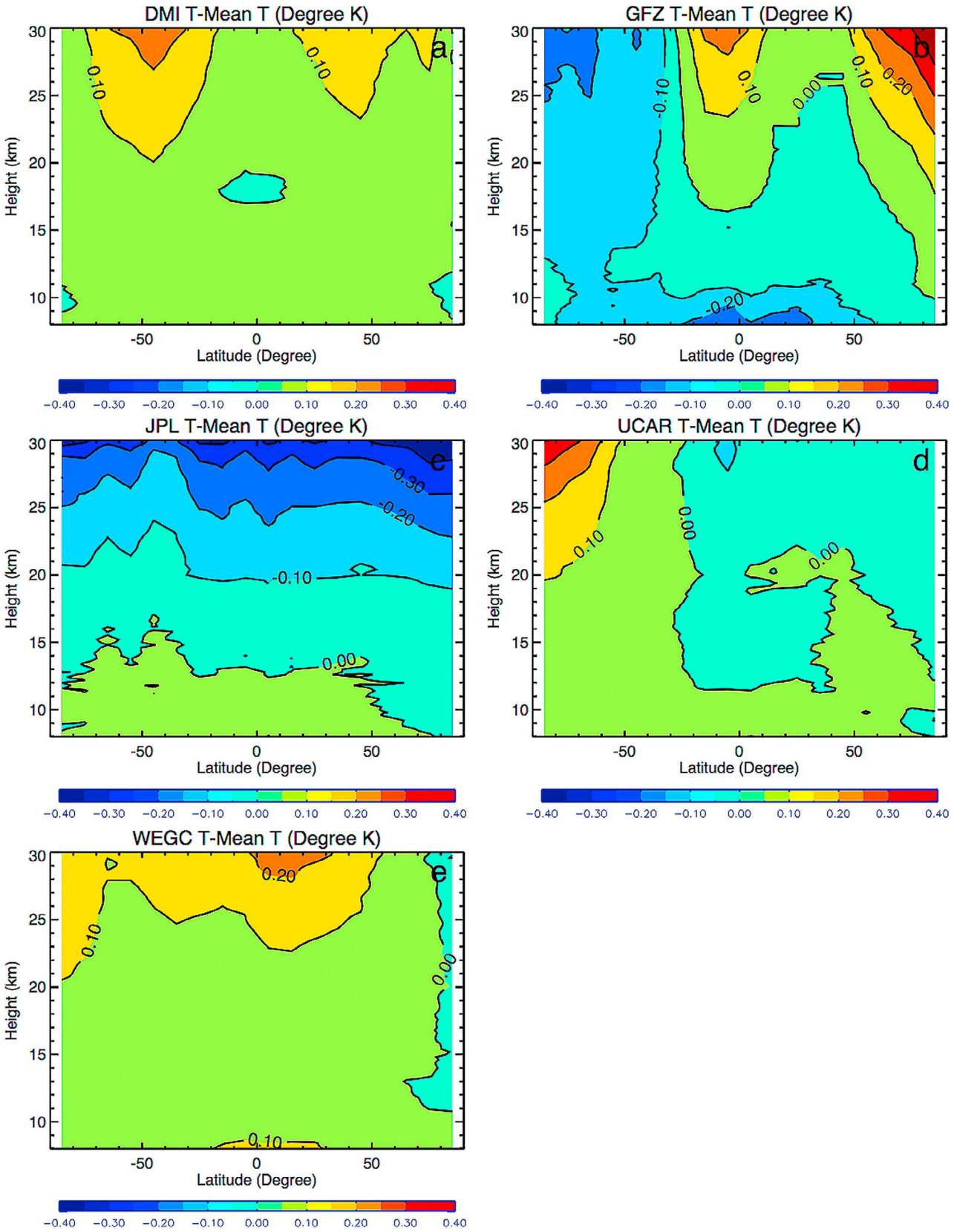

Figure 6. The mean difference of zonal-mean dry temperature to the inter-model mean for (a) DMI, (b) GFZ, (c) JPL, (d) UCAR, and (e) WEGC is shown for 2007.

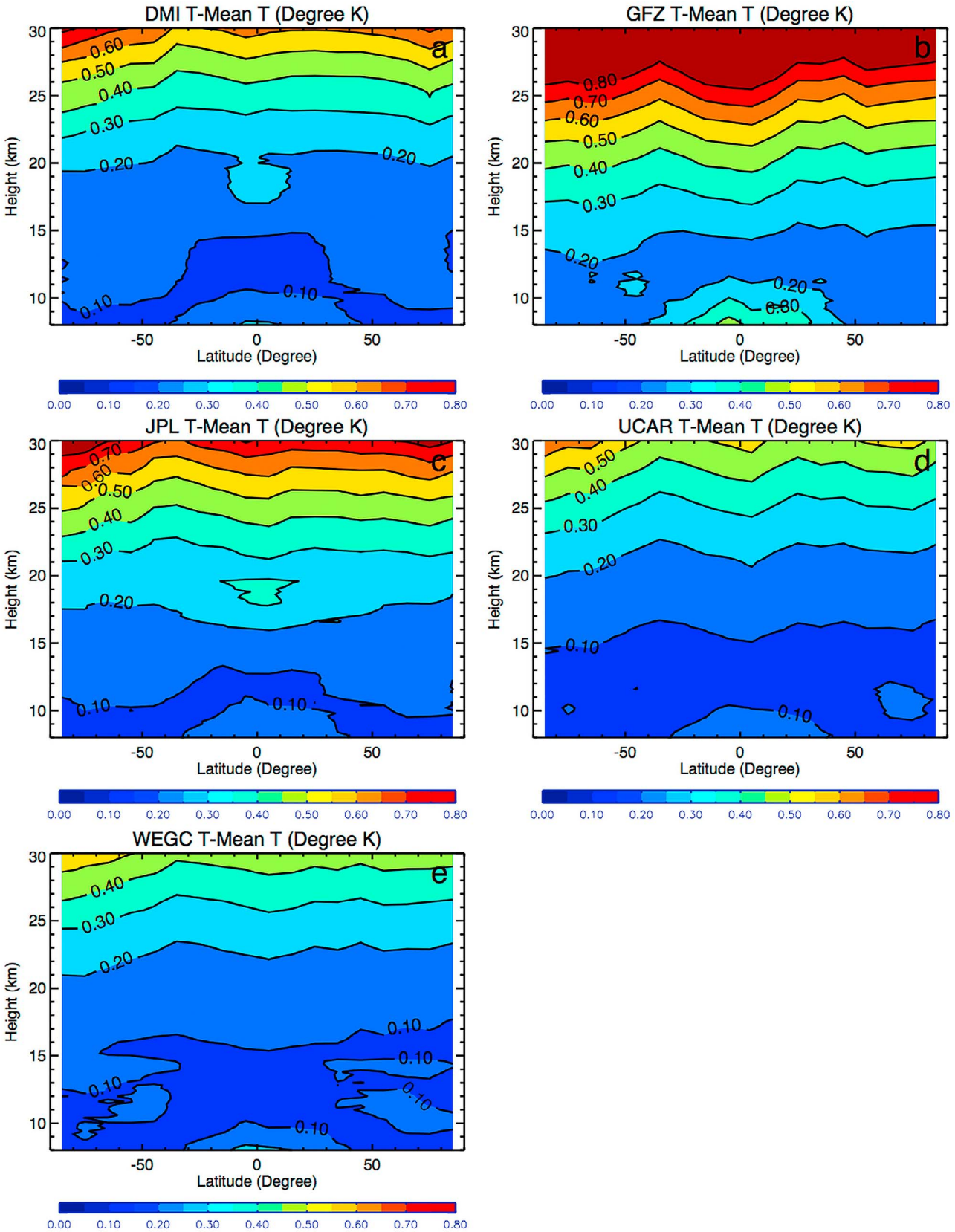

Figure 7. The Median Absolute Deviation (MAD) of zonal-mean dry temperature to the inter-model mean for (a) DMI, (b) GFZ, (c) JPL, (d) UCAR, and (e) WEGC is shown for 2007.

inter-center mean MPC for each layer-, zone-, and month-bin. Fractional time series differences (in %) are computed for bending angle, refractivity, and dry pressure. The mean and standard deviations of the time series for each center to the mean of all centers for six latitudinal zones, and at four vertical layers for fractional bending angle (%), fractional refractivity (%), fractional dry pressure (%), dry temperature (K), and dry geopotential height (m) are summarized in Tables 3–7, respectively.

[36] Note that, as mentioned in *Ho et al.* [2009a], because the inter-center mean is subtracted, results from each center need to offset the persistent or varying anomalies from an individual center by compensating behavior. The magnitude of the mean anomalies is merely used to indicate the deviation of individual centers from the inter-center mean rather than the accuracy of the time series. Here we focus on quantifying the systematic inter-center difference and inter-monthly variability among centers.

4.3.2. Time Series Differences for Bending Angle (α)

[37] Figure 8 depicts the differences of bending angle time series to the inter-center mean for DMI, EUM, GFZ, JPL, UCAR, and WEGC for the 8 km to 30 km layer (i.e., $\Delta\alpha^{\text{Time}}_{\text{DMI}}$, $\Delta\alpha^{\text{Time}}_{\text{EUM}}$, $\Delta\alpha^{\text{Time}}_{\text{GFZ}}$, $\Delta\alpha^{\text{Time}}_{\text{JPL}}$, $\Delta\alpha^{\text{Time}}_{\text{UCAR}}$, $\Delta\alpha^{\text{Time}}_{\text{WEGC}}$) for all six latitudinal zones, Figure 8a for the global, and Figures 8b–8f for the northern high-latitudes, sub-tropical and northern midlatitudes, Tropics, sub-tropical and southern midlatitudes, and southern high-latitudes, respectively. All these figures present similar qualitative features: (i) the anomalies from individual centers are persistent in time and there are no obvious latitudinal dependent biases except for $\Delta\alpha^{\text{Time}}_{\text{GFZ}}$ in the tropical region ($\sim$0.29%, Figure 8d) and small $\Delta\alpha^{\text{Time}}_{\text{JPL}}$ in the northern high-latitudes (0.14%, Table 3) and in the southern high-latitudes ($-$0.17%, Table 3), and (ii) individual center's differences show no obvious inter-monthly and inter-seasonally variance except for $\Delta\alpha^{\text{Time}}_{\text{GFZ}}$ in the Tropics (the standard deviation is $\sim$0.06%, Table 3), and in the midlatitudes (the standard deviation is $\sim$0.07%, Table 3).

[38] The mean differences for $\Delta\alpha^{\text{Time}}_{\text{DMI}}$, $\Delta\alpha^{\text{Time}}_{\text{EUM}}$, $\Delta\alpha^{\text{Time}}_{\text{GFZ}}$, $\Delta\alpha^{\text{Time}}_{\text{JPL}}$, $\Delta\alpha^{\text{Time}}_{\text{UCAR}}$, and $\Delta\alpha^{\text{Time}}_{\text{WEGC}}$ in the 8 km to 30 km layer are $-$0.01%, $-$0.02%, 0.12%, 0.02%, $-$0.02%, and $-$0.08% (Table 3), respectively. The mean standard deviations in the same layer for all centers are within 0.02%. The smallest bending angle differences among centers are found in the 12 km to 20 km layer where the mean is between $-$0.01% and 0.02% and the standard deviation is less than $\sim$0.02% (Table 3).

[39] Figure 9 depicts the time series MPC fractional bending angle differences for all six centers for northern midlatitudes, the Tropics, and the southern high-latitudes, Figures 9a, 9c, and 9e for the 8 km to 12 km layer, and Figures 9b, 9d, and 9f for the 20 km to 30 km layer. The fractional bending angle anomalies for other latitudinal zones are summarized in Table 3 and are not shown here. Figure 9a shows that $\Delta\alpha^{\text{Time}}_{\text{GFZ}}$ has a larger inter-seasonal variability with a difference of up to $\sim$0.5% in boreal hemispheric summer months (also in austral hemispheric summer months, not shown). The positive $\Delta\alpha^{\text{Time}}_{\text{GFZ}}$ bias in the 8 km to 12 km layer in the Tropics of 0.65% (Figure 9c) is mainly offset by $\Delta\alpha^{\text{Time}}_{\text{WEGC}}$ ($-$0.38%) and $\Delta\alpha^{\text{Time}}_{\text{EUM}}$ ($-$0.15%). The reason for the inter-seasonal bias below 12 km near the Tropics and sub-tropical region is probably due to differences in geometric optics and wave optics retrievals as well as differences in downward extrapolation of L1$-$L2 for ionospheric correction (see section A3). Obviously, GFZ's processing shows stronger deviations under tropical atmospheric conditions and in sub-tropical to mid-latitudinal summer. In the 20 km to 30 km layer, the inter-monthly variation of $\Delta\alpha^{\text{Time}}$ is low for all centers (Figures 9b, 9d, and 9f). $\Delta\alpha^{\text{Time}}_{\text{JPL}}$ shows a small bias of 0.19% in the northern high-latitudes and of $-$0.13% in the southern high-latitudes in the 20 km to 30 km layer (Table 3). The reason for this is not presently understood.

4.3.3. Time Series Differences for Refractivity (N)

[40] The time series of fractional refractivity differences (ΔN^{Time}) show similar qualitative features as bending angle but with a different magnitude. The mean global differences among centers in the 8 km to 30 km layer are within $\pm$0.03% with about 0.01% standard deviation (Table 4). Figure 10 depicts ΔN^{Time} for five centers (except EUM) for the northern midlatitudes, the Tropics, and the southern high-latitudes, Figures 10a, 10c, and 10e for the 8 km to 12 km layer, and Figures 10b, 10d, and 10f for the 20 km to 30 km layer. The anomalies from individual centers are in general persistent in time except at northern midlatitudes in the 8 km to 12 km layer (Figure 10a). A 0.65% of fractional bending angle bias (e.g., $\Delta\alpha^{\text{Time}}_{\text{GFZ}}$ in the Tropics for the 8 km to 12 km layer in Table 3, also see Figure 9c) is likely leading to a $\sim$0.2% of fractional refractivity bias (e.g., $\Delta N^{\text{Time}}_{\text{GFZ}}$ in the same region shown in Table 4, also see Figure 10c). The obvious inter-seasonal bias for $\Delta N^{\text{Time}}_{\text{GFZ}}$ in the sub-tropical and midlatitudes in the 8 km to 12 km layer reflects the behavior of bending angle bias in these regions.

4.3.4. Time Series Differences for Dry Pressure (p) and Dry Temperature (T)

[41] The statistics of the MPC time series differences to the inter-center mean for dry pressure and dry temperature are shown in Tables 5 and 6, respectively. Like the time series MPC for refractivity shown above, the global dry pressure time series MPC in the 8 km to 30 km layer for DMI, GFZ, JPL, UCAR, and WEGC ($\Delta p^{\text{Time}}_{\text{DMI}}$, $\Delta p^{\text{Time}}_{\text{GFZ}}$, $\Delta p^{\text{Time}}_{\text{JPL}}$, $\Delta p^{\text{Time}}_{\text{UCAR}}$, and $\Delta p^{\text{Time}}_{\text{WEGC}}$) show a small standard deviation of less than 0.02%. The mean global differences for $\Delta p^{\text{Time}}_{\text{DMI}}$, $\Delta p^{\text{Time}}_{\text{GFZ}}$, $\Delta p^{\text{Time}}_{\text{JPL}}$, $\Delta p^{\text{Time}}_{\text{UCAR}}$, and $\Delta p^{\text{Time}}_{\text{WEGC}}$ are (0.04, $-$0.04, $-$0.02, 0.00, and 0.01)%, respectively. Largest differences occur in the 20 km to 30 km layer.

[42] The global mean temperature time series differences in the 8 km to 30 km layer for DMI, GFZ, JPL, UCAR, and WEGC ($\Delta T^{\text{Time}}_{\text{DMI}}$, $\Delta T^{\text{Time}}_{\text{GFZ}}$, $\Delta T^{\text{Time}}_{\text{JPL}}$, $\Delta T^{\text{Time}}_{\text{UCAR}}$, and $\Delta T^{\text{Time}}_{\text{WEGC}}$) are 0.15 K, 0.00 K, $-$0.27 K, 0.04 K, and 0.09 K, respectively (Table 6). The variations, i.e., the corresponding standard deviations are 0.04 K, 0.06 K, 0.05 K, 0.04 K, and 0.04 K, respectively. The mean anomaly differences among centers are even smaller in the 12 km to 20 km layers (within $\pm$0.08 K, standard deviation less than 0.03 K). Differences are larger in the 20 km to 30 km layer and the 8 km to 12 km layers.

[43] Figure 11 depicts the temperature time series differences for all five centers for the northern midlatitudes, the Tropics, and the southern high-latitudes, Figures 11a, 11c, and 11e for the 8 km to 12 km layer, and Figures 11b, 11d,

Table 3. Mean and Standard Deviations of the Time Series of Fractional Bending Angle Differences for DMI, EUM, GFZ, JPL, UCAR, and WEGC to the Mean of All Six Centers for Six Latitudinal Zones, and at Four Vertical Layers[a]

Latitude Zone	Height Layers	Mean Trend (%/5 yrs)	Mean (std)/DMI–Mean Trend	Mean (std)/EUM–Mean Trend	Mean (std)/GFZ–Mean Trend	Mean (std)/JPL–Mean Trend	Mean (std)/UCAR–Mean Trend	Mean (std)/WEGC–Mean Trend
90°N to 90°S	**8 to 30 km**	**0.01**	**−0.01 (0.01)/0.00**	**−0.02 (0.02)/0.00**	**0.12 (0.02)/−0.01**	**0.02 (0.02)/0.00**	**−0.02 (0.01)/0.00**	**−0.08 (0.01)/0.02**
	8 to 12 km	0.06	−0.03 (0.01)/−0.01	−0.03 (0.02)/0.00	0.26 (0.05)/−0.01	0.00 (0.02)/−0.01	−0.03 (0.02)/−0.01	−0.16 (0.02)/0.03
	12 to 20 km	0.06	0.00 (0.00)/0.00	0.00 (0.02)/−0.01	0.00 (0.01)/−0.02	0.02 (0.02)/0.00	0.00 (0.00)/0.00	−0.01 (0.01)/0.01
	20 to 30 km	−0.25	−0.01 (0.0)/0.00	−0.01 (0.02)/−0.01	−0.04 (0.01)/0.0	0.09 (0.03)/0.00	−0.02 (0.00)/0.00	−0.01 (0.01)/0.01
60°N to 90°N	**8 to 30 km**	**−0.11**	**−0.02 (0.01)/0.00**	**0.0 (0.02)/−0.01**	**−0.02 (0.03)/−0.01**	**0.14 (0.03)/−0.01**	**−0.03 (0.02)/−0.01**	**−0.06 (0.03)/0.02**
	8 to 12 km	0.22	−0.02 (0.02)/−0.01	0.02 (0.03)/−0.01	−0.01 (0.06)/−0.02	0.12 (0.03)/0.00	−0.03 (0.03)/−0.02	−0.08 (0.04)/0.03
	12 to 20 km	0.13	−0.02 (0.01)/0.01	−0.02 (0.02)/0.00	−0.03 (0.01)/0.00	0.15 (0.03)/−0.01	−0.03 (0.01)/0.00	−0.04 (0.02)/0.02
	20 to 30 km	−0.49	−0.04 (0.01)/0.00	−0.04 (0.01)/−0.01	−0.04 (0.03)/0.02	0.19 (0.03)/−0.02	−0.04 (0.01)/−0.02	−0.04 (0.01)/0.0
60°N to 20°N	**8 to 30 km**	**0.15**	**0.00 (0.02)/−0.01**	**0.00 (0.04)/−0.01**	**0.09 (0.07)/0.00**	**−0.01 (0.04)/−0.01**	**−0.01 (0.02)/−0.01**	**−0.06 (0.03)/0.02**
	8 to 12 km	−0.11	−0.02 (0.03)/0.0	0.00 (0.05)/0.00	0.20 (0.14)/0.02	−0.03 (0.04)/−0.01	−0.03 (0.04)/−0.01	−0.12 (0.06)/0.02
	12 to 20 km	0.44	0.01 (0.0)/0.00	0.01 (0.03)/0.00	0.00 (0.01)/0.00	−0.01 (0.04)/0.00	0.0 (0.01)/0.00	−0.02 (0.02)/0.02
	20 to 30 km	0.17	0.00 (0.01)/0.00	−0.01 (0.02)/0.00	−0.02 (0.01)/0.01	0.05 (0.04)/0.00	−0.01 (0.01)/0.0	0.00 (0.01)/0.00
20°N to 20°S	**8 to 30 km**	**0.1**	**−0.04 (0.02)/0.00**	**−0.07 (0.02)/0.01**	**0.29 (0.06)/−0.03**	**0.02 (0.04)/0.00**	**−0.04 (0.02)/0.0**	**−0.17 (0.02)/0.03**
	8 to 12 km	0.19	−0.08 (0.04)/0.00	−0.15 (0.05)/0.03	0.65 (0.14)/−0.05	0.01 (0.05)/−0.02	−0.06 (0.04)/−0.01	−0.38 (0.05)/0.06
	12 to 20 km	−0.12	−0.01 (0.01)/0.00	−0.01 (0.02)/−0.01	0.03 (0.02)/−0.02	0.03 (0.02)/0.01	−0.01 (0.01)/0.00	−0.01 (0.01)/0.02
	20 to 30 km	−0.35	−0.01 (0.01)/0.00	−0.02 (0.02)/−0.01	−0.01 (0.01)/−0.01	−0.04 (0.01)/0.02	−0.04 (0.01)/0.00	−0.01 (0.01)/0.01
20°S to 60°S	**8 to 30 km**	**0.03**	**−0.03 (0.02)/0.00**	**−0.04 (0.01)/−0.02**	**0.10 (0.07)/0.00**	**0.09 (0.05)/0.01**	**−0.04 (0.02)/0.0**	**−0.09 (0.03)/0.02**
	8 to 12 km	0.04	−0.05 (0.03)/−0.01	−0.06 (0.05)/−0.01	0.26 (0.15)/0.01	0.05 (0.05)/−0.01	−0.06 (0.03)/−0.01	−0.16 (0.05)/0.02
	12 to 20 km	−0.05	−0.01 (0.01)/0.00	−0.02 (0.04)/−0.03	−0.03 (0.02)/−0.02	0.10 (0.05)/0.01	−0.02 (0.01)/0.00	−0.03 (0.01)/0.02
	20 to 30 km	0.18	−0.02 (0.01)/0.00	−0.04 (0.05)/−0.03	−0.06 (0.01)/−0.01	0.19 (0.06)/0.01	−0.03 (0.01)/0.00	−0.02 (0.01)/0.00
60°S to 90°S	**8 to 30 km**	**−0.17**	**0.05 (0.01)/0.00**	**0.06 (0.02)/0.01**	**0.01 (0.02)/−0.03**	**−0.17 (0.04)/−0.01**	**0.04 (0.01)/0.00**	**0.01 (0.03)/0.03**
	8 to 12 km	−0.09	0.05 (0.01)/0.01	0.08 (0.03)/−0.01	0.02 (0.03)/−0.02	−0.17 (0.04)/−0.01	0.04 (0.02)/−0.01	−0.01 (0.04)/0.03
	12 to 20 km	0.3	0.05 (0.01)/0.00	0.05 (0.02)/0.00	0.01 (0.02)/−0.03	−0.18 (0.04)/−0.01	0.04 (0.01)/0.00	0.03 (0.02)/0.02
	20 to 30 km	−1.03	0.04 (0.01)/0.01	0.04 (0.02)/0.01	−0.01 (0.03)/−0.04	−0.13 (0.04)/−0.01	0.03 (0.01)/0.01	0.03 (0.01)/0.02

[a]The values of standard deviations of time series of fractional bending angle differences are shown in the parentheses. The corresponding mean trends for the period 2002 to 2008 of de-seasonalized fractional bending angle anomalies (in %/5 yrs) for all centers and the DMI-mean trend of all six centers, the EUM-mean trend of all six centers, the GFZ-mean trend of all six centers, the JPL-mean trend of all six centers, the UCAR-mean trend of all six centers, and the WEGC-mean trend of all six centers. To be more visible for readers, the numbers for the 8 km to 30 km layer are highlighted in bold.

Table 4. The Same as Table 3, but for Fractional Refractivity (%)

Latitude Zone	Height Layers	Trend (%/5 yrs)	Mean (std)/DMI–Mean Trend	Mean (std)/GFZ–Mean Trend	Mean (std)/JPL–Mean Trend	Mean (std)/UCAR–Mean Trend	Mean (std)/WEGC–Mean Trend
90°N to 90°S	**8 to 30 km**	**0.02**	**0.00 (0.0)/0.00**	**0.02 (0.00)/−0.01**	**0.02 (0.00)/0.00**	**−0.01 (0.00)/0.00**	**−0.03 (0.01)/0.02**
	8 to 12 km	0.08	−0.01 (0.01)/0.01	0.07 (0.02)/−0.01	0.01 (0.01)/0.00	−0.01 (0.01)/0.00	−0.05 (0.01)/0.02
	12 to 20 km	0.46	0.01 (0.0)/0.00	−0.02 (0.01)/0.00	0.03 (0.00)/0.00	−0.01 (0.00)/0.00	−0.01 (0.01)/0.01
	20 to 30 km	−0.31	0.02 (0.0)/0.00	−0.02 (0.01)/−0.01	0.03 (0.01)/−0.01	−0.02 (0.01)/0.00	0.00 (0.01)/0.01
60°N to 90°N	**8 to 30 km**	**0.0**	**0.01 (0.01)/−0.01**	**0.00 (0.02)/0.01**	**0.02 (0.01)/−0.01**	**0.00 (0.01)/−0.01**	**−0.03 (0.01)/0.01**
	8 to 12 km	0.24	0.01 (0.01)/0.00	0.00 (0.02)/0.00	0.02 (0.01)/−0.01	0.01 (0.02)/−0.01	−0.03 (0.02)/0.02
	12 to 20 km	−0.06	0.00 (0.01)/−0.01	−0.01 (0.02)/0.00	0.02 (0.01)/−0.01	0.00 (0.01)/0.00	−0.01 (0.01)/0.00
	20 to 30 km	−0.54	0.02 (0.02)/−0.02	0.02 (0.06)/0.05	0.01 (0.03)/−0.04	−0.02 (0.02)/0.00	−0.02 (0.02)/−0.01
60°N to 20°N	**8 to 30 km**	**0.26**	**0.00 (0.01)/−0.01**	**0.02 (0.02)/0.00**	**0.02 (0.01)/−0.01**	**−0.01 (0.01)/−0.01**	**−0.03 (0.01)/0.02**
	8 to 12 km	0.13	0.00 (0.01)/0.00	0.05 (0.04)/0.00	0.01 (0.02)/−0.01	0.00 (0.02)/−0.01	−0.05 (0.02)/0.03
	12 to 20 km	0.76	0.01 (0.0)/0.00	−0.02 (0.01)/0.00	0.02 (0.01)/0.00	−0.01 (0.01)/0.00	−0.01 (0.01)/0.00
	20 to 30 km	0.09	0.01 (0.01)/−0.01	−0.02 (0.03)/0.03	0.02 (0.01)/−0.01	0.02 (0.03)/0.00	0.00 (0.01)/0.01
20°N to 20°S	**8 to 30 km**	**−0.13**	**0.00 (0.01)/−0.01**	**0.08 (0.02)/−0.01**	**0.02 (0.01)/0.00**	**−0.03 (0.01)/0.00**	**−0.05 (0.01)/0.02**
	8 to 12 km	0.02	−0.05 (0.01)/0.01	0.20 (0.02)/−0.03	−0.01 (0.01)/−0.01	−0.05 (0.01)/0.00	−0.09 (0.02)/0.02
	12 to 20 km	−0.49	0.01 (0.0)/0.00	−0.01 (0.01)/−0.01	0.04 (0.01)/0.00	−0.01 (0.00)/0.00	−0.02 (0.01)/0.00
	20 to 30 km	−0.26	0.01 (0.01)/0.01	−0.02 (0.02)/−0.01	0.04 (0.01)/−0.01	−0.02 (0.01)/0.00	0.01 (0.01)/0.01
20°S to 60°S	**8 to 30 km**	**0.05**	**0.00 (0.01)/0.00**	**0.01 (0.02)/−0.02**	**0.02 (0.01)/−0.01**	**−0.01 (0.01)/0.00**	**−0.02 (0.01)/0.01**
	8 to 12 km	0.02	−0.01 (0.01)/0.00	0.06(0.02)/−0.02	0.01 (0.01)/0.00	−0.02 (0.02)/0.00	−0.05 (0.02)/0.02
	12 to 20 km	0.24	0.01 (0.0)/0.01	−0.03 (0.01)/−0.02	0.03 (0.01)/0.01	0.00 (0.0)/0.01	−0.01 (0.01)/0.01
	20 to 30 km	0.15	0.02 (0.01)/0.01	−0.06 (0.02)/−0.02	0.04 (0.01)/−0.01	−0.04 (0.01)/0.01	0.01 (0.01)/0.02
60°S to 90°S	**8 to 30 km**	**−0.22**	**0.01 (0.01)/0.02**	**−0.03 (0.01)/−0.04**	**0.02 (0.01)/0.01**	**0.01 (0.01)/0.01**	**−0.02 (0.02)/0.03**
	8 to 12 km	0.02	0.01 (0.01)/0.02	−0.02 (0.02)/−0.03	0.02 (0.01)/0.0	0.01 (0.02)/−0.01	−0.03 (0.02)/0.02
	12 to 20 km	−0.04	0.01 (0.01)/0.00	−0.03 (0.02)/0.01	0.03 (0.01)/−0.01	0.00 (0.01)/0.00	0.00 (0.01)/0.00
	20 to 30 km	−1.47	0.03 (0.02)/0.03	−0.06 (0.06)/−0.10	0.02 (0.03)/0.01	−0.01 (0.01)/0.04	0.01 (0.02)/0.03

and 11f for the 20 km to 30 km layer. As for bending angle and refractivity, the temperature differences of individual centers are persistent in time, especially in the troposphere (the 8 km to 12 km layer). A positive $\Delta N_{\mathrm{GFZ}}^{\mathrm{Time}}$ in the 8 km to 12 km layer leads to a small negative $\Delta T_{\mathrm{GFZ}}^{\mathrm{Time}}$ in the same height (Figures 11a, 11c, and 11e). In the LS at midlatitudes and in the Tropics (Figures 11b and 11d), the temperature anomalies from individual centers are also persistent in time, consistent with refractivity behavior. The inter-seasonal variance hardly visible in $\Delta N_{\mathrm{DMI}}^{\mathrm{Time}}$ propagates to $\Delta T_{\mathrm{DMI}}^{\mathrm{Time}}$ in the 20 km to 30 km layer at high-latitudes (Figure 11f). The reason for the obvious inter-seasonal variability in $\Delta T_{\mathrm{DMI}}^{\mathrm{Time}}$ most likely originates from the inability of the MSISE-90 climatology (used in the statistical optimization, see section A4) to represent the real stratosphere and mesosphere at high-latitudes [*Gobiet and Kirchengast*, 2004; *Gobiet et al.*, 2005,

Table 5. The Same as Table 3, but for Fractional Dry Pressure (%)

Latitude Zone	Height Layers	Trend (%/5 yrs)	Mean (std)/DMI–Mean Trend	Mean (std)/GFZ–Mean Trend	Mean (std)/JPL–Mean Trend	Mean (std)/UCAR–Mean Trend	Mean (std)/WEGC–Mean Trend
90°N to 90°S	**8 to 30 km**	**−0.20**	**0.04 (0.01)/−0.01**	**−0.04 (0.02)/−0.02**	**−0.02 (0.01)/0.00**	**0.00 (0.01)/−0.01**	**0.01 (0.01)/0.02**
	8 to 12 km	−0.07	0.02 (0.00)/0.00	−0.04 (0.01)/−0.02	0.02 (0.00)/0.00	0.01 (0.01)/0.00	−0.01 (0.0)/0.02
	12 to 20 km	−0.23	0.04 (0.01)/−0.01	−0.05 (0.02)/0.02	−0.01 (0.01)/0.00	0.00 (0.01)/0.00	0.01 (0.01)/0.02
	20 to 30 km	−0.44	0.11 (0.03)/−0.03	0.03 (0.05)/−0.06	−0.19 (0.03)/0.03	0.00 (0.03)/0.01	0.05 (0.03)/0.04
60°N to 90°N	**8 to 30 km**	**−0.47**	**0.05 (0.07)/−0.05**	**0.01 (0.10)/0.12**	**−0.05 (0.05)/−0.02**	**0.01 (0.06)/−0.01**	**−0.02 (0.04)/0.00**
	8 to 12 km	−0.16	0.03 (0.03)/−0.03	−0.04 (0.05)/0.04	0.00 (0.02)/−0.01	0.02 (0.03)/−0.01	−0.02 (0.02)/0.00
	12 to 20 km	−0.38	0.05 (0.07)/−0.05	0.01 (0.10)/0.08	−0.04 (0.05)/−0.02	0.01 (0.06)/0.00	−0.02 (0.04)/0.00
	20 to 30 km	−0.59	0.15 (0.23)/−.15	0.18 (0.3)/0.23	−0.27 (0.15)/−0.03	0.01 (0.20)/−0.01	−0.05 (0.11)/−0.03
60°N to 20°N	**8 to 30 km**	**0.26**	**0.05 (0.02)/−0.03**	**−0.04(0.04)/0.03**	**−0.01 (0.02)/0.00**	**0.00 (0.02)/−0.01**	**0.01 (0.02)/0.01**
	8 to 12 km	0.30	0.03 (0.01)/−0.01	−0.06 (0.02/0.02	0.02 (0.01)/0.00	0.01 (0.01)/−0.02	−0.01 (0.01)/0.00
	12 to 20 km	0.30	0.05 (0.02)/−0.03	−0.05 (0.04)/0.02	−0.01 (0.02)/−0.01	0.00 (0.02)/0.00	0.02 (0.01)/0.02
	20 to 30 km	0.05	0.12 (0.05))/−0.08	0.04 (0.09))/0.08	−0.17 (0.05))/0.01	−0.04 (0.06))/−0.03	0.04 (0.04)/0.02
20°N to 20°S	**8 to 30 km**	**−0.11**	**0.01 (0.01)/0.01**	**0.02 (0.03)/−0.03**	**−0.01(0.01)/0.00**	**−0.03 (0.02)/−0.01**	**0.0 (0.01)/0.01**
	8 to 12 km	−0.13	0.00 (0.01)/0.01	0.02 (0.02)/−0.02	0.02 (0.01)/0.00	−0.02 (0.01)/0.00	−0.02 (0.01)/0.02
	12 to 20 km	−0.27	0.02 (0.01)/0.00	−0.01 (0.03)/−0.02	0.01 (0.01)/0.00	−0.02 (0.01)/−0.01	0.01 (0.01)/0.02
	20 to 30 km	−0.04	0.04 (0.05)/0.01	0.10 (0.09)/−0.06	−0.17 (0.05)/0.03	−0.04 (0.05)/−0.05	0.07 (0.04)/0.05
20°S to 60°S	**8 to 30 km**	**0.01**	**0.05 (0.02)/0.00**	**−0.08 (0.04)/−0.05**	**0.00 (0.02)/0.00**	**0.01 (0.02)/0.01**	**0.02 (0.02)/0.02**
	8 to 12 km	0.02	0.03 (0.01)/0.00	−0.07 (0.02)/−0.03	0.03 (0.01)/0.00	0.01 (0.01)/0.00	0.0 (0.01)/0.02
	12 to 20 km	0.03	0.05 (0.02)/0.00	−0.09 (0.04)/−0.04	0.01 (0.01)/0.00	0.01 (0.02)/0.01	0.02 (0.02)/0.02
	20 to 30 km	−0.10	0.14(0.06)/−0.01	−0.09 (0.11)/−0.12	−014 (0.05)/0.03	0.01 (0.05)/0.03	0.08 (0.05)/0.06
60°S to 90°S	**8 to 30 km**	**−0.93**	**0.06 (0.05)/0.02**	**−0.1 (0.08)/−0.15**	**−0.03 (0.04)/0.02**	**0.05 (0.03)/0.04**	**0.02 (0.04)/0.04**
	8 to 12 km	−0.42	0.04 (0.02)/0.02	−0.1 (0.04)/−0.08	0.02 (0.02)/0.01	0.04 (0.02)/0.02	0.01 (0.02)/0.02
	12 to 20 km	−0.96	0.06 (0.05)/0.02	−0.11 (0.08)/−0.14	−0.02 (0.04)/0.03	0.05 (0.03)/0.05	0.02 (0.04)/0.04
	20 to 30 km	−2.1	0.16 (0.20)/0.10	−0.1 (0.23)/−0.40	−0.23 (0.13)/0.10	0.13 (0.10)/0.20	0.05 (0.11)/0.10

Table 6. The Same as Table 3, but for Temperature (K)

Latitude Zone	Height Layers	Trend (K/5 yrs)	Mean (std)/DMI–Mean Trend	Mean (std)/GFZ–Mean Trend	Mean (std)/JPL–Mean Trend	Mean (std)/UCAR–Mean Trend	Mean (std)/WEGC–Mean Trend
90°N to 90°S	**8 to 30 km**	**−0.34**	**0.15 (0.04)/−0.05**	**0.00 (0.06)/−0.06**	**−0.27(0.05)/0.06**	**0.04 (0.04)/0.01**	**0.09 (0.04)/0.04**
	8 to 12 km	−0.34	0.07 (0.01)/−0.02	−0.24 (0.03)/0.00	0.03 (0.01)/0.01	0.04 (0.01)/0.01	0.10 (0.01)/−0.01
	12 to 20 km	−0.42	0.08 (0.02)/−0.02	−0.06 (0.03)/−0.03	−0.08 (0.02)/0.02	0.02 (0.02)/0.01	0.05 (0.02)/0.02
	20 to 30 km	−0.28	0.23 (0.07)/−0.08	0.15 (0.09)/−0.12	−0.55 (0.09)/0.12	0.05 (0.08)/−0.01	0.12 (0.07)/0.09
60°N to 90°N	**8 to 30 km**	**−0.4**	**0.19 (0.3)/−0.22**	**0.20 (0.34)/0.27**	**−0.38 (0.2)/−0.01**	**0.02 (0.27)/−0.02**	**−0.03 (0.15)/−0.03**
	8 to 12 km	−0.73	0.04 (0.06)/−0.06	−0.07 (0.10)/0.09	−0.03 (0.05)/−0.02	0.01 (0.06)/0.01	0.05 (0.06)/−0.03
	12 to 20 km	−0.53	0.10 (0.15)/−0.10	0.04 (0.19)/0.17	−0.14 (0.10)/−0.02	0.01 (0.13)/0.00	−0.02 (0.08)/−0.03
	20 to 30 km	−0.18	0.32 (0.55)/−0.36	0.43 (0.56)/0.43	−0.70 (0.35)/0.02	0.02 (0.50)/−0.01	−0.06 (0.26)/−0.07
60°N to 20°N	**8 to 30 km**	**−0.16**	**0.16 (0.09)/−0.1**	**0.01 (0.13)/0.09**	**−0.24 (0.07)/0.03**	**−0.03 (0.08)/−0.04**	**0.09 (0.06)/0.01**
	8 to 12 km	0.34	0.07 (0.02)/−0.02	−0.23 (0.07)/0.04	0.03 (0.02)/0.01	0.02 (0.04)/0.01	0.11 (0.03)/−0.01
	12 to 20 km	−0.43	0.09 (0.04/−0.05	−0.07 (0.08)/0.06	−0.07 (0.04)/0.00	0.0 (0.04)/−0.02	0.05 (0.03)/0.00
	20 to 30 km	−0.09	0.26 (0.16)/−0.17	0.18 (0.22)/0.15	−0.50 (0.12)/0.08	−0.06 (0.14)/−0.08	0.11 (0.09)/0.04
20°N to 20°S	**8 to 30 km**	**0.26**	**0.05 (0.06)/0.01**	**0.08 (0.10)/−0.06**	**−0.25 (0.07)/0.06**	**0.00 (0.06)/−0.08**	**0.13 (0.05)/0.06**
	8 to 12 km	−0.43	0.09 (0.03)/−0.01	−0.36 (0.09)/0.01	0.08 (0.03)/0.00	0.06 (0.03)/−0.01	0.13 (0.02)/−0.01
	12 to 20 km	0.09	0.01 (0.05)/0.01	0.02 (0.05)/−0.02	−0.08 (0.03)/0.02	−0.03 (0.03)/−0.02	0.07 (0.03)/0.03
	20 to 30 km	0.62	0.06 (0.11)/0.03	0.30 (0.17)/−0.11	−0.52 (0.11)/0.12	−0.01 (0.11)/−0.13	0.17 (0.09)/0.12
20°S to 60°S	**8 to 30 km**	**−0.29**	**0.18 (0.08)/−0.03**	**−0.13 (0.13)/−0.14**	**−0.22 (0.07)/0.06**	**0.04 (0.06)/0.04**	**0.13 (0.06)/0.06**
	8 to 12 km	0.02	0.08 (0.07)/−0.01	−0.28 (0.07)/−0.02	0.05 (0.02)/0.01	0.05 (0.03)/0.02	0.11 (0.02)/0.00
	12 to 20 km	−0.02	0.10 (0.04)/0.00	−0.14 (0.07)/−0.07	−0.05 (0.03)/0.02	0.03 (0.03)/0.03	0.07 (0.03)/0.03
	20 to 30 km	−0.63	0.29 (0.15)/−0.05	−0.06 (0.22)/−0.24	−0.46 (0.12)/0.12	0.04 (0.11)/0.06	0.18 (0.11)/0.11
60°S to 90°S	**8 to 30 km**	**−1.4**	**0.18 (0.27)/0.03**	**−0.12 (0.01)/−0.46**	**−0.33 (0.18)/0.13**	**0.19 (0.13)/0.18**	**0.08 (0.15)/0.12**
	8 to 12 km	−0.96	0.05 (0.05)/−0.01	−0.18 (0.07)/−0.10	−0.01 (0.04)/0.03	0.04 (0.04)/0.06	0.09 (0.04)/0.01
	12 to 20 km	−1.89	0.11 (0.12)/0.02	−0.16 (0.15)/−0.26	−0.10 (0.08)/0.06	0.10 (0.06)/0.10	0.06 (0.07)/0.06
	20 to 30 km	−1.19	0.29 (0.48)/0.04	−0.06 (0.47)/−0.77	−0.65 (0.32)/0.22	0.32 (0.24)/0.30	0.11 (0.26)/0.21

2007]. Preliminary investigations revealed that increasing the assumed error of the model profile in the statistical optimization approach at DMI reduced the inter-seasonal oscillations in the 20 km to 30 km layer at the expense of larger random noise in retrieved profiles above ~30 km. As a trade-off, the assumed model error in the DMI processing scheme was fixed at 50%, resulting in the inter-seasonal oscillations in dry temperature as seen in Figure 11f. In the 20 km to 30 km layer, $\Delta T_{\mathrm{JPL}}^{\mathrm{Time}}$ shows a negative bias in all the latitude zones. The mean global $\Delta T_{\mathrm{DMI}}^{\mathrm{Time}}$, $\Delta T_{\mathrm{GFZ}}^{\mathrm{Time}}$, $\Delta T_{\mathrm{JPL}}^{\mathrm{Time}}$, $\Delta T_{\mathrm{UCAR}}^{\mathrm{Time}}$, and $\Delta T_{\mathrm{WEGC}}^{\mathrm{Time}}$ in the LS are 0.23 K, 0.15 K, −0.55 K, 0.05 K, and 0.12 K, respectively, and the corresponding standard deviations are within 0.09 K (Table 6).

[44] On the other hand, the global highest troposphere and lowest stratosphere show low inter-monthly variance and a clear persistent anomaly. The mean $\Delta T_{\mathrm{DMI}}^{\mathrm{Time}}$, $\Delta T_{\mathrm{GFZ}}^{\mathrm{Time}}$,

Table 7. The Same as Table 3, but for Geopotential Height (m)

Latitude Zone	Height Layers	Trend (m/5 yrs)	Mean (std)/DMI–Mean Trend	Mean (std)/GFZ–Mean Trend	Mean (std)/JPL–Mean Trend	Mean (std)/UCAR–Mean Trend	Mean (std)/WEGC–Mean Trend
90°N to 90°S	**8 to 30 km**	**−18.5**	**6.8 (1.0)/−1.1**	**−7.6 (2.0)/−2.3**	**−5.6 (1.2)/1.1**	**2.5 (1.3)/0.3**	**3.9 (1.4)/2.0**
	8 to 12 km	−3.70	3.2 (0.3)/−0.1	−7.3 (0.8)/−1.1	0.86 (0.3)/0.1	2.0 (0.3)/0.1	1.2 (0.6)/1.2
	12 to 20 km	−15.2	4.8 (0.5)/−0.1	−8.9 (1.2)/−1.3	−0.76 (0.6)/0.3	2.2 (0.7)/0.3	2.7 (0.8)/1.2
	20 to 30 km	−30.3	9.8 (1.7)/−2.0	−6.7 (3.4)/−3.7	−12.0 (2.1)/2.2	2.8 (2.2)/0.4	6.0 (2.2)/3.0
60°N to 90°N	**8 to 30 km**	**−15.3**	**7.8 (8.50)/−6.5**	**−2.0 (11.9)/9.4**	**−8.6 (5.8)/−1.4**	**2.5 (7.1)/−0.6**	**0.3 (4.4)/−0.9**
	8 to 12 km	−2.90	3.5 (2.00)/−1.6	−6.28 (3.2)/1.27	−0.14 (1.38)/−0.7	2.5 (1.6)/−0.5	0.43 (1.3)/−0.4
	12 to 20 km	−23.7	5.3 (4.40)/−3.5	−5.86 (6.8)/5.6	−2.7 (3.16)/−1.3	2.6 (3.7) /−0.9	0.6 (2.4)/−0.8
	20 to 30 km	−34.0	11.6(14.5)/−10.7	2.68 (19.6)/15.3	−16.6 (9.7)/−1.9	2.5 (12.0)/−0.8	0.1 (7.4)/−1.9
60°N to 20°N	**8 to 30 km**	**10.1**	**8.2 (2.7)/−3.2**	**−9.8 (4.7)/3.6**	**−4.6 (2.3)/0.3**	**1.7 (2.5)/−1.5**	**4.4 (1.9)/0.8**
	8 to 12 km	20.4	4.0 (0.7)/−0.9	−9.6 (1.95)/0.8	1.4 (0.7)/−0.3	2.5 (0.8)/−0.6	1.7 (0.9)/0.7
	12 to 20 km	15.0	5.8 (1.4)/−1.7	−11.3 (2.8)/2.3	−0.1 (1.2)/−0.2	2.2 (1.4)/−0.8	3.4 (1.1)/0.5
	20 to 30 km	2.0	11.8 (4.5)/−5.4	−8.7 (7.6)/5.92	−10.5 (3.9)/0.86	0.9 (4.2)/−2.4	6.4 (3.2)/1.1
20°N to 20°S	**8 to 30 km**	**−12.4**	**2.4 (2.0)/0.9**	**2.0 (3.9)/−2.8**	**−6.4 (2.0)/1.1**	**−1.3 (1.9)/−1.8**	**3.3 (1.8)/2.7**
	8 to 12 km	−16.6	1.2 (0.6)/0.4	−1.2 (1.94)/−1.7	0.32(0.7)/0.0	−0.4 (0.7)/−0.2	0.04 (0.8)/1.4
	12 to 20 km	−16.0	1.9 (1.0)/0.5	−1.3 (2.4)/−1.6	−1.2(1.0)/0.3	−1.0 (1.0)/−0.7	1.6 (1.0)/1.6
	20 to 30 km	−1.40	3.2 (3.4)/1.2	6.0 (6.1)/−4.2	−13.1 (3.3)/2.2	−2.0 (3.2)/−3.5	5.9 (3.0)/4.0
20°S to 60°S	**8 to 30 km**	**−2.7**	**8.2 (2.4)/−0.5**	**−12.4 (4.7)/−4.8**	**−4.1(2.04)/1.38**	**3.0 (1.9)/1.3**	**5.3 (2.0)/2.5**
	8 to 12 km	1.6	3.6 (0.6)/−0.03	−8.9 (1.6)/−1.58	1.5 (0.6)/0.05	2.3 (0.6)/0.38	1.6 (0.7)/1.1
	12 to 20 km	2.2	5.4 (1.2)/−0.1	−11.7 (2.56)/−2.57	0.2 (1.0)/0.3	2.6 (1.1)/0.8	3.5 (1.1)/1.5
	20 to 30 km	−8.2	12.2 (4.1)/−0.9	−14.3 (7.6)/−7.9	−9.8 (3.5)/2.7	3.6 (3.2)/2.0	8.3 (3.2)/3.9
60°S to 90°S	**8 to 30 km**	**−77.8**	**8.3 (6.2)/2.0**	**−15.9 (8.9)/−15.3**	**−5.4 (4.4)/3.8**	**7.7 (3.6)/5.4**	**5.1 (4.2)/4.4**
	8 to 12 km	−19.2	4.2 (1.4)/1.1	−11.3 (3.0)/−5.1	0.94 (1.2)/1.0	4.1 (1.0)/1.4	2.1 (1.4)/1.9
	12 to 20 km	−60.3	6.2 (3.1)/1.3	−14.8 (5.2)/−9.1	−0.76 (2.4)/1.9	5.6 (2.0)/3.1	3.8 (2.3)/2.6
	20 to 30 km	−127.2	11.8 (10.6)/2.8	−18.7 (14.5)/−24.2	−11.5 (7.4)/6.3	10.9 (6.0)/−8.6	7.4 (6.9)/6.7

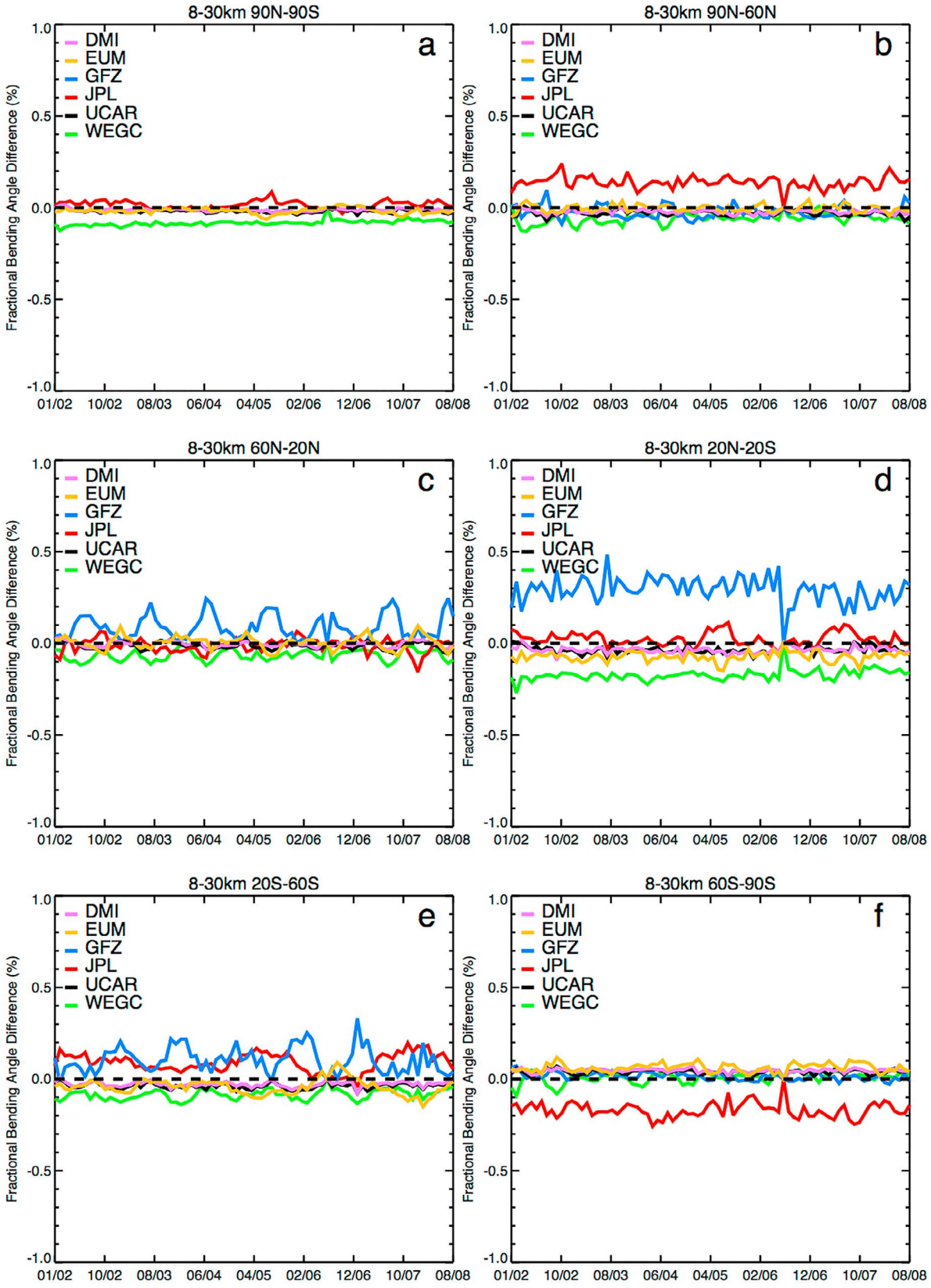

Figure 8. The time series of fractional bending angle differences among six centers for the 8 km to 30 km layer is shown for all investigated zones: (a) the entire globe (90°N to 90°S), (b) 90°N to 60°N, (c) 60°N to 20°N, (d) 20°N to 20°S, (e) 20°S to 60°S, and (f) 60°S to 90°S. The inter-model mean was subtracted on a monthly basis.

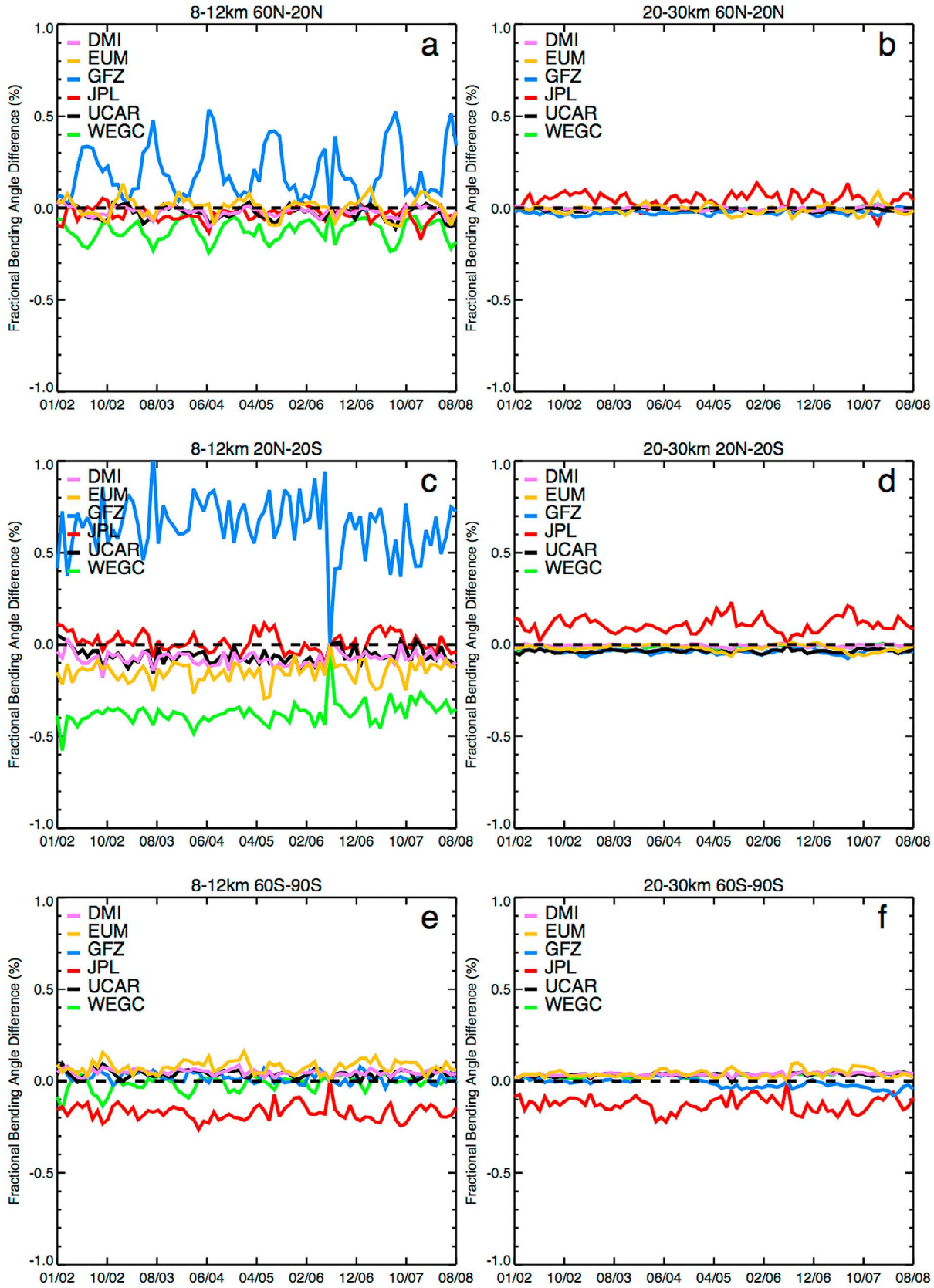

Figure 9. The time series of fractional bending angle differences among six centers are shown for the 8 km to 12 km layer for (a) the 60°N to 20°N zone, (c) the 20°N to 20°S zone, and (e) the 60°S to 90°S zone, and for the 20 km to 30 km layer for (b) the 60°N to 20°N zone, (d) the 20°N to 20°S zone, and (f) the 60°S to 90°S zone.

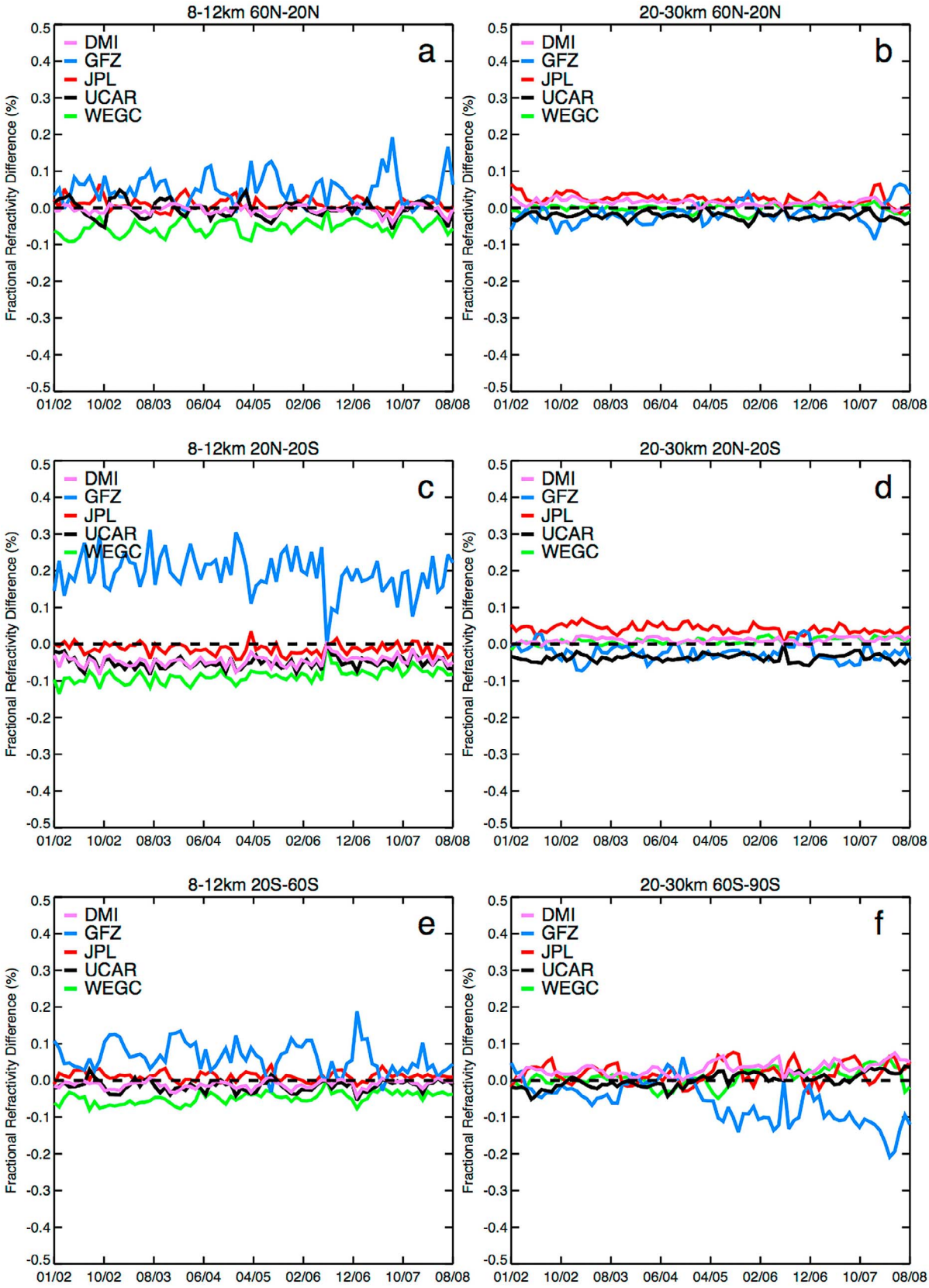

Figure 10. The time series of fractional refractivity differences among five centers are shown for the 8 km to 12 km layer for (a) the 60°N to 20°N zone, (c) the 20°N to 20°S zone, and (e) 60°S to 90°S zone, and for the 20 km to 30 km layer for (b) the 60°N to 20°N zone, (d) the 20°N to 20°S zone, and (f) the 60°S to 90°S zone.

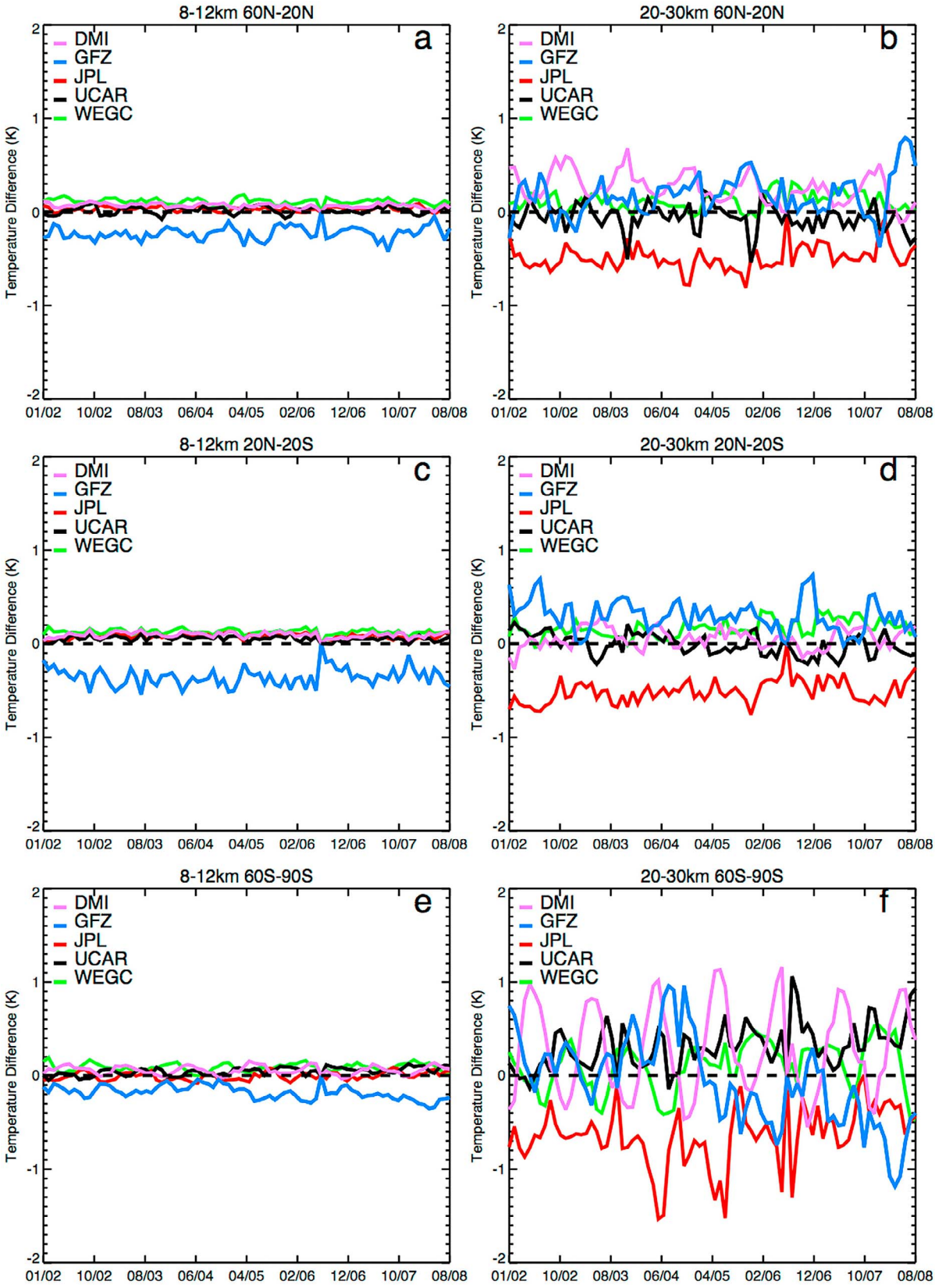

Figure 11. The time series of temperature differences among five centers are shown for the 8 km to 12 km layer for (a) the 60°N to 20°N zone, (c) the 20°N to 20°S zone, and (e) the 60°S to 90°S zone, and for the 20 km to 30 km layer for (b) the 60°N to 20°N zone, (d) the 20°N to 20°S zone, and (f) the 60°S to 90°S zone.

$\Delta T^{\text{Time}}_{\text{JPL}}$, $\Delta T^{\text{Time}}_{\text{UCAR}}$, and $\Delta T^{\text{Time}}_{\text{WEGC}}$ in the 12 km to 20 km layer are 0.08 K, −0.06 K, −0.08 K, 0.02 K, and 0.05 K, respectively, and the corresponding standard deviations are within 0.02 K to 0.03 K (Table 6).

4.3.5. Time Series Differences for Dry Geopotential Height (Z)

[45] In Figure 12 we show the MPC geopotential height time series for all five centers ($\Delta Z^{\text{Time}}_{\text{DMI}}$, $\Delta Z^{\text{Time}}_{\text{GFZ}}$, $\Delta Z^{\text{Time}}_{\text{JPL}}$, $\Delta Z^{\text{Time}}_{\text{UCAR}}$, and $\Delta Z^{\text{Time}}_{\text{WEGC}}$) in the same layout as for temperature in Figure 11. In Figure 12 the pattern of the inter-monthly variance for each center relative to the inter-center mean is very similar to that of temperature time series, especially at high-latitudes in the 20 km to 30 km layer. $\Delta Z^{\text{Time}}_{\text{DMI}}$ is offset by $\Delta Z^{\text{Time}}_{\text{JPL}}$ in the LS region at northern midlatitudes (Figure 12b). In the southern high-latitude LS region (also in the UT and TS), $\Delta Z^{\text{Time}}_{\text{GFZ}}$ shows a trend relative to the inter-center mean particularly after 2006 (Figure 12f). The global mean differences in the 8 km to 30 km layer for $\Delta Z^{\text{Time}}_{\text{DMI}}$, $\Delta Z^{\text{Time}}_{\text{GFZ}}$, $\Delta Z^{\text{Time}}_{\text{JPL}}$, $\Delta Z^{\text{Time}}_{\text{UCAR}}$, and $\Delta Z^{\text{Time}}_{\text{WEGC}}$ are 6.8 m, −7.6 m, −5.6 m, 2.5 m and 3.9 m, respectively (Table 7).

4.4. Comparison of Anomaly Differences and Trends

4.4.1. Analysis Method

[46] We quantify anomaly differences and trends of the de-seasonalized time series of the six centers. The following equation is used to derive the de-seasonalized MPC anomalies:

$$\Delta X^{\text{Deseason}}(l,m,k) = X_{\text{MPC}}(l,m,k) - \overline{X_{MPC}}(l,m,k), \qquad (6)$$

where l, m, and k are the indices for each layer (l), zone (m), and month for the whole time series (k = 1 to 80), respectively, and t is the index of the month bin of the year (t = 1 to 12). $\overline{X_{MPC}}(l, m, t)$ is the mean MPC for each layer (l), zone (m), and averaged over all years for a particular month (t). Here the $\overline{X_{MPC}}(l, m, t)$ is computed for the period from January 2002 to December 2005 since the MPC for July 2006 is not available. The mean trends of all centers and the trend difference to the mean trend for each individual center are summarized in Tables 3−7 for bending angle, refractivity, dry temperature, dry pressure, and dry geopotential height for the investigated latitudinal zones and vertical layers.

4.4.2. Anomaly Differences and Trends for Bending Angle (α) and Refractivity (N)

[47] While the trends of bending angle and refractivity anomalies from 8 km to 30 km altitudes indicate the variation of atmospheric density with time, the trends of temperature, pressure, and geopotential height represent the corresponding dry air variation in the same vertical layer under the constraint of hydrostatic equilibrium. Because the time series differences to the inter-center mean either contain systematic inter-seasonal variations (Figures 9a, 10a, and 10e) or are nearly constant with time (see Figures 8–12), the trend differences among centers are in general very small. The trends of the global de-seasonalized bending angle anomalies in the 8 km to 30 km layer for DMI, EUM, GFZ, JPL, UCAR, and WEGC ($\Delta\alpha^{\text{Deseason}}_{\text{DMI}}$, $\Delta\alpha^{\text{Deseason}}_{\text{EUM}}$, $\Delta\alpha^{\text{Deseason}}_{\text{GFZ}}$, $\Delta\alpha^{\text{Deseason}}_{\text{JPL}}$, $\Delta\alpha^{\text{Deseason}}_{\text{UCAR}}$, and $\Delta\alpha^{\text{Deseason}}_{\text{WEGC}}$) are (0.01, 0.01, 0.0, 0.01, 0.01, and 0.03)%/5 yrs, respectively, where the trend differences to the mean trend are within ±0.02%/5 yrs in the same layer (Table 3). Even though $\Delta\alpha^{\text{Time}}_{\text{JPL}}$ has a persistent bias at southern (−0.17%) and northern high-latitudes (0.14%) in the 8 km to 30 km layer, the trend of $\Delta\alpha^{\text{Deseason}}_{\text{JPL}}$ is very close to the trends of the other centers (the trend difference of $\Delta\alpha^{\text{Deseason}}_{\text{JPL}}$ is equal −0.01%/5 yrs, Table 3), because the variation of $\Delta\alpha^{\text{Time}}_{\text{JPL}}$ is very small (less than 0.04%, Table 3).

[48] Although the $\Delta\alpha^{\text{Time}}_{\text{GFZ}}$ contains obvious inter-seasonal variation in the 8 km to 12 km layer in the northern midlatitudes (Figure 9a), the trend difference between GFZ and the mean trend is equal to 0.02%/5 yrs. Because $\Delta\alpha^{\text{Time}}_{\text{GFZ}}$ in the Tropics for the 8 km to 12 km layer is slightly decreased after August 2006 (Figure 9c), $\Delta\alpha^{\text{Deseason}}_{\text{GFZ}}$ shows a slightly decreasing trend (−0.05%/5 yrs) relative to the mean trends (Table 3). The largest trend variability is over southern high-latitudes where $\Delta\alpha^{\text{Time}}_{\text{GFZ}}$ also shows a decreasing trend (−0.04%/5 yrs) relative to the mean trend. The fractional bending angle trend difference among centers is within ±0.01%/5 years for the 20 km to 30 km layer (Table 3).

[49] *Ho et al.* [2009a] used daily NCEP (National Centers for Environmental Prediction) reanalysis [*Saha et al.*, 2010] (on a 6-h and 1-degree bin) to estimate sampling errors from the respective monthly mean climatologies (similar to *Pirscher et al.* [2007] and *Foelsche et al.* [2008b]). After removing the representative sampling errors, *Ho et al.*, 2009a showed that the uncertainty of the trend for fractional refractivity anomalies among centers was between −0.03%/5 yrs and 0.01%/5 yrs. As stated in *Ho et al.*, 2009a, the sampling errors estimation may be less accurate at high altitudes over southern/northern high-latitudes due to possible temporal and spatial representation errors from NCEP reanalysis. In this study sampling error is not an issue since we use matched profile pairs. We identify that the uncertainty of the trend of the fractional refractivity is within −0.01%/5 yrs to 0.02%/5 yrs (less than ±0.02%/5 yrs) globally (Table 4) which is even smaller than that from *Ho et al.*, 2009a. The mean trend for global $\Delta N^{\text{Deseason}}_{\text{DMI}}$, $\Delta N^{\text{Deseason}}_{\text{GFZ}}$, $\Delta N^{\text{Deseason}}_{\text{JPL}}$, $\Delta N^{\text{Deseason}}_{\text{UCAR}}$, and $\Delta N^{\text{Deseason}}_{\text{WEGC}}$ in the 8 km to 30 km layer is (0.02, 0.01, 0.02, 0.02, and 0.04)%/5 yrs, respectively.

[50] Figure 13 depicts de-seasonalized fractional refractivity anomalies for each center for the northern midlatitudes, the Tropics, and the southern high-latitudes. Figures 13a, 13c, and 13e are for the 12 km to 20 km layer and Figures 13b, 13d, and 13f are for the 20 km to 30 km layer. In general, the trend differences in the 12 km to 20 km layer in all latitudinal zones are very close to zero, except for in the southern midlatitudes (Table 4). In this region, the trend difference to the mean trend for GFZ is equal to −0.02%/5 yrs whereas those for all the other centers are close to 0.00%/5 yrs (the rounded values). Over the Tropics in the LS region, the trend differences among the centers are within ±0.01%/5 yrs (Table 4). Over the southern high-latitudes in the LS region (Figure 13f), the trend of $\Delta N^{\text{Deseason}}_{\text{GFZ}}$ is equal to −1.57%/5 yrs whereas the trends of the other centers are all within −1.43%/5 yrs ($\Delta N^{\text{Deseason}}_{\text{UCAR}}$) and −1.46%/5 yrs ($\Delta N^{\text{Deseason}}_{\text{JPL}}$). This relatively large trend difference for GFZ in this region is mainly due to the large negative fractional refractivity differences ($\Delta T^{\text{Time}}_{\text{GFZ}}$) after 2004 (Figure 10f). This is more pronounced in the temperature trend differences (see below).

[51] To quantify the degree of deviation among the centers, we also compute the RMS difference between $\Delta N^{Deseason}$ and

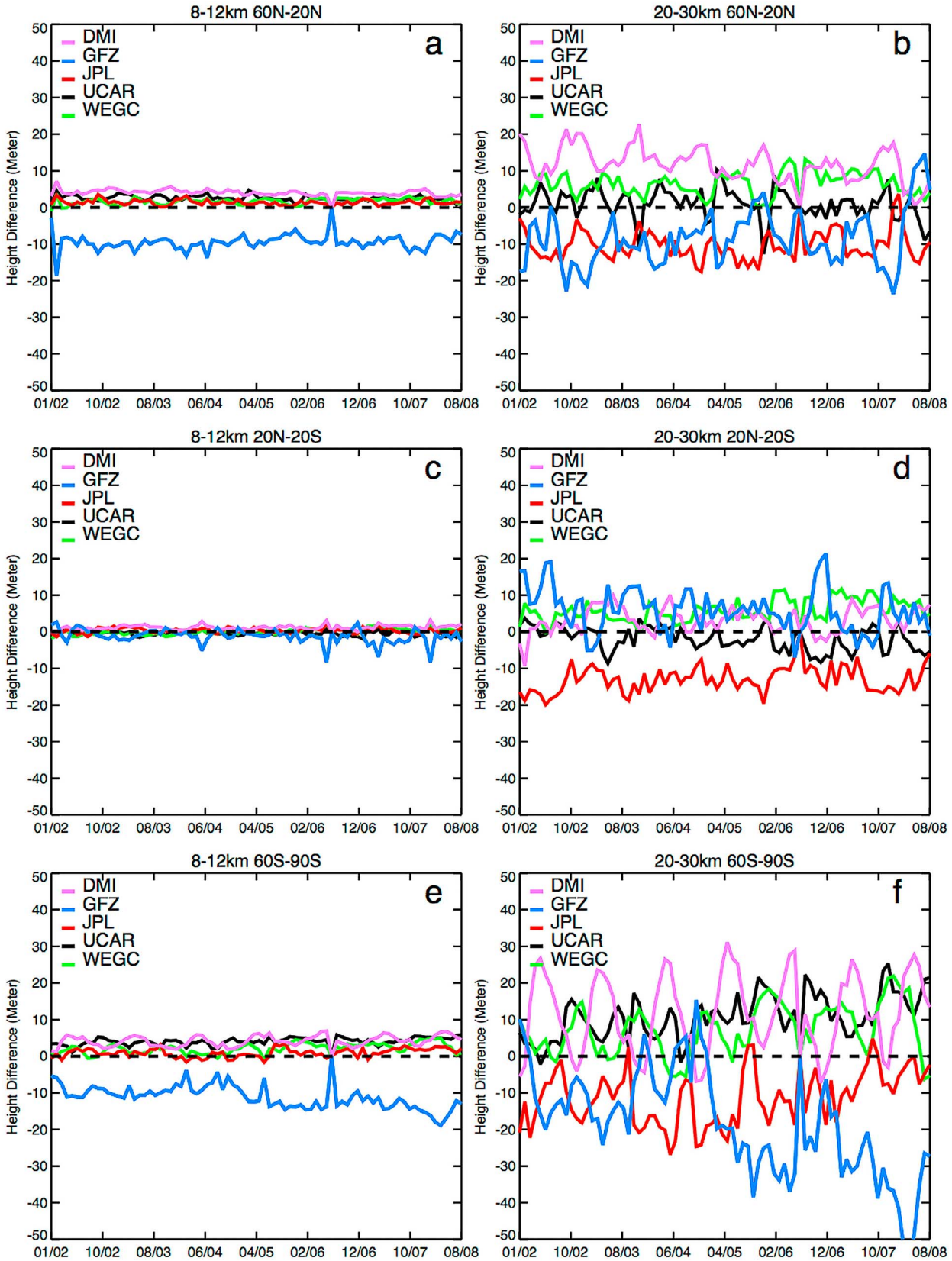

Figure 12. The time series of geopotential height differences among five centers are shown for the 8 km to 12 km layer for (a) the 60°N to 20°N zone, (c) the 20°N to 20°S zone, and (e) the 60°S to 90°S zone, and for the 20 km to 30 km layer for (b) the 60°N to 20°N zone, (d) the 20°N to 20°S zone, and (f) the 60°S to 90°S zone.

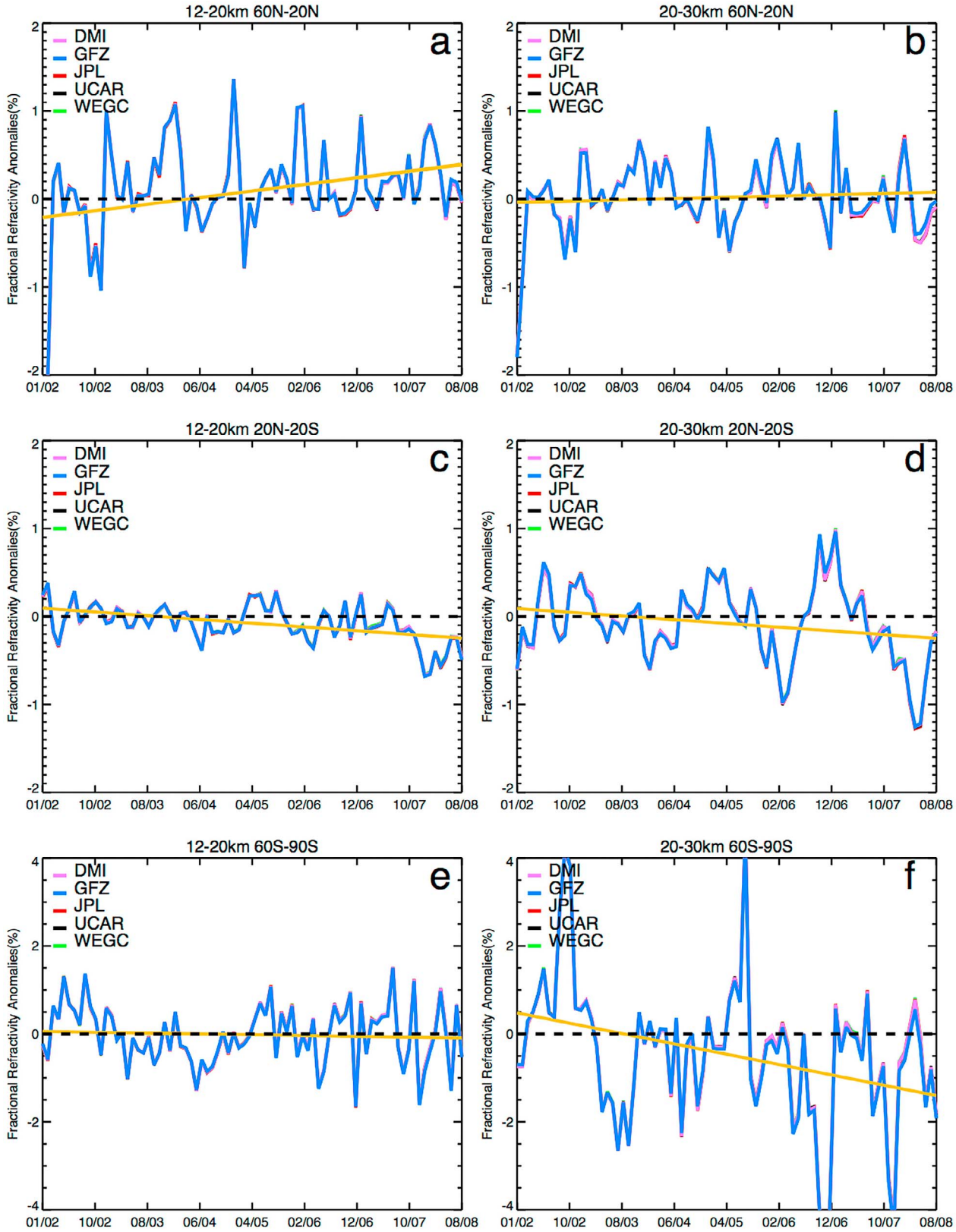

Figure 13. The de-seasonalized fractional refractivity anomalies for each center in the 12 km to 20 km layer for (a) the 60°N to 20°N zone, (c) the 20°N to 20°S zone, and (e) the 60°S to 90°S zone, and for the 20 km to 30 km layer for (b) the 60°N to 20°N zone, (d) the 20°N to 20°S zone, and (f) the 60°S to 90°S zone. The 5-yr trend of the inter-center mean is shown as well. Note that the ordinate range in Figures 13e and 13f is enlarged to ±4% (relative to ±2% of Figures 13a–13d).

Table 8. The Same as Table 3, but for Mean Root Mean Square (RMS) of the Differences of De-seasonalized Time Series Anomalies to the Inter-center Mean for DMI, GFZ, JPL, UCAR, and WEGC for Fractional Refractivity (%) and Temperature (K)

Latitude Zone	Height Layer	DMI-Mean N (%)/T (K)	GFZ-Mean N (%)/T (K)	JPL-Mean N (%)/T (K)	UCAR-Mean N (%)/T (K)	WEGC-Mean N (%)/T (K)
90°N to 90°S	**8 to 30 km**	**0.00/0.03**	**0.01/0.04**	**0.00/0.05**	**0.00/0.04**	**0.01/0.04**
	8 to 12 km	0.01/0.01	0.02/0.03	0.01/0.01	0.01/0.01	0.01/0.01
	12 to 20 km	0.00/0.02	0.01/0.02	0.00/0.02	0.00/0.02	0.00/0.02
	20 to 30 km	0.00/0.06	0.01/0.08	0.01/0.09	0.00/0.07	0.00/0.07
60°N to 90°N	**8 to 30 km**	**0.01/0.13**	**0.02/0.25**	**0.01/0.19**	**0.01/0.23**	**0.01/0.11**
	8 to 12 km	0.01/0.03	0.02/0.08	0.01/0.04	0.02/0.05	0.02/0.04
	12 to 20 km	0.01/0.07	0.02/0.15	0.01/0.09	0.01/0.11	0.01/0.06
	20 to 30 km	0.01/0.23	0.02/0.41	0.01/0.32	0.01/0.39	0.01/0.19
60°N to 20°N	**8 to 30 km**	**0.01/0.05**	**0.02/0.12**	**0.01/0.06**	**0.01/0.07**	**0.01/0.05**
	8 to 12 km	0.01/0.02	0.03/0.05	0.01/0.02	0.02/0.03	0.02/0.03
	12 to 20 km	0.00/0.03	0.01/0.07	0.01/0.03	0.01/0.04	0.01/0.03
	20 to 30 km	0.01/0.1	0.03/0.2	0.01/0.11	0.01/0.12	0.01/0.08
20°N to 20°S	**8 to 30 km**	**0.01/0.05**	**0.02/0.10**	**0.01/0.07**	**0.01/0.06**	**0.01/0.05**
	8 to 12 km	0.02/0.03	0.05/0.09	0.01/0.03	0.01/0.03	0.02/0.02
	12 to 20 km	0.01/0.02	0.01/0.05	0.01/0.03	0.00/0.02	0.01/0.02
	20 to 30 km	0.01/0.09	0.02/0.16	0.01/0.11	0.01/0.11	0.01/0.08
20°S to 60°S	**8–30 km**	**0.01/0.05**	**0.02/0.12**	**0.01/0.06**	**0.01/0.06**	**0.01/0.05**
	8 to 12 km	0.01/0.02	0.03/0.06	0.01/0.02	0.01/0.02	0.01/0.02
	12 to 20 km	0.00/0.02	0.01/0.06	0.01/0.03	0.00/0.03	0.01/0.02
	20 to 30 km	0.01/0.09	0.02/0.20	0.01/0.11	0.01/0.09	0.01/0.08
60°S to 90°S	**8 to 30 km**	**0.01/0.07**	**0.02/0.25**	**0.01/0.14**	**0.01/0.12**	**0.02/0.10**
	8 to 12 km	0.01/0.02	0.03/0.07	0.01/0.03	0.02/0.04	0.02/0.03
	12 to 20 km	0.00/0.40	0.02/0.14	0.0/10.06	0.01/0.06	0.01/0.05
	20 to 30 km	0.01/0.12	0.06/0.42	0.01/0.25	0.02/0.20	0.02/0.17

the mean of $\Delta N_{\mathrm{DMI}}^{\mathrm{Deseason}}$, $\Delta N_{\mathrm{GFZ}}^{\mathrm{Deseason}}$, $\Delta N_{\mathrm{JPL}}^{\mathrm{Deseason}}$, $\Delta N_{\mathrm{UCAR}}^{\mathrm{Deseason}}$, and $\Delta N_{\mathrm{WEGC}}^{\mathrm{Deseason}}$ for each center (i.e., ΔN_{DMI}^{RMS}, ΔN_{GFZ}^{RMS}, ΔN_{JPL}^{RMS}, ΔN_{UCAR}^{RMS}, ΔN_{WEGC}^{RMS}, see Table 8). The global RMS for all centers are within 0.02% for all latitudinal zones except for RMSGFZ at high-latitudes and mostly in the 8 km to 12 km layer.

4.4.3. Anomaly Differences and Trends for Dry Temperature (T), Dry Pressure (p), and Dry Geopotential Height (Z)

[52] Similar to *Ho et al.* [2009a], the trend derived by each individual center is still statistically insignificant although in total only 80 months of data are used. It may take about 10 years of RO data to obtain statistically significant trends [*Leroy et al.*, 2006; *Foelsche et al.*, 2008a; *Ringer and Healy*, 2008]. Here we aim at quantifying the trend differences among centers when the sampling errors and the natural variability, which is common on individual center trends, are completely removed.

[53] Figure 14 depicts the de-seasonalized temperature anomalies for DMI, GFZ, JPL, UCAR, and WEGC ($\Delta T_{\mathrm{DMI}}^{\mathrm{Deseason}}$, $\Delta T_{\mathrm{GFZ}}^{\mathrm{Deseason}}$, $\Delta T_{\mathrm{JPL}}^{\mathrm{Deseason}}$, $\Delta T_{\mathrm{UCAR}}^{\mathrm{Deseason}}$, and $\Delta T_{\mathrm{WEGC}}^{\mathrm{Deseason}}$) for the northern midlatitudes, the Tropics, and the southern high-latitudes. Figures 14a, 14c, and 14e are for the 12 km to 20 km layer, and Figures 14b, 14d, and 14f are for the 20 km to 30 km layer. The temperature anomalies for other latitudinal zones are similar to those in Figure 14 and are not shown here. The trends for $\Delta T_{\mathrm{DMI}}^{\mathrm{Deseason}}$, $\Delta T_{\mathrm{GFZ}}^{\mathrm{Deseason}}$, $\Delta T_{\mathrm{JPL}}^{\mathrm{Deseason}}$, $\Delta T_{\mathrm{UCAR}}^{\mathrm{Deseason}}$, and $\Delta T_{\mathrm{WEGC}}^{\mathrm{Deseason}}$ in the 12 km to 20 km layer agree within ±0.03 K/5 yrs, because their differences are constant over time with a standard deviation of 0.03 K (Table 6). The global trend differences for each center in the 8 km to 12 km layer are within ±0.02 K/5 yrs and within ±0.06 K/5 yrs in the 8 km to 30 km layer (Table 6).

[54] The trends of $\Delta T_{\mathrm{DMI}}^{\mathrm{Deseason}}$, $\Delta T_{\mathrm{GFZ}}^{\mathrm{Deseason}}$, $\Delta T_{\mathrm{JPL}}^{\mathrm{Deseason}}$, $\Delta T_{\mathrm{UCAR}}^{\mathrm{Deseason}}$, and $\Delta T_{\mathrm{WEGC}}^{\mathrm{Deseason}}$ in the 20 km to 30 km layer show larger deviations (Figures 14b, 14d, and 14f) especially at high-latitudes. Figures 14b, 14d, and 14f show that the systematic temperature biases to the inter-center mean for JPL and GFZ over northern midlatitudes (Figure 11b), Tropics (Figure 11d), and in northern high-latitude zone (not shown), and the systematic inter-seasonal temperature biases for DMI in the southern high-latitudes (Figure 11f) are largely removed in the de-seasonalized anomalies. The trend difference for $\Delta T_{\mathrm{DMI}}^{\mathrm{Deseason}}$ to the mean trend in the southern high-latitudes is equal to 0.04 K/5 yrs in the LS (Table 6). However, the anomaly trend differences for $\Delta T_{\mathrm{DMI}}^{\mathrm{Deseason}}$ in northern high-latitudes and northern midlatitudes are still as large as −0.36 K/5 yrs and −0.17 K/5 yrs, respectively (Table 6).

[55] In addition, Figure 15 shows the differences of de-seasonalized temperature anomalies ($\Delta T^{Deseason}$) for each center to the mean de-seasonalized temperature anomalies for the northern midlatitudes, the Tropics, and the southern high-latitudes. Figures 15a, 15c, and 15e are for the 8 km to 12 km layer, and Figures 15b, 15d, and 15f are for the 20 km to 30 km layer. RMS differences between $\Delta T^{Deseason}$ and the mean of $\Delta T_{\mathrm{DMI}}^{\mathrm{Deseason}}$, $\Delta T_{\mathrm{GFZ}}^{\mathrm{Deseason}}$, $\Delta T_{\mathrm{JPL}}^{\mathrm{Deseason}}$, $\Delta T_{\mathrm{UCAR}}^{\mathrm{Deseason}}$, and $\Delta T_{\mathrm{WEGC}}^{\mathrm{Deseason}}$ (i.e., ΔT_{DMI}^{RMS}, ΔT_{GFZ}^{RMS}, ΔT_{JPL}^{RMS}, ΔT_{UCAR}^{RMS}, ΔT_{WEGC}^{RMS}) for each center in different vertical layers are shown in Table 8. Due to decreasing negative temperature anomalies ($\Delta T_{\mathrm{GFZ}}^{\mathrm{Time}}$) after 2004 (Figure 11f) particularly over southern high-latitudes in the 20 km to 30 km layer, the trend difference for $\Delta T_{\mathrm{GFZ}}^{\mathrm{Deseason}}$ to the mean trend is as large as −0.77 K/5 yrs (Table 6) where the RMS temperature difference for GFZ (i.e., ΔT_{GFZ}^{RMS}) in the same region is equal to 0.42 K (Table 8).

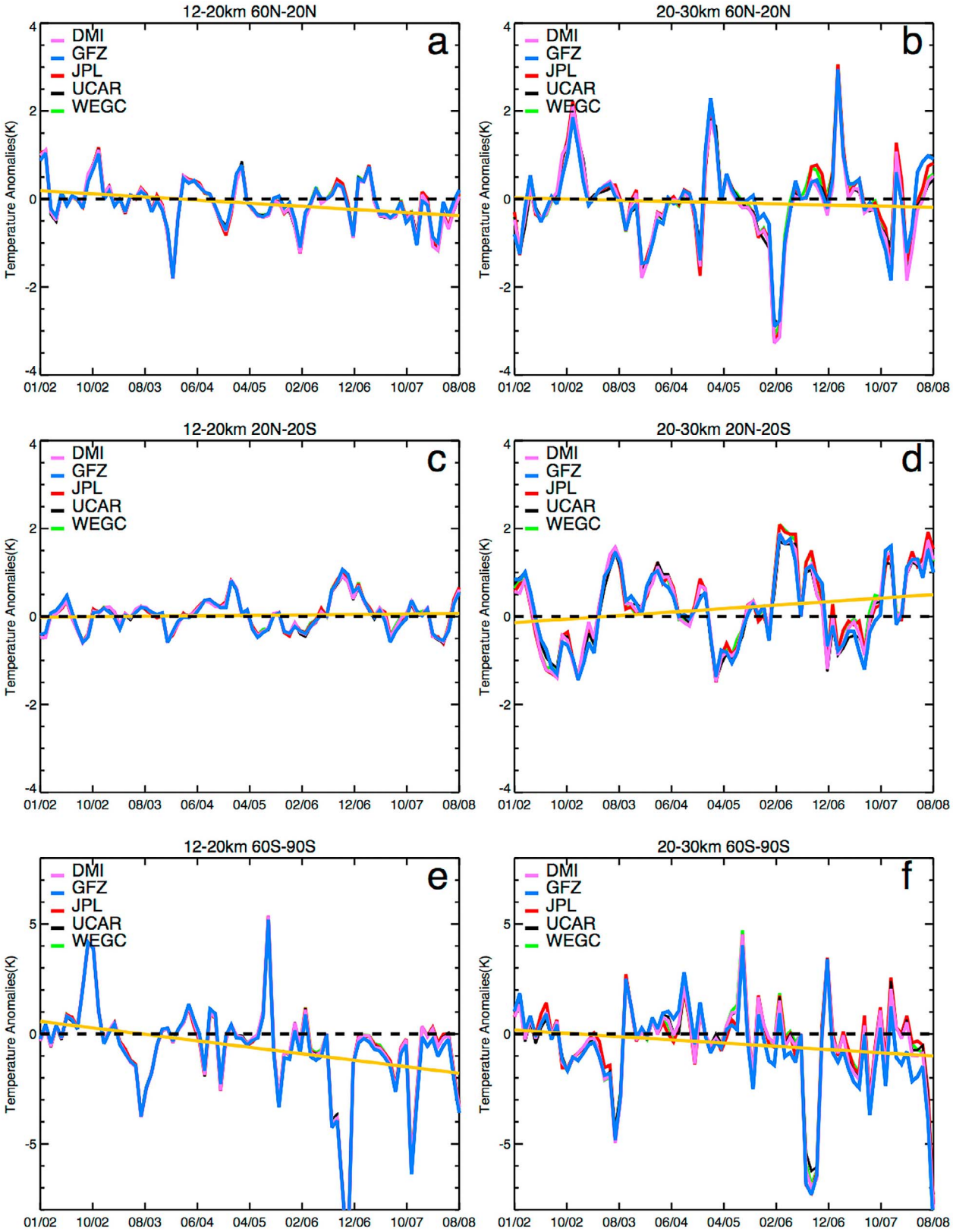

Figure 14. The de-seasonalized temperature anomalies for each center in the 12 km to 20 km layer for (a) the 60°N to 20°N zone, (c) the 20°N to 20°S zone, and (e) the 60°S to 90°S zone, and in the 20 km to 30 km layer for (b) the 60°N to 20°N zone, (d) the 20°N to 20°S zone, and (f) the 60°S to 90°S zone. The 5-yr trend of the inter-center mean is shown as well. Note that the ordinate range of Figures 14e and 14f is enlarged to ±8 K (relative to ±4 K of Figures 14a–14d).

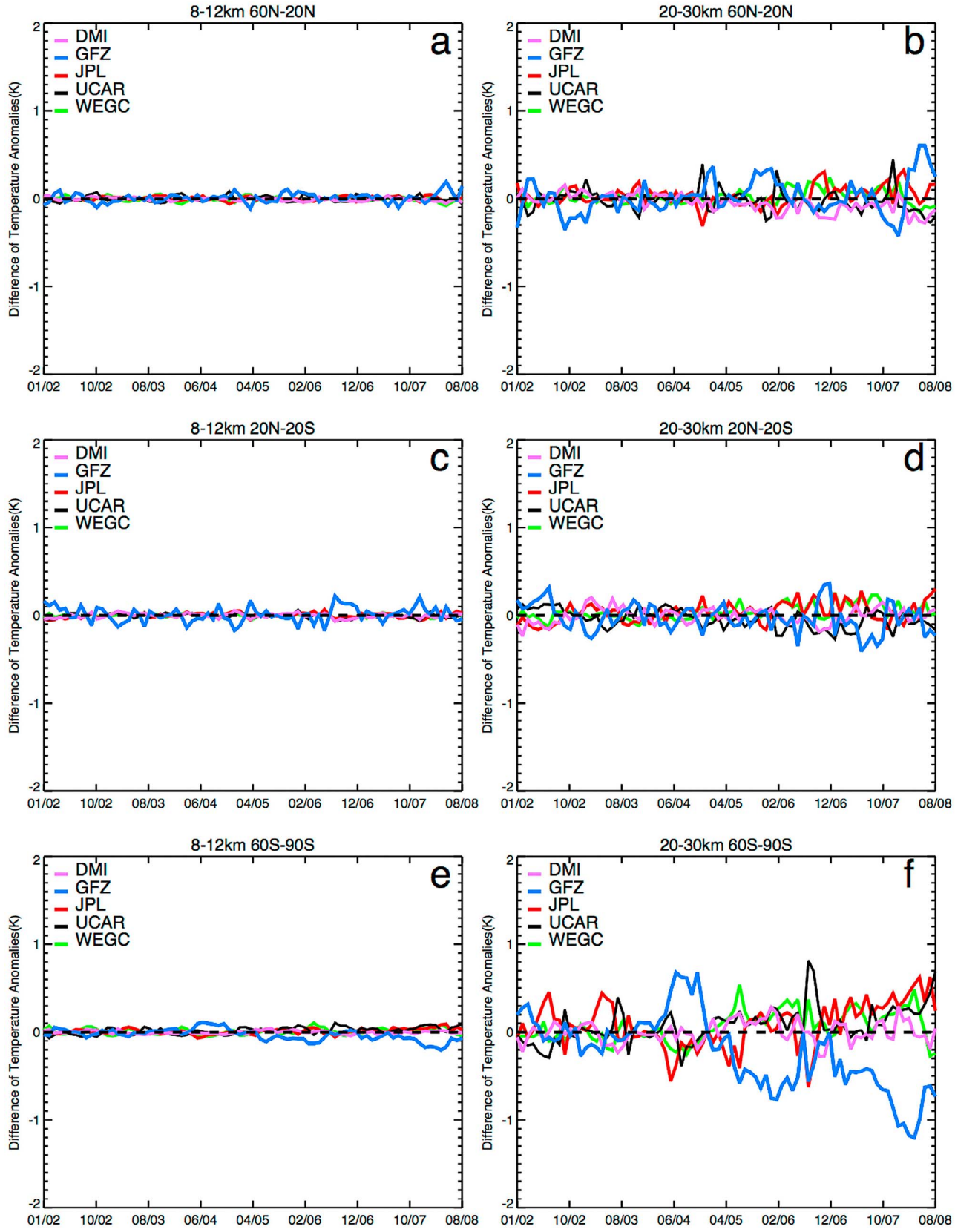

Figure 15. The differences of de-seasonalized temperature anomalies to the inter-center mean for DMI, GFZ, JPL, UCAR, and WEGC are shown for the 8 km to 12 km layer for (a) the 60°N to 20°N zone, (c) the 20°N to 20°S zone, and (e) the 60°S to 90°S zone, and for the 20 km to 30 km layer for (b) the 60°N to 20°N zone, (d) the 20°N to 20°S zone, and (f) the 60°S to 90°S zone.

[56] The global trend differences to the mean trends among centers for dry pressure and dry geopotential height in 8 km to 30 km layer are within ±0.02%/5 yrs (Table 5) and ±2.3 m/5 yrs (Table 7), respectively. Again, the largest trend differences to the mean trends are from GFZ at southern high-latitudes.

5. Discussions and Applications

5.1. Propagation of Structural Uncertainty From Bending Angle (α) to Temperature (T)

[57] We quantified structural uncertainties of RO data from the statistics of trend differences among centers based on PPCs of bending angle, refractivity, temperature, pressure, and geopotential height. Uncertainties are actually accumulating in derived variables due to propagation through the retrieval chain. We reiterate here that four centers (UCAR EUM, DMI, and WEGC) share the same excess phase and amplitude data whereas JPL, UCAR and GFZ derive these independently. Uncertainties in the derived variables reflect both an accumulation of uncertainty in the processing chain and uncertainties in the raw amplitudes and phases.

[58] Thus, when an individual center shows a larger mean anomaly in bending angle, it is likely the same center will also contain larger mean anomalies in the other derived variables. For example, the mean global differences for bending angles from January 2002 to August 2008 among six centers are within ±0.04% for the 8 km to 30 km layer, where the global mean bending angle difference for JPL ($\Delta\alpha_{\mathrm{JPL}}^{\mathrm{PPC}}$) is 0.04% and that for WEGC is −0.03% (Table 2). The 0.04% of $\Delta\alpha_{\mathrm{JPL}}^{\mathrm{PPC}}$ represents the combined effects from different implementations of RO excess phase processing, POD, ionospheric correction, and initialization of the bending angle for Abel inversion at different centers. The 0.04% upper bound of $\Delta\alpha_{\mathrm{JPL}}^{\mathrm{PPC}}$ then leads to an upper bound of ∼0.02%, −0.27 K, −0.11%, and −5.8 m in global mean differences of refractivity, dry temperature, dry pressure, and dry geopotential height, respectively. We note that JPL possessing the largest bending angle difference is consistent with the fact that the other centers share the use of climatology for bending angle initialization, whereas the JPL procedure is independent of such climatology. Further studies are needed to understand how the bending angle initialization affects absolute accuracy.

[59] Although the derived variables from bending angle to temperature and geopotential height are not traced to SI units, the high precision of the raw RO observables is preserved through the processing steps. Even for the accumulated structural uncertainties, the anomaly time series for the individual centers are in general persistent in time. Standard deviations of the difference time series during the CHAMP era from January 2002 to August 2008 of bending angle, refractivity, dry temperature, dry pressure, and dry geopotential height for all centers are within 0.02%, 0.01%, 0.06 K, 0.02%, and 2 m, respectively. These standard deviations for each variable quantify the structural uncertainty of RO-derived variables for climate monitoring.

5.2. Inter-center PPC for Monitoring RO Data Quality

[60] Although the PPC results cannot be used to indicate the accuracy of retrieved variables derived by individual centers, we have demonstrated that the inter-comparison method provides useful information as to how the anomalies of individual centers deviate from the inter-center mean. The behavior of anomaly time series, e.g., an offset change or a possible drift in the anomalies with time relative to the inter-center mean, is clearly identified. The PPC approach is a useful tool to monitor the quality of RO-derived variables in a processing chain and to identify processing-related inconsistencies among centers. We can detect impacts to the data of each inversion step, which is more challenging if only one center's data are used. Results of the inter-center comparisons also provide valuable feedback to the RO processing centers and help to further advance the processing chain development.

5.3. Causes of Structural Uncertainty in Retrieved Variables Due to Inversion Algorithms

[61] In the PPC, the structural uncertainty quantified varies depending on the different data sets used. Since the same orbital data, excess phase, and amplitude data are used, mean differences and MADs among DMI, UCAR, EUM and WEGC are in general smaller than those from JPL and GFZ. Although detailed processing implementations are largely different among centers, the anomalies of the retrieved products from bending angle to pressure and temperature are in general constant in time relative to the inter-center mean and show no obvious inter-annual variations.

[62] The 7-year trends derived from CHAMP RO data cannot be considered as climate trends. *Ho et al.* [2009a] used monthly mean climatologies with a different number of occultations for each center and thus had to quantify the sampling error. Residual sampling error related to sampling differences among centers was the dominant error source at high-latitude regions. The resulting structural uncertainty contained contributions from both retrieval error and residual sampling error, which was hard to quantify separately. Since sampling error does not exist in PPC studies using matched profile pairs, finer structural uncertainty information due to inversion procedures implemented by each center can be identified. The uncertainty of refractivity trends is within ±0.02%/5 yrs (−0.01% and 0.02%/5 yrs) from 2002 to 2008 in this study and consistent with the results of *Ho et al.* [2009a] of ±0.03%/5 yrs globally (−0.03% and 0.01%/5 yrs). In *Ho et al.* [2009a], the standard deviations of the time series of fractional refractivity differences for monthly mean climatologies for four centers (GFZ, JPL, UCAR, and WEGC) is about 0.02% after subtraction of the sampling errors. In this study it is less than 0.01% and the differences can be explained by the residual sampling errors in monthly mean climatologies used in *Ho et al.* [2009a].

[63] In a complementary study (A. K. Steiner et al., Quantification of structural uncertainty in climate data records from GPS radio occultation, submitted to *Atmospheric Chemistry and Physics*, 2012) the structural uncertainty of such monthly mean climatological fields is quantified for all six centers. In that study the sampling error is estimated based on the ERA (ECMWF re-analysis) Interim reanalysis [*Dee et al.*, 2011] and subtracted from the RO climatologies. Results show that trends for all RO-derived variables are consistent with the results of this PPC study in regions where background variation is not significant, which generally applies within 50°N to 50°S. The consistency of findings from the different

studies, which use different data versions and a different methodological approach, further underlines the quality of RO data and their utility for climate studies [*Ho et al.*, 2007, 2010; *Lackner et al.*, 2011; *Steiner et al.*, 2011].

6. Conclusions

[64] In this study we utilized CHAMP RO data processed by six RO processing centers to quantify structural uncertainty of RO-derived atmospheric variables and to examine their suitability for climate monitoring. While the fundamental phase delay observed from the GPS RO technique is synchronized to the ultra-stable atomic clocks on the ground, the derived RO variables (bending angle, refractivity, dry pressure, dry geopotential height, and dry temperature) are not. The retrieved results may vary when different processing algorithms and implementations are used. In this study, profile-to-profile CHAMP variables from January 2002 to August 2008 retrieved from common approaches but with different implementations at the centers are compared. Our analyses reach the following conclusions.

[65] 1. Although the PPC results cannot be used to indicate the accuracy of retrieved variables derived by individual centers, the mean differences and the standard deviations of each individual center relative to the inter-center mean determine the structural uncertainty among centers due to different implementations and assumptions used in the RO inversion procedures along the processing chain. Results show that different implementations in the inversion procedures do introduce small but stable retrieval differences among centers. In addition, when a center contains a large mean anomaly in bending angle, the same center is also likely to contain larger mean anomalies in the other derived variables in the inversion chain. For example, the 0.04% upper bound of mean global differences of bending angle from JPL in the 8 km to 30 km layer for 01/2002 to 08/2008 also leads to an upper bound of ~0.02%, −0.27 K, −0.11%, and −5.8 m in global mean differences of refractivity, dry temperature, dry pressure, and dry geopotential height, respectively. The mean global differences of bending angle, refractivity, dry temperature, dry pressure, and dry geopotential height in the 8 km to 30 km layer for 01/2002 to 08/2008 are between −0.03% and 0.04%, −0.01% and 0.02%, −0.27 K and 0.13 K, −0.11% and 0.07%, and −10 m and 10 m, respectively. The corresponding MAD in the same height range are within 0.74% for bending angle, 0.18% for refractivity, 0.92 K for temperature, 0.52% for pressure, and 30 m for geo-potential height, respectively.

[66] 2. Although the derived variables from bending angle to temperature and geopotential height are not readily traceable to SI units, the high precision nature of the raw RO observables is preserved in the inversion chain. The standard deviation of all variables is smallest at about 15 km altitude and grows exponentially to 30 km. The estimated standard deviations near 15 km vary slightly among centers and the mean standard deviation from all centers near 15 km for bending angle, refractivity, dry temperature, dry pressure, and dry geopotential height is within 0.5%, 0.1%, 0.3 K, 0.02%, and 10 m, respectively.

[67] 3. Uncertainties accumulate in derived variables due to propagation through the RO retrieval chain. This is reflected in the inter-center differences, which are small for bending angle and refractivity increasing to dry temperature, dry pressure, and dry geopotential height. Although there are small mean anomaly differences among centers, they are more or less constant in the time series comparisons. The mean anomaly differences of the time series in the 8 km to 30 km layer for bending angle, refractivity, dry temperature, dry pressure, and dry geopotential height for all centers are −0.08% to 0.12%, −0.03% to 0.02%, −0.27 K to 0.15 K, −0.04% to 0.04%, and −7.6 m to 6.8 m, respectively. The corresponding standard deviation is within 0.02%, 0.01%, 0.06 K, 0.02%, and 2.0 m, respectively.

[68] 4. With systematic inter-monthly time series anomalies among centers, the trend differences among centers are generally very small. The mean trend differences in the 8 km to 30 km layer for bending angle, refractivity, dry temperature, dry pressure, and dry geopotential height are within ±0.02%/5 yrs, ±0.02%/5 yrs, ±0.06 K/5 yrs, ±0.02%/5 yrs, and ±2.3 m/5 yrs, respectively. The largest uncertainties of inter-annual and intraseasonal anomalies stem from high-latitude regions in the 20 km to 30 km layer (mainly above 25 km) that are primarily due to different initialization methods used by the six centers. This encouraging consistency suggests that, once inter-center differences are better understood, RO can provide very accurate trend information.

[69] 5. Unlike atmospheric profiles retrieved from most satellite sounders, GPS RO-derived atmospheric profiles do not usually contain significant a priori information below 25 km. The PPC results demonstrate that the computed RO inter-center mean time series are very useful for monitoring the quality of RO data products from individual centers. The standard deviation of trends in anomaly time series provides important information on the structural uncertainty of RO-derived variables for climate monitoring. This provides unique applications of RO data for climate monitoring that is a strong advantage of RO.

[70] Besides CHAMP (2001 to 2008), several other international RO missions are also available and are processed by some of the above centers. These RO missions include GPS/Meteorology (GPS/MET, from 1995 to 1997), COSMIC (launched in April 2006), Gravity Recovery And Climate Experiment (GRACE, launched in 2004), Satélite de Aplicaciones Científicas-C (SAC-C, launched in 2000), MetOp/GRAS (launched in 2006), Communication/Navigation Outage Forecast System (C/NOFS, launched in 2008), and Terra Synthetic Aperture Radar (SAR) operating in the X-band (TerraSAR-X, launched in 2007). It has been shown that RO data from different satellites are highly consistent in terms of monthly mean climatologies [*Foelsche et al.*, 2009; *Steiner et al.*, 2011; *Foelsche et al.*, 2011] and PPCs [*Hajj et al.*, 2004; *Ho et al.*, 2009b] when applying the same processing scheme. Near future work is to further quantify the long-term structural uncertainties of the RO data from multiple RO missions that result from different processing methods to use RO-derived variables from multiple RO missions for climate monitoring.

Appendix A: Description of Processing Schemes at DMI, EUM, GFZ, JPL, UCAR, and WEGC

[71] Processing schemes used by DMI, EUM, GFZ, JPOL, UCAR and WEGC are summarized in this appendix. These processing steps include: i) POD and atmospheric excess

phase processing, ii) bending angle calculation, iii) ionospheric correction, iv) optimal estimation of the bending angles in the stratosphere, v) calculation of refractivity by Abel inversion, vi) calculation of pressure, temperature, and geopotential height, and vii) quality control (QC).

A1. Precise Orbit Determinations (POD) and Atmospheric Excess Phase Processing

[72] To generate the accurate atmospheric excess L1 and L2 phase, the effects of the relative motions and satellite clock fluctuations of the GPS and CHAMP satellites must be removed from the raw GPS L1 and L2 phase measurements. The dominant kinematic Doppler effect on the atmospheric excess phase is removed with knowledge of the satellite orbit positions and velocities obtained from POD processing. The CHAMP receiver clock fluctuations are removed by performing a single-difference between occultation link and clock reference link measurements [*Wickert et al.*, 2002; *Beyerle et al.*, 2005; *Schreiner et al.*, 2009]. The GPS satellite transmitter clock fluctuations can be removed with a double-difference procedure [*Hajj et al.*, 2002] using GPS measurements from a single ground receiver, or by applying clock offsets that have been previously estimated with data from a ground network of GPS receivers.

A1.1. DMI Procedure

[73] DMI obtained excess phase and amplitude data and CHAMP orbit data from UCAR CDAAC (version 2009.2650). These data are processed with the UCAR procedure described in section A1.5.

A1.2. EUM Procedure

[74] EUM also obtained excess phase and amplitude data and CHAMP orbit data from UCAR CDAAC (version 2009.2650).

A1.3. GFZ Procedure

[75] Precise orbits of the GPS and CHAMP satellites were generated by GFZ's POD software EPOS-OC (Earth Parameter and Orbit System – Orbit Computation) [*König et al.*, 2006]. The related orbit product (provided to the ISDC) used for the standard occultation processing is denoted as Rapid Science Orbit (RSO). Comparisons between CHAMP RSO data and satellite laser tracking measurements showed a mean deviation of 5.9 cm in error estimation of altitude [*Wickert et al.*, 2009]. A single-difference approach (occultation link to reference link) removing the LEO clock offsets is used to derive the L1 and L2 atmospheric excess phases. The GPS satellite clock errors are removed by interpolating the 5 min clock data provided with GFZ's GPS orbit products. To reduce the impact of the reference link L2 phase noise, GFZ uses a L1–L2 smoothing technique [*Beyerle et al.*, 2005].

A1.4. JPL Procedure

[76] JPL uses the reduced-dynamic strategy and the GIPSY (GPS-Inferred Positioning System) software package to determine the precise orbits of the GPS and CHAMP satellites [*Bertiger et al.*, 1994]. GPS satellite orbits and transmitter clock biases are based on the FLINN (Fiducial Laboratories for International Natural Science Network) solution generated at JPL using global ground tracking data [*Hajj et al.*, 2004]. The transmitter and receiver clocks are calibrated using the double-differencing technique [*Hajj et al.*, 2002].

A1.5. UCAR Procedure

[77] UCAR uses the Bernese software (v5.0) package to estimate precise orbits of the CHAMP satellite [*Dach et al.*, 2007]. Ionosphere-free phase observations from a 27-h period are used in a zero-difference reduced-dynamic filtering approach to estimate the position, velocity, and clock offset [*Švehla and Rothacher*, 2003]. Results of orbit overlaps for adjacent solutions show consistency in velocity at the 0.07 mm/s 3D root mean square (RMS), and orbit overlaps with other agencies show agreement at a level of 0.15 mm/s 3D RMS [*Schreiner et al.*, 2009]. The atmospheric excess phases for the L1 and L2 signals are computed using the single-difference processing strategy detailed in *Schreiner et al.* [2009]. The ionospheric correction of L1 and L2 on the non-occulting link is performed by smoothing L1–L2 to suppress the effect of LEO clock distribution errors and L2 noise of the CHAMP GPS receiver [*Schreiner et al.*, 2009].

A1.6. WEGC Procedure

[78] CHAMP RO excess phase data and orbit data provided by UCAR CDAAC (version 2009.2650) were used as input to the WEGC OPSv5.4 processing.

A2. Calculation of Bending Angles (α)

[79] A series of processing procedures is needed to convert the raw L1 and L2 excess phases into L1 and L2 bending angle profiles [*Vorob'ev and Krasil'nikova*, 1994; *Kursinski et al.*, 1997; *Rocken et al.*, 1997; *Hajj et al.*, 2002; *Kuo et al.*, 2004]. These steps include i) outlier rejection, noise filtering, and differentiation of excess phases to compute filtered Dopplers, which is necessary to eliminate multiple values of bending angle as a function of the impact parameter, ii) transferring the reference frame to the local center of the Earth's curvature to better satisfy the assumption of spherical symmetry, and iii) calculation of L1 and L2 bending angles from the filtered Doppler. As described in *Ho et al.* [2009a], above a height where atmospheric multipath is not significant (usually above the lower troposphere), one can derive L1 and L2 bending angles in the geometric optics approximation. In the lower troposphere, especially in moist environments where multipath propagation may be significant, wave optics techniques are usually applied to invert the L1 complex signal (phase and amplitude) to bending angle. Here we briefly describe the methods used by each center to calculate L1 and L2 bending angles. In this study, we focus our comparisons on the region from 8 km to 30 km, where atmospheric multipath effects are not significant.

A2.1. DMI Procedure

[80] Before processing into bending angle, the calibrated excess phases and amplitudes are corrected. This correction is partly mission-specific. For CHAMP data, the correction includes replacement of the observed L2 amplitudes by modeled amplitudes, and filtering of the noisy L2 excess phase and amplitude data using a radioholographic filtering technique [*Gorbunov et al.*, 2006]. Above 25 km altitude, a geometrical optics approach is used. For the differentiation of noisy phase excess, the measurement data are de-trended,

where the smooth trend can be differentiated analytically, and the noisy de-trended part of the signal is differentiated by applying the statistical optimization as described by *Ustinov* [1990]. Below 25 km, the CT2 (Canonical Transform of Type 2) wave optics method is applied to both L1 and L2 to obtain bending angles and impact parameters [*Gorbunov and Lauritsen*, 2004].

A2.2. EUM Procedure

[81] Atmospheric excess phase and orbit data as provided by the UCAR CDAAC archive were used as a starting point. Doppler profiles were calculated from excess phase data by applying a Savitzky-Golay smoothing filter (degree 4 over 70 points) [*Savitzky and Golay*, 1964]. Bending angle profiles are computed from Doppler shift profiles based on geometric optics [e.g., *Kursinski et al.*, 1997].

A2.3. GFZ Procedure

[82] A single value decomposition fit [*Press et al.*, 1996] is used for excess phase noise filtering and numerical differentiation to derive Doppler shift profiles. This filtering procedure applies a third order polynomial and encompasses 101 data samples of the 50 Hz data. Bending angle computation is based on geometric optics, below 15 km (smooth transition down to 11 km) the Full Spectrum Inversion (FSI) technique is applied to correct for multipath effects in the lower troposphere.

A2.4. JPL Procedure

[83] JPL uses different methods to compute bending angle for the L1 and L2 frequencies: the CT (Canonical Transform) technique and the non-CT technique. The CT technique is applied to the received phase and amplitude data for the L1 frequency, which is often available down to the surface. A non-CT version of L1 bending angles is also calculated in the same fashion as the L2 bending angles (non-CT) for use in the ionospheric correction.

A2.5. UCAR Procedure

[84] L1 and L2 bending angles are calculated in a reference frame centered at the local center of sphericity of the reference ellipsoid [*Syndergaard*, 1999] in the direction of the occultation plane at the estimated "occultation point" that corresponds to the estimated tangent point of the ray GPS-LEO, where the excess phase is equal to 500 m (3–4 km above the surface). In order to truncate the part of RO signal affected by tracking errors, the smoothed L1 excess Doppler is differenced with the Doppler model calculated based on GPS and LEO orbits and "wet" refractivity climatology [*Kirchengast et al.*, 1999]. The earliest time when the difference exceeds 10 Hz is found and then the signal is truncated at an earlier time when the difference reduces to 5 Hz. The bending angles are calculated differently above and below the so-called "transition height" which is determined dynamically for each occultation based on the following criteria: either the deviation of raw from smoothed L2 Doppler exceeds 6 Hz, or the difference between smoothed L2 and L1 (multiplied by the ratio of L2 to L1 frequencies) Dopplers exceeds 1 Hz. These criteria are checked below 40 km. Above the transition height the L1 and L2 bending angles are calculated in the approximation of geometric optics [*Vorob'ev and Krasil'nikova*, 1994; *Kursinski et al.*, 1997] after smoothing L1 and L2 excess phases with 3-pass sliding window polynomial regression of 3rd order. The L1 excess phase is smoothed with an equivalent window width of about 1 km. Additionally, for the ionospheric correction, both L1 and L2 bending angles are calculated after smoothing the excess phases with a different window (explained in section A3.5). Below the transition height, L1 bending angle is calculated by the FSI [*Jensen et al.*, 2003] from raw complex RO signal without smoothing. The FSI-retrieved bending angle is smoothed by the same filter as excess phase (see above) but with an equivalent window of about 0.15 km and truncated based on least squares fit of the step-function to the raw FSI-transformed amplitude.

A2.6. WEGC Procedure

[85] In the OPSv5.4, first an outlier rejection is performed on the L1 and L2 excess phase profiles at 50 Hz sampling rate. Data points outside three times the standard deviation are substituted by the interval's mean of a one-second running window. The excess phase profiles are smoothed by a regularization method after *Syndergaard* [1998] and then converted via numerical differentiation to Doppler shift profiles. Bending angle profiles are computed from Doppler shift profiles based on geometric optics [e.g., *Kursinski et al.*, 1997].

A3. Ionospheric Correction

[86] All centers apply ionospheric correction by forming a linear combination of L1 and L2 bending angles at a common impact parameter, generally following the approach by *Vorob'ev and Krasil'nikova* [1994] with some differences in implementations discussed below.

A3.1. DMI Procedure

[87] DMI uses Optimal Linear Combination (OLC), an algorithm devised by *Gorbunov* [2002]. The ionospheric correction, upper level noise reduction, and provision of an upper limit to the Abel integral are obtained within a single framework based on a statistically optimal combination of observed and modeled bending angles.

A3.2. EUM Procedure

[88] For lower tropospheric data, where only L1 bending angles are available, the following processing is used: (1) a linear fit in L1–L2 is performed for the lowest few kilometers where both bending angles are available; (2) the linear fit is then extrapolated down to the lowest altitude where L1 bending angles are available.

A3.3. GFZ Procedure

[89] The FSI technique (applied below 15 km) uses the ionosphere-free linear combination of L1 and L2. Here L1–L2 is linearly extrapolated downward from higher altitudes to continue the ionospheric correction down to the Earth's surface. The extrapolation is based on the longest available interval of connected data samples (minimum of 650 requested) for which the quotient of the L1 and L2 excess phase forward differences lies within the range between 0.97 and 1.03 [see *Beyerle et al.*, 2004].

A3.4. JPL Procedure

[90] At altitudes below approximately 10 km (based on a minimum signal-to-noise ratio (SNR) criterion applied to

the L2 data), ionospheric L1–L2 is linearly extrapolated downward from higher altitudes to continue the ionospheric correction to the surface.

A3.5. UCAR Procedure

[91] Above the transition height, the L1 bending angle, obtained with an approximate 1 km smoothing window (see section A2.5), is corrected by L4 = L1–L2 bending angle obtained with a different smoothing window. The latter window, defined in the range of approximately 1 km to 4 km, is determined individually for each occultation by minimizing fluctuation of the L3 (ionosphere-free) bending angle between 60 km and 80 km [*Sokolovskiy et al.*, 2009]. This reduces the combined effect of L2 noise and the small-scale ionospheric residuals. Below the transition height, the FSI-retrieved L1 bending angle is corrected by a constant obtained by a least squares fit of L4 bending angle in the 3 s interval immediately above the transition height.

A3.6. WEGC Procedure

[92] Below 15 km impact height, the ionospheric correction is linearly extrapolated downward from higher altitudes (i.e., the L1–L2 bending angle difference profile is linearly fitted at 15 km to 25 km and extended downward) to continue the ionospheric correction as deep as needed into the troposphere. This latter measure ensures that the resulting neutral atmospheric bending angle profile is independent of the L2 data quality in the troposphere, which is frequently degraded due to lower signal-to-noise ratio of L2 data compared to L1 data [e.g., *Steiner et al.*, 1999].

A4. Initialization of the Bending Angle (α) for Abel Inversion

[93] This section summarizes the methods used by each center for optimal estimation of the bending angle for Abel inversion.

A4.1. DMI Procedure

[94] The OLC of L1 and L2 bending angles includes the merging of the observations at high altitudes with a model profile in a statistically optimized solution [*Gorbunov*, 2002]. The model profile used in this process is found through a global search [*Gobiet and Kirchengast*, 2004] (every 10 degrees latitude, every 20 degrees longitude, for monthly mean profiles) for bending angles constructed from the MSISE-90 (Mass Spectrometer Incoherent Scatter Radar extended model 1990) climatological model [*Hedin*, 1991]. The logarithm of the model bending angles are scaled and shifted in a least squares fit to the observed bending angle above 40 km, and the profile requiring the least scaling and shifting is chosen as described in *Lauritsen et al.* [2011]. In the OLC, the L1 and L2 bending angle observation errors and a priori ionospheric bending are estimated as described by *Gorbunov* [2002], whereas the error of the model profile is set to a fixed value. Correlations between errors in the vertical are neglected. Above 100 km, the bending angle is assumed to decrease exponentially with altitude, allowing an approximate analytical solution of the Abel integral to infinity [e.g., *Gorbunov et al.*, 2011].

A4.2. GFZ Procedure

[95] The algorithm described by *Sokolovskiy and Hunt* [1996] is applied for the bending angle optimization. The background model is based on the MSISE-90 climatology. The observation error variance is estimated from observation-background deviation between 60 km and 70 km. To reduce influence from the background model in the weighting procedure, the observation error is divided by 4. Below 40 km altitude, no bending angle optimization is applied. Above 100 km, optimized bending angles are replaced by the pure climatology. The Abel inversion of the optimized bending angle profiles starts at 150 km.

A4.3. JPL Procedure

[96] As described in *Ho et al.* [2009a], the JPL approach is to assume that the bending angle decays exponentially with height at high altitudes. Bending angle measurements within 40 km and 50 km altitudes are fit to a simple exponential function. Bending angles above 50 km are extrapolated upward from the fitted exponential function.

A4.4. UCAR Procedure

[97] In order to reduce the effect of error propagation in the refractivity retrieved by Abel inversion, the observational ionosphere-free bending angle is optimally combined with a fitted background bending angle model by applying dynamic error estimation and neglecting vertical error correlations [*Sokolovskiy and Hunt*, 1996; *Lohmann*, 2005]. The background bending angle model is calculated from National Center for Atmospheric Research (NCAR) climatology with exponentially extrapolated density above the top height (approx. 90 km). The fitted background model is obtained by log linear least squares fit of the background model to observations between 20 km and a maximum height (<60 km, estimated individually for each occultation). Above 60 km, the fitted background model smoothly transitions to the background model. The weighting functions in this optimal linear combination depend on the observational and background errors estimated individually for each occultation. The observational error variance is estimated from the difference between the observation and the background between 60 km and 80 km. The background error variance is estimated from the difference between the observation and the fitted background between 20 km and the maximum height. The optimized bending angle is subject to Abel inversion below 150 km.

A4.5. WEGC Procedure

[98] Above 30 km impact height the retrieved bending angle profiles are combined with background information derived from ECMWF (European Centre for Medium-Range Weather Forecasts) short-range forecast fields (24 h to 30 h forecasts), which are extended with MSISE-90 data up to 120 km. Statistical optimization is performed with inverse covariance weighting [*Healy*, 2001; *Rieder and Kirchengast*, 2001; *Gobiet and Kirchengast*, 2004]. The error of the background profile is assumed to amount to 15% of the background bending angle with a vertical error correlation length of 10 km. The observation error is estimated from the variance of the observed profile between 65 km and 80 km

(generally amounting to 3 μrad to 4 μrad for CHAMP data at ~2 km vertical resolution), with a vertical error correlation length of 2 km assumed. The retrieval-to-background error ratio indicates that the atmospheric profiles are background-dominated above the stratopause and observation dominated below about 40 km [*Gobiet and Kirchengast*, 2004; *Gobiet et al.*, 2007; *Pirscher*, 2010].

A5. Derivation of Refractivity (N), Dry Pressure (p), and Dry Temperature (T)

[99] Similar approaches are used by all centers to derive dry pressure and dry temperature from refractivity obtained by Abel inversion.

A5.1. DMI Procedure

[100] The dry pressure and dry temperature profiles are obtained by assuming a completely dry atmosphere, consisting of an ideal gas in hydrostatic equilibrium, with the gravitational acceleration g given as a specific function of latitude and altitude. The refractivity profile is extended up to the height of 150 km using the model profile after the global search and fitting procedure as described above in section A4.1. The hydrostatic equation is vertically integrated downward from 150 km, with the top boundary conditions determined from the refractivity and its gradient at the top of the profile. In each integration step, the dry pressure is first calculated from hydrostatic equilibrium and the dry temperature is then calculated from the dry pressure and the observed refractivity.

A5.2. GFZ Procedure

[101] GFZ uses the standard dry temperature/pressure retrieval: Assuming dry air conditions, refractivity is directly proportional to air density (applying ideal gas equation). The pressure profile is derived by downward integration of the density profile assuming hydrostatic equilibrium. Pressure retrieval is initialized at 100 km with MSISE-90. The temperature profile is calculated consecutively applying the Smith-Weintraub formula [*Smith and Weintraub*, 1953].

A5.3. JPL Procedure

[102] Using the dry refractivity equation ($N = a_1\, p/T$, where $a_1 = 77.6$ K/hPa), the dry temperature (or pressure) is obtained by integrating the hydrostatic equation downward assuming known temperature value at height z_m. For this integration, density is derived from the measured refractivity and the ideal gas law. The interpolated ECMWF temperature is used at z_m = 40 km. The gravitational acceleration is computed based on equation 5–50 from *Turcotte and Schubert* [1982].

A5.4. UCAR Procedure

[103] Refractivity is retrieved by Abel inversion as a function of refractional radius. The refractional radius is converted to radius, then to the height above the reference ellipsoid (by subtracting the local radius of curvature), then to the height above mean sea level (MSL) (by subtracting the JGM2 (Joint Gravity Model-2) geoid undulation at the occultation point). The dry density is derived from refractivity under the assumption of dry air by using the equation for refractivity [*Smith and Weintraub*, 1953] and the equation of state of dry air. Dry pressure is retrieved from dry density by integration of the hydrostatic equation. The gravitational acceleration is a function of height over the reference ellipsoid and latitude (3-term expansion) [*Lambeck*, 1988]. Dry temperature is calculated from the retrieved dry density and pressure by use of the equation of state of dry air.

A5.5. WEGC Procedure

[104] The Abel inversion, implemented as a numerical integration, is applied to the optimized bending angle profile starting at 120 km and yields the refractivity profile. The refractivity profile is finally smoothed by a Blackman window filter (<1 km width, moving average), providing filtering of potential residual numerical noise while conserving the basic Fresnel-scale resolution of the data (~1 km resolution).

[105] The subsequent atmospheric profile retrieval is a dry air retrieval (for a detailed discussion of dry versus actual atmospheric parameters see *Scherllin-Pirscher et al.* [2011a]). The latitude- and height-dependent acceleration of gravity is used in the hydrostatic equation. Here the upper bound of the integral, z_{top}, is set to 120 km (the upper bound of the refractivity profile), since contributions from beyond have been shown to be negligible for the results of interest below the stratopause [*Steiner et al.*, 1999]. Dry temperature is obtained by utilizing the equation of state. The dry temperature profile is finally smoothed by a Blackman window filter in the same way as refractivity, for filtering of potential residual numerical noise.

A6. Derivation of Geopotential Height (Z)

A6.1. DMI Procedure

[106] The geometric height above the World Geodetic System-84 (WGS-84) reference ellipsoid is converted to MSL altitude by subtracting the geoid undulation, obtained from a spectral description of the EGM-96 (Earth Gravitational Model 1996) geoid of order and degree 360 (National Imagery and Mapping Agency - NIMA). The spectral coefficients are expanded as Legendre polynomials and applied to the nominal latitude and longitude of the occultation. The altitude is then converted to a geopotential height through an expression derived from the Somigliana equation, which gives the gravity as a function of latitude and altitude. The resulting profiles of dry pressures as a function of geopotential heights can be interpolated to give the geopotential heights of (dry) isobaric surfaces.

A6.2. GFZ Procedure

[107] Geopotential height is derived by upward integration of the local altitude dependent gravitational acceleration (g). Integration step size is 200 m. The gravitational acceleration at local geoid surface (g_{surf}) is derived from the EGM-96 geoid model. Altitude dependence follows $g(i) = g_{surf}*(r/(r + h(i)))^2$ where r is the local geoid radius and h is altitude above geoid surface.

A6.3. JPL Procedure

[108] The geometric height is converted to geopotential height as described in *Leroy* [1997, equation 1]. The gravity model JGM-3 (Joint Gravity Model-3) is used to convert an altitude z to a potential energy U. The potential energy is then converted to geopotential height by subtracting a constant corresponding to the potential energy of MSL and dividing

this difference by a standard gravitational acceleration g = 9.80665 m/s^2. The JGM-3 gravity model is truncated at a maximum spherical harmonic degree of 36.

A6.4. UCAR Procedure

[109] Dry pressure (discussed in section A5.4) is computed as a function of geometric height and, additionally, as a function of geopotential height (the integral of gravity acceleration normed by the gravity acceleration at the surface). Then the inverse function provides the geopotential height of a given pressure.

A6.5. WEGC Procedure

[110] Geopotential height Z is computed by first integrating the acceleration of gravity over the RO-derived altitude z, divided by the standard acceleration of gravity at sea level (g_0 = 9.80665 m s^{-1}). Geopotential heights $Z(z)$ are then linearly interpolated to a standard "pressure altitude" grid z_p (equivalent to a pressure level grid but a convenient altitude-type scale), defined by $z_p = -H_0 \cdot \ln(p/p_0)$, where H_0 = 7 km is a standard atmospheric scale height, p_0 = 1013.25 hPa is the standard surface pressure, and p is the atmospheric pressure provided here by the dry pressure profile $p_{dry}(z)$. The interpolation result is $Z_{dry}(z_p)$, the desired dry geopotential height profile at the pressure altitude grid associated with the dry pressure level grid $p_{dry}(z_p) = p_0 \cdot \exp(z_p/H_0)$.

A7. Quality Control (QC) Methods

A7.1. DMI Procedure

[111] The processing from raw data to bending angle and refractivity profiles implicitly and explicitly includes several quality screening steps in which data may be totally or partly rejected [*Gorbunov et al.*, 2006, 2011]. These quality checks address different aspects of noise and multipath effects. The final refractivity profiles are compared to collocated ECMWF analysis profiles and the whole profile is discarded if any point in the profile deviates by more than 10% from the ECMWF value somewhere in the altitude range 10 km to 35 km.

A7.2. EUM Procedure

[112] No specific quality control procedure is performed in generating the bending angle profiles.

A7.3. GFZ Procedure

[113] Occultation events shorter than 20 s are generally not processed. A minimum of 650 connected data samples are requested for which the quotient of the L1 and L2 excess phase forward differences has to be in the range between 0.97 and 1.03 [see *Beyerle et al.*, 2004]. This criterion, applied for L1–L2 extrapolation in the troposphere, excludes occultations with early loss of L2 tracking mainly due to ionospheric disturbances. The fractional refractivity deviation from MSISE-90 is requested to be less than 22.5% in the altitude range between 8 km and 31 km. If this criterion is violated at any point within this altitude range, the profile is rejected.

A7.4. JPL Procedure

[114] For each occultation, upper altitude data are removed where the ionosphere-corrected bending angle has the wrong sign or where the bending angle deviates significantly from an exponential fit ($\chi^2 > 0.02$). This typically occurs between 60 and 80 km. Post-retrieval QC is then applied based on comparison with ECMWF with the following criteria: (i) $|N - N(ECMWF)| < 0.1\ N(ECMWF)$ over the whole profile below 30 km and (ii) $|T - T(ECMWF)| < 10$ K between ~8 km to 30 km. The QC criteria are less strict than the previous data set from *Ho et al.* [2009a] where the criteria were applied up to 40 km, which resulted in the elimination of many high-latitude profiles [*Ho et al.*, 2009a].

A7.5. UCAR Procedure

[115] Data affected by receiver tracking errors are truncated based on deviation of the smoothed L1 Doppler from the model based on orbits and refractivity climatology (see section A2.5). The whole occultation is discarded if (i) the transition height (see section A2.5) is larger than 20 km; (ii) the maximum height used for fitting of the background profile (defined in section A4.4) is less than 40 km; (iii) the retrieved refractivity differs fractionally from background by more than 50% between 10 km and 40 km; (iv) the standard deviation of the ionosphere-free bending angle from background between 60 km and 80 km is larger than 1.5E–4 rad and/or mean deviation is larger than 1E–4 rad.

A7.6. WEGC Procedure

[116] The OPS QC includes internal (early stage) and external (final stage) QC. Internal QC is applied down to bending angle level and probes technical and consistency parts of the data and adjusts error estimates or rejects profiles during the retrieval as found needed [*Pirscher*, 2010]. The external QC compares retrieved refractivity results to collocated ECMWF analysis profiles. Profiles featuring a relative refractivity difference to the ECWMF profiles >10% at any altitude level between 5 km and 35 km, and/or a temperature difference >20 K between 8 km and 25 km, are rejected. In total the QC removes about 35% of the CHAMP RO profiles entering the retrieval at excess phase level.

Notation

α	Bending Angle.
AMSU	Advanced Microwave Sounding Units.
BA	Bending Angle.
CDR	Climate Data Record.
CHAMP	CHAllenging Minisatellite Payload.
CDAAC	COSMIC Data Analysis and Archive Center.
COSMIC	Constellation Observing System for Meteorology, Ionosphere, and Climate.
C/NOFS	Communication/Navigation Outage Forecast System.
CT	Canonical Transform.
CT2	Canonical Transform of Type 2.
DMI	Danish Meteorological Institute.
ECMWF	European Centre for Medium-Range Weather Forecasts.
EGM-96	Earth Gravitational Model 1996.
EPOS-OC	Earth Parameter and Orbit System – Orbit Computation.
ERA	ECMWF re-analysis.
EUMETSAT	European Organisation for the Exploitation of Meteorological Satellites.

EUM European Organisation for the Exploitation of Meteorological Satellites.
FLINN Fiducial Laboratories for International Natural Science Network.
FP7 Seventh Framework Programme for Research and Technological Development of the European Commission.
FSI Full Spectrum Inversion.
FWF Austrian Science Fund.
g gravitational acceleration.
g_0 standard acceleration of gravity at sea level.
g_{surf} gravitational acceleration at local geoid surface.
GFZ German Research Centre for Geosciences.
GIPSY GPS-Inferred Positioning System.
GPS Global Positioning System.
GPS/MET GPS/Meteorology.
GRACE Gravity Recovery And Climate Experiment.
GRAS Global Navigation Satellite System RO Receiver for Atmospheric Sounding.
h altitude above geoid surface.
H_0 a standard atmospheric scale height.
ISDC Information System and Data Center.
JGM-2 Joint Gravity Model-2.
JGM-3 Joint Gravity Model-3.
JPL Jet Propulsion Laboratory.
L1 GPS L-band frequency in 1575.42 MHz.
L2 GPS L-band frequency in 1227.6 MHz.
LEO low earth orbit.
LS lower stratosphere.
MAD median absolute deviation.
MPC mean profile-to-profile climatology.
MSL mean sea level.
MSIS Mass Spectrometer Incoherent Scatter Radar Model.
MSISE-90 Mass Spectrometer Incoherent Scatter Radar Extended Model 1990.
MSU Microwave Sounding Units.
N refractivity.
NCEP National Centers for Environmental Prediction.
NIMA National Imagery and Mapping Agency.
NCAR National Center for Atmospheric Research.
OLC Optimal Linear Combination.
OPS Occultation Processing System.
p pressure.
p_0 standard surface pressure.
POD precise orbit determination.
PPC profile-to-profile comparison.
QC quality control.
r local geoid radius.
RMS root mean square.
RO radio occultation.
ROM Radio Occultation Meteorology.
RSO Rapid Science Orbit.
SAC-C Satélite de Aplicaciones Científicas-C.
SAF Satellite Application Facility.
SAR Synthetic Aperture Radar.
SI System of Units.
SNR signal-to-noise ratio.
T temperature.
TerraSAR-X Terra SAR operating in the X-band.
TOVS TIROS Operational Vertical Sounders.
TS highest troposphere/lowest stratosphere.
U potential energy.
UT upper troposphere.
UCAR University Corporation for Atmospheric Research.
WEGC Wegener Center/University of Graz.
WGS-84 World Geodetic System-84.
Z geopotential height.

[117] **Acknowledgments.** We thank all the scientists, engineers and technicians of the CHAMP satellite mission for their successful work, which is the basis for our investigations. The DMI work was supported by the Radio Occultation Meteorology (formerly GRAS) Satellite Application Facility, which is an operational RO processing center under EUMETSAT. DMI thanks K. R. Larsen for assistance in the processing of data. The work of EUM was partially funded by the ERA-CLIM project, under the Seventh Framework Programme for Research and Technological Development of the European Commission (FP7). The work of GFZ was supported by GEOTECHNOLOGIEN grant 03G0728A. The work of JPL, California Institute of Technology, was carried out under a contract with the National Aeronautics and Space Administration. The work of UCAR was supported by the National Science Foundation under cooperative agreement AGS-0918398/CSA AGS-0939962. The National Center for Atmospheric Research is sponsored by the National Science Foundation. Shu-peng Ho acknowledges NOAA support under grant NA07OAR4310224. The work of WEGC was funded by the Austrian Science Fund (FWF) grants P21642-N21 and P22293-N21 and partially by European Space Agency and FFG-ALR Austria contracts.

References

Bertiger, W. I., et al. (1994), GPS precise tracking of TOPEX/Poseidon: Results and implications, *J. Geophys. Res.*, *99*, 24,449–24,464, doi:10.1029/94JC01171.

Beyerle, G., J. Wickert, T. Schmidt, and C. Reigber (2004), Atmospheric sounding by GNSS radio occultation: An analysis of the negative refractivity bias using CHAMP observations, *J. Geophys. Res.*, *109*, D01106, doi:10.1029/2003JD003922.

Beyerle, G., T. Schmidt, J. Wickert, and C. Reigber (2005), GPS radio occultation with GRACE: Atmospheric profiling utilizing the zero difference technique, *Geophys. Res. Lett.*, *32*, L13806, doi:10.1029/2005GL023109.

Borsche, M. (2008), Global atmospheric climatologies from radio occultation data and derivation of diagnostic parameters for climate monitoring, *Sci. Rep., 22-2008*, Wegener Cent., Graz, Austria.

Borsche, M., A. Gobiet, A. K. Steiner, U. Foelsche, G. Kirchengast, T. Schmidt, and J. Wickert (2006), Pre-operational retrieval of radio occultation based climatologies, in *Atmosphere and Climate: Studies by Occultation Methods*, edited by U. Foelsche, G. Kirchengast, and A. K. Steiner, pp. 315–323, Springer, Berlin, doi:10.1007/3-540-34121-8_26.

Christy, J. R., R. W. Spencer, and W. D. Braswell (2000), MSU Tropospheric temperatures: Data set construction and radiosonde comparisons, *J. Atmos. Oceanic Technol.*, *17*, 1153–1170, doi:10.1175/1520-0426(2000)017<1153:MTTDCA>2.0.CO;2.

Dach, R., U. Hugentobler, P. Fridez, and M. Meindl (Eds.) (2007), Bernese GPS software version 5.0, user manual, Astron. Inst., Univ. of Bern, Bern.

Dee, D. P., et al. (2011), The ERA-Interim reanalysis: Configuration and performance of the data assimilation system, *Q. J. R. Meteorol. Soc.*, *137*, 553–597, doi:10.1002/qj.828.

Fjeldbo, G. F., V. R. Eshleman, and A. J. Kliore (1971), The neutral atmosphere of Venus as studied with the Mariner V radio occultation experiments, *Astron. J.*, *76*, 123–140, doi:10.1086/111096.

Foelsche, U., G. Kirchengast, A. K. Steiner, L. Kornblueh, E. Manzini, and L. Bengtsson (2008a), An observing system simulation experiment for climate monitoring with GNSS radio occultation data: Setup and test bed study, *J. Geophys. Res.*, *113*, D11108, doi:10.1029/2007JD009231.

Foelsche, U., M. Borsche, A. K. Steiner, A. Gobiet, B. Pirscher, and G. Kirchengast (2008b), Observing upper troposphere-lower stratosphere climate with radio occultation data from the CHAMP satellite, *Clim. Dyn.*, *31*, 49–65, doi:10.1007/s00382-007-0337-7.

Foelsche, U., B. Pirscher, M. Borsche, G. Kirchengast, and J. Wickert (2009), Assessing the climate monitoring utility of radio occultation data: From CHAMP to FORMOSAT-3/COSMIC, *Terr. Atmos. Oceanic Sci.*, *20*, 155–170, doi:10.3319/TAO.2008.01.14.01(F3C).

Foelsche, U., B. Scherllin-Pirscher, F. Ladstädter, A. K. Steiner, and G. Kirchengast (2011), Refractivity and temperature climate records from multiple radio occultation satellites consistent within 0.05%, *Atmos. Meas. Tech.*, *4*, 2007–2018, doi:10.5194/amt-4-2007-2011.

Free, M., D. J. Seidel, J. K. Angell, J. Lanzante, I. Durre, and T. C. Peterson (2005), Radiosonde Atmospheric Temperature Products for Assessing Climate (RATPAC): A new data set of large-area anomaly time series, *J. Geophys. Res.*, *110*, D22101, doi:10.1029/2005JD006169.

Gobiet, A., and G. Kirchengast (2004), Advancements of GNSS radio occultation retrieval in the upper stratosphere for optimal climate monitoring utility, *J. Geophys. Res.*, *109*, D24110, doi:10.1029/2004JD005117.

Gobiet, A., G. Kirchengast, J. Wickert, C. Retscher, D.-Y. Wang, and A. Hauchecorne (2005), Evaluation of stratospheric radio occultation retrieval using data from CHAMP, MIPAS, GOMOS and ECMWF analysis field, in *Earth Observation With CHAMP: Results From Three Years in Orbit*, edited by C. Reigber et al., pp. 531–536, Springer, Berlin, doi:10.1007/3-540-26800-6_84.

Gobiet, A., G. Kirchengast, L. Manney, M. Borsche, C. Retscher, and G. Stiller (2007), Retrieval of temperature profiles from CHAMP for climate monitoring: Intercomparison with Envisat MIPAS and GOMOS and different atmospheric analyses, *Atmos. Chem. Phys.*, *7*(13), 3519–3536, doi:10.5194/acp-7-3519-2007.

Goody, R., J. Anderson, and G. North (1998), Testing climate models: An approach, *Bull. Am. Meteorol. Soc.*, *79*(11), 2541–2549, doi:10.1175/1520-0477(1998)079<2541:TCMAA>2.0.CO;2.

Goody, R., J. Anderson, T. Karl, R. B. Miller, G. North, J. Simpson, G. Stephens, and W. Washington (2002), Why monitor the climate?, *Bull. Am. Meteorol. Soc.*, *83*(6), 873–878, doi:10.1175/1520-0477(2002)083<0873:WWSMTC>2.3.CO;2.

Gorbunov, M. E. (2002), Ionospheric correction and statistical optimization of radio occultation data, *Radio Sci.*, *37*(5), 1084, doi:10.1029/2000RS002370.

Gorbunov, M. E., and K. B. Lauritsen (2004), Analysis of wave fields by Fourier integral operators and their application for radio occultations, *Radio Sci.*, *39*, RS4010, doi:10.1029/2003RS002971.

Gorbunov, M. E., K. B. Lauritsen, A. Rhodin, M. Tomassini, and L. Kornblueh (2006), Radio holographic filtering, error estimation, and quality control of radio occultation data, *J. Geophys. Res.*, *111*, D10105, doi:10.1029/2005JD006427.

Gorbunov, M. E., V. Shmakov, S. S. Leroy, and K. B. Lauritsen (2011), COSMIC radio occultation processing: Cross-center comparison and validation, *J. Atmos. Oceanic Technol.*, *28*, 737–751, doi:10.1175/2011JTECHA1489.1.

Grody, N. C., K. Y. Vinnikov, M. D. Goldberg, J. Sullivan, and J. D. Tarpley (2004), Calibration of Multi-satellites observations for climate studies, Microwave Sounding Unit (MSU), *J. Geophys. Res.*, *109*, D24104, doi:10.1029/2004JD005079.

Haimberger, L., C. Tavolato, and S. Sperka (2008), Towards elimination of the warm bias in historic radiosonde temperature records: Some new results from a comprehensive intercomparison of upper air data, *J. Clim.*, *21*, 4587–4606, doi:10.1175/2008JCLI1929.1.

Hajj, G. A., E. R. Kursinski, L. J. Romans, W. I. Bertiger, and S. S. Leroy (2002), A technical description of atmospheric sounding by GPS occultation, *J. Atmos. Sol. Terr. Phys.*, *64*(4), 451–469, doi:10.1016/S1364-6826(01)00114-6.

Hajj, G. A., C. O. Ao, B. A. Iijima, D. Kuang, E. R. Kursinski, A. J. Mannucci, T. K. Meehan, L. J. Romans, M. de la Torre Juarez, and T. P. Yunck (2004), CHAMP and SAC-C atmospheric occultation results and intercomparisons, *J. Geophys. Res.*, *109*, D06109, doi:10.1029/2003JD003909.

Hardy, K. R., G. A. Hajj, and E. R. Kursinski (1994), Accuracies of atmospheric profiles obtained from GPS occultations, *Int. J. Satell. Commun. Networking*, *12*, 463–473, doi:10.1002/sat.4600120508.

Healy, S. B. (2001), Smoothing radio occultation bending angles above 40 km, *Ann. Geophys.*, *19*, 459–468, doi:10.5194/angeo-19-459-2001.

Hedin, A. E. (1991), Extension of the MSIS thermosphere model into the middle and lower atmosphere, *J. Geophys. Res.*, *96*, 1159–1172, doi:10.1029/90JA02125.

Ho, S.-P., Y. H. Kuo, Z. Zeng, and T. Peterson (2007), A comparison of lower stratosphere temperature from microwave measurements with CHAMP GPS RO data, *Geophys. Res. Lett.*, *34*, L15701, doi:10.1029/2007GL030202.

Ho, S.-P., et al. (2009a), Estimating the uncertainty of using GPS RO data for climate monitoring: Inter-comparison of CHAMP refractivity climate records 2002–2006 from different data centers, *J. Geophys. Res.*, *114*, D23107, doi:10.1029/2009JD011969.

Ho, S.-P., W. He, and Y.-H. Kuo (2009b), Construction of consistent temperature records in the lower stratosphere using Global Positioning System radio occultation data and microwave sounding measurements, in *New Horizons in Occultation Research*, edited by A. K. Steiner et al., pp. 207–217, Springer, Berlin.

Ho, S.-P., Y.-H. Kuo, W. Schreiner, and X. Zhou (2010), Using SI-traceable Global Positioning System radio occultation measurements for climate monitoring, *Bull. Am. Meteorol. Soc.*, *91*(7), S36–S37.

Intergovernmental Panel on Climate Change (IPCC) (2007), *Climate Change: The Physical Science Basis. Contribution of Working Group I to the Fourth Assessment Report of the Intergovernmental Panel on Climate Change*, edited by S. Solomon et al., 996 pp., Cambridge Univ. Press, Cambridge, U. K.

Jensen, A. S., M. Lohmann, H.-H. Benzon, and A. Nielsen (2003), Full spectrum inversion of radio occultation signals, *Radio Sci.*, *38*(3), 1040, doi:10.1029/2002RS002763.

Karl, T. R., S. J. Hassol, C. D. Miller, and W. L. Murry (Eds.) (2006), *Temperature Trends in the Lower Atmosphere: Steps for Understanding and Reconciling Differences*, Clim. Change Sci. Program, Washington, D. C.

Kirchengast, G., J. Hafner, and W. Poetzi (1999), The CIRA-86aQ_UoG model: An extension of the CIRA-86 monthly tables including humidity tables and a Fortran 95 global moist air climatology model, *IMG/UoG Tech. Rep., 8*, Eur. Space Agency, Paris.

Kirchengast, G., S. Schweitzer, J. Ramsauer, and J. Fritzer (2007), End-to-end Generic Occultation Performance Simulator version 5.2 (EGOPSv5.2) software user manual (overview, reference, and file format manual), *Tech. Rep., ESA/ESTEC-4/2007*, Wegener Cent., Univ. of Graz, Graz, Austria.

König, R., G. Michalak, K. Neumayer, and S. Zhu (2006), Remarks on CHAMP orbit products, in *Observation of the Earth System From Space*, edited by J. Flury et al., pp. 17–26, Springer, Berlin, doi:10.1007/3-540-29522-4_2.

Kuo, Y. H., T. K. Wee, S. Sokolovskiy, C. Rocken, W. Schreiner, and D. Hunt (2004), Inversion and error estimation of GPS radio occultation data, *J. Meteorol. Soc. Jpn.*, *82*, 507–531, doi:10.2151/jmsj.2004.507.

Kursinski, E. R., G. A. Hajj, J. T. Schofield, R. P. Linfield, and K. R. Hardy (1997), Observing Earth's atmosphere with radio occultation measurements using the Global Positioning System, *J. Geophys. Res.*, *102*, 23,429–23,465, doi:10.1029/97JD01569.

Lackner, B. C., A. K. Steiner, G. C. Hegerl, and G. Kirchengast (2011), Atmospheric climate change detection by radio occultation data using a fingerprinting method, *J. Clim.*, *24*, 5275–5291, doi:10.1175/2011JCLI3966.1.

Lambeck, K. (1988), *Geophysical Geodesy: The Slow Deformations of the Earth*, Oxford Univ. Press, Oxford, U. K.

Lauritsen, K. B., S. Syndergaard, H. Gleisner, M. E. Gorbunov, F. Rubek, M. B. Sørensen, and H. Wilhelmsen (2011), Processing and validation of refractivity from GRAS radio occultation data, *Atmos. Meas. Tech.*, *4*, 2065–2071, doi:10.5194/amt-4-2065-2011.

Leroy, S. S. (1997), Measurement of geopotential heights by GPS radio occultation, *J. Geophys. Res.*, *102*(D6), 6971–6986, doi:10.1029/96JD03083.

Leroy, S. S., J. G. Anderson, and J. A. Dykema (2006), Testing climate models using GPS radio occultation: A sensitivity analysis, *J. Geophys. Res.*, *111*, D17105, doi:10.1029/2005JD006145.

Lohmann, M. (2005), Application of dynamical error estimation for statistical optimization of radio occultation bending angles, *Radio Sci.*, *40*, RS3011, doi:10.1029/2004RS003117.

Mears, C. A., M. C. Schabel, and F. J. Wentz (2003), A reanalysis of the MSU channel 2 tropospheric temperature record, *J. Clim.*, *16*, 3650–3664, doi:10.1175/1520-0442(2003)016<3650:AROTMC>2.0.CO;2.

Mears, C. A., F. J. Wentz, P. Thorne, and D. Bernie (2011), Assessing uncertainty in estimates of atmospheric temperature changes from MSU and AMSU using a Monte-Carlo estimation technique, *J. Geophys. Res.*, *116*, D08112, doi:10.1029/2010JD014954.

Ohring, G. (Ed.) (2007), *Achieving Satellite Instrument Calibration for Climate Change*, 144 pp., NOAA, Camp Springs, Md.

Phinney, R. A., and D. L. Anderson (1968), On the radio occultation method for studying planetary atmospheres, *J. Geophys. Res.*, *73*, 1819–1827, doi:10.1029/JA073i005p01819.

Pirscher, B. (2010), Multi-satellite climatologies of fundamental atmospheric variables from radio occultation and their validation, *Sci. Rep., 33-2010*, Wegener Cent., Graz, Austria.

Pirscher, B., U. Foelsche, B. C. Lackner, and G. Kirchengast (2007), Local time influence in single-satellite radio occultation climatologies from sun-synchronous and non sun-synchronous satellites, *J. Geophys. Res.*, *112*, D11119, doi:10.1029/2006JD007934.

Prabhakara, C., R. Iacovazzi, J. M. Yoo, and G. Dalu (2000), Global warming: Evidence from satellite observations, *Geophys. Res. Lett.*, *27*(21), 3517–3520, doi:10.1029/2000GL011719.

Press, W. H., S. A. Teukolsky, W. T. Vetterling, and B. P. Flannery (1996), *Numerical Recipes in Fortran 77: The Art of Scientific Computing*, Cambridge Univ. Press, Cambridge, U. K.

Rieder, M. J., and G. Kirchengast (2001), Error analysis and characterization of atmospheric profiles retrieved from GNSS occultation data, *J. Geophys. Res.*, *106*, 31,755–31,770.

Ringer, M. A., and S. B. Healy (2008), Monitoring twenty-first century climate using GPS radio occultation bending angles, *Geophys. Res. Lett.*, *35*, L05708, doi:10.1029/2007GL032462.

Rocken, C., et al. (1997), Analysis and validation of GPS/MET data in the neutral atmosphere, *J. Geophys. Res.*, *102*(D25), 29,849–29,866, doi:10.1029/97JD02400.

Saha, S., et al. (2010), The NCEP climate forecast system reanalysis, *Bull. Am. Meteorol. Soc.*, *91*, 1015–1057, doi:10.1175/2010BAMS3001.1.

Savitzky, A., and M. J. E. Golay (1964), Smoothing and differentiation of data by simplified least squares procedures, *Anal. Chem.*, *36*(8), 1627–1639, doi:10.1021/ac60214a047.

Scherllin-Pirscher, B., G. Kirchengast, A. K. Steiner, Y.-H. Kuo, and U. Foelsche (2011a), Quantifying uncertainty in climatological fields from GPS radio occultation: An empirical-analytical error model, *Atmos. Meas. Tech.*, *4*, 2019–2034, doi:10.5194/amt-4-2019-2011.

Scherllin-Pirscher, B., A. K. Steiner, G. Kirchengast, Y.-H. Kuo, and U. Foelsche (2011b), Empirical analysis and modeling of errors of atmospheric profiles from GPS radio occultation, *Atmos. Meas. Tech.*, *4*, 1875–1890, doi:10.5194/amt-4-1875-2011.

Schreiner, W., C. Rocken, S. Sokolovskiy, and D. Hunt (2009), Quality assessment of COSMIC/FORMOSAT-3 GPS radio occultation data derived from single- and double-difference atmospheric excess phase processing, *GPS Solut.*, *14*(1), 13–22, doi:10.1007/s10291-009-0132-5.

Schreiner, W., S. Sokolovskiy, D. Hunt, C. Rocken, and Y.-H. Kuo (2011), Analysis of GPS radio occultation data from the FORMOSAT-3/COSMIC and Metop/GRAS missions at CDAAC, *Atmos. Meas. Tech.*, *4*(10), 2255–2272, doi:10.5194/amt-4-2255-2011.

Smith, E., and S. Weintraub (1953), The constants in the equation for atmospheric refractive index at radio frequencies, *Proc. IRE*, *41*, 1035–1037, doi:10.1109/JRPROC.1953.274297.

Sokolovskiy, S., and D. Hunt (1996), Statistical optimization approach for GPS/MET data inversion, paper presented at GPS/MET Workshop, Int. Union of Radio Sci., Tucson, Ariz.

Sokolovskiy, S., Y.-H. Kuo, and W. Wang (2005), Assessing the accuracy of a linearized observation operator for assimilation of radio occultation data: Case simulations with a high-resolution weather model, *Mon. Weather Rev.*, *133*, 2200–2212, doi:10.1175/MWR2948.1.

Sokolovskiy, S., W. Schreiner, C. Rocken, and D. Hunt (2009), Optimal noise filtering for the ionospheric correction of GPS radio occultation signals, *J. Atmos. Oceanic Technol.*, *26*(7), 1398–1403, doi:10.1175/2009JTECHA1192.1.

Steiner, A. K., and G. Kirchengast (2005), Error analysis for GNSS radio occultation data based on ensembles of profiles from end-to-end simulations, *J. Geophys. Res.*, *110*, D15307, doi:10.1029/2004JD005251.

Steiner, A. K., G. Kirchengast, and H.-P. Ladreiter (1999), Inversion, error analysis, and validation of GPS/MET occultation data, *Ann. Geophys.*, *17*, 122–138.

Steiner, A. K., G. Kirchengast, B. C. Lackner, B. Pirscher, M. Borsche, and U. Foelsche (2009), Atmospheric temperature change detection with GPS radio occultation 1995 to 2008, *Geophys. Res. Lett.*, *36*, L18702, doi:10.1029/2009GL039777.

Steiner, A. K., B. C. Lackner, F. Ladstädter, B. Scherllin-Pirscher, U. Foelsche, and G. Kirchengast (2011), GPS radio occultation for climate monitoring and change detection, *Radio Sci.*, *46*, RS0D24, doi:10.1029/2010RS004614.

Švehla, D., and M. Rothacher (2003), Kinematic and reduced-dynamic precise orbit determination of low earth orbiters, *Adv. Geosci.*, *1*, 47–56, doi:10.5194/adgeo-1-47-2003.

Syndergaard, S. (1998), Modeling the impact of the Earth's oblateness on the retrieval of temperature and pressure profiles from limb sounding, *J. Atmos. Sol. Terr. Phys.*, *60*, 171–180, doi:10.1016/S1364-6826(97)00056-4.

Syndergaard, S. (1999), Retrieval analysis and methodologies in atmospheric limb sounding using the GNSS radio occultation technique, *Sci. Rep., 99-6*, Dan. Meteorol. Inst., Copenhagen.

Thorne, P. W., D. E. Parker, J. R. Christy, and C. A. Mears (2005), Uncertainties in climate trends: Lessons from upper-air temperature records, *Bull. Am. Meteorol. Soc.*, *86*, 1437–1442, doi:10.1175/BAMS-86-10-1437.

Thorne, P. W., J. R. Lanzante, T. C. Peterson, D. J. Seidel, and K. P. Shine (2011), Tropospheric temperature trends: History of an ongoing controversy, *WIREs Clim. Change*, *2*, 66–88, doi:10.1002/wcc.80.

Turcotte, D. L., and G. Schubert (1982), *Geodynamics: Application of Continuum Physics to Geological Problems*, John Wiley, New York.

Ustinov, E. A. (1990), To the solution of the problem of the numerical differentiation by the statistical optimization method, *Cosmic Res., Engl. Transl.*, *28*(4), 545–554.

Vorob'ev, V. V., and T. G. Krasil'nikova (1994), Estimation of the accuracy of the atmospheric refractive index recovery from Doppler shift measurements at frequencies used in the NAVSTAR system, *Phys. Atmos. Ocean*, *29*, 602–609.

Wickert, J., G. Beyerle, G. A. Hajj, V. Schwieger, and C. Reigber (2002), GPS radio occultation with CHAMP: Atmospheric profiling utilizing the space-based single difference technique, *Geophys. Res. Lett.*, *29*(8), 1187, doi:10.1029/2001GL013982.

Wickert, J., et al. (2009), GPS radio occultation: Results from CHAMP, GRACE and FORMOSAT-3/COSMIC, *Terr. Atmos. Oceanic Sci.*, *20*, 35–50, doi:10.3319/TAO.2007.12.26.01(F3C).

Zou, C. Z., and W. Wang (2011), Intersatellite calibration of AMSU-A observations for weather and climate applications, *J. Geophys. Res.*, *116*, D23113, doi:10.1029/2011JD016205.

Zou, C. Z., M. D. Goldberg, Z. Cheng, N. C. Grody, J. T. Sullivan, C. Cao, and D. Tarpley (2006), Recalibration of microwave sounding unit for climate studies using simultaneous nadir overpasses, *J. Geophys. Res.*, *111*, D19114, doi:10.1029/2005JD006798.